Faculty of Physics and Astronomy
University of Heidelberg

Diploma thesis
in Physics

submitted by
Gerhard Zürn
born in Heilbronn
2009

Realization of an Optical Microtrap for a Highly Degenerate Fermi Gas

This diploma thesis has been carried out by
Gerhard Zürn at the
Max-Planck-Institute for Nuclear Physics
under the supervision of
Juniorprofessor Dr. Selim Jochim

Abstract:
This thesis reports on the realization of a micrometer-sized optical dipole trap for the preparation of a highly degenerate Fermi gas of ^{6}Li atoms. The degenerate ensemble in the microtrap is the starting point for future experiments with a finite number of fermions. One phenomenon to study will be the formation of a shell structure in an interacting two-component spin-mixture. ^{6}Li is especially well suited for such experiments due to the easy tuneability of the inter-particle interaction by means of Feshbach resonances.
In the course of this thesis, we present our apparatus for the creation of ultracold Fermi gases. Thereby, the main subject is the assembly of our microtrap. After analyzing the assembly in an external test setup, we focus on the scheme for the transfer of atoms from our large volume optical dipole trap into the microtrap. Using a non-interacting Fermi gas we were able to determine the characteristics of the microtrap, such as lifetime and trap frequencies. Subsequently, we can give an estimation for the degeneracy of the Fermi gas inside. As an outlook, we present our first promising attempts to control the particle number, which is the next milestone on the way towards experiments on finite systems of fermions.

Zusammenfassung:
In dieser Arbeit wird die Realisierung einer mikrometer-großen optischen Dipolfalle für die Herstellung eines hoch entarteten Fermi Gases aus ^{6}Li Atomen behandelt. Das entartete Ensemble in der Mikrofalle ist der Ausgangspunkt für zukünftige Experimente mit einer endlichen Anzahl von Fermionen. Ein zu untersuchendes Phänemen wird die Ausbildung einer Schalenstruktur in einer zwei komponentigen wechselwirkenden Spin Mischung sein. ^{6}Li ist besonders dafür geeignet, weil man die Wechselwirkung zwichen den Teilchen mit Hilfe von Feschbach Resonanzen leicht einstellen kann.
Im Verlauf der Arbeit werden wir unseren Experimentaufbau zur Erzeugung von ultrakalten Fermi Gasen vorstellen. Dabei wird der Schwerpunkt auf den Aufbau unserer Mikrofalle gelegt sein. Nach dem Test in einem externen Aufbau werden wir besonders auf den Transfer von Atomen aus unserer optischen Falle, die ein großes Volumen besitzt, in die Mikrofalle eingehen. Mit Hilfe eines nicht wechselwirkendem Fermi Gases haben wir die Möglichkeit die Eigenschaften der Mikrofalle, wie Lebensdauer und Fallenfrequenzen, zu bestimmen. Anschließend können wir eine Abschätzung für die Entartung des Fermi Gases in der Falle geben. Als Ausblick stellen wir unsere ersten vielversprechenden Versuche die Teilchenzahl zu kontrollieren vor. Die Kontrolle über die Teilchenzahl ist der nächste wichtig Schritt auf dem Weg zu Experimenten mit endlichen Systemen aus Fermionen.

Contents

Chapter 1

Introduction

In 1924 Pauli introduced the spin as an additional quantum number [Pau25] with no classical analogon, to correctly describe the splitting of lines in the atomic excitation spectrum. The completely new concept divides particles into two categories. The quantum state of particles possessing an integer spin quantum number, which are called bosons, is totally symmetric. The states of the complementary group of particles having half odd-integer spin, called fermions, is totally antisymmetric, which results in fundamentally different physical properties. By understanding the nature of fermions, the first known few fermionic system namely electrons in an atom could be explicitly described by quantum mechanics. Later on with the development of the nucleon shell model, to which Goeppert-Mayer [May49] and Jensen [Sue49] significantly contributed, the next more complicated few fermion system had been investigated. In the mean time Fermi and Dirac had developed their statistical description for fermions [Dir26, Zan99] which could be soon applied to a large array of many-body systems like electrons in metals or neutrons in neutron stars.
The observation of the quantum statistical nature of bosons and fermions in atomic gases became probable with the development of laser cooling, proposed in 1975 [Hae75], which was possible due to increased knowledge about the internal structure of atoms and progress in laser physics. A substantial property of these atomic gases, prepared at low temperature, is the short range of the interaction potential compared to the inter-particle spacing. This implies that in this so called dilute gases, the interaction can be described by a point-like collisional interaction of the particles. In the low energy limit the scattering process is determined by only one parameter, the s-wave scattering length, which drastically simplifies the description of interaction. If the scattering length is large compared to the characteristic length scale of the interaction potential, the system is universal. In the limit of long distances, the atomic gas exhibits identical properties as other universal systems with possibly completely different type of interaction, independent whether the

short range behavior differs from each other. Due to symmetry reasons, contributions of even partial waves in the scattering process vanish for identical fermions which is the reason why they do not interact at low temperatures. However, if interaction is desired, this can be overcome by using a spin mixture of different hyperfine Zeeman sublevels.
To enter a regime where the quantum statistical nature of either bosons or fermions becomes observable, several orders of magnitude in phase space have to be gained, which implies very low temperatures of the dilute gases, which became possible with the development of further cooling techniques. The initial attention was directed to the statistics of bosons which led to the first direct observation of a Bose- Einstein condensate. Since the first realization of Bose- Einstein condensation in dilute gases in 1995 [And95, Dav95], experiments on these ultracold quantum gases have evolved to an important playground for studying interesting new physics and to test theories which can be applied to systems in "real nature". Studying an ideal Fermi gas with no interaction [DeM99] was the first step to various following experiments with ultracold fermions.
A big breakthrough was the discovery of Feshbach resonances in quantum gases [Ino98]. A Feshbach resonance - the term originates from Herman Feshbachs work on resonance phenomena in nuclear physics - occurs when a bound state of a different interaction potential is close to the continuum of the scattering state. The scattering length diverges when the bound state coincides with the continuum threshold of the scattering state. Magnetically tuning these states to one another allows the scattering length to adopt arbitrary values. Feshbach resonances opened the door to study the wide range of weakly to strongly interacting Fermi gases. In 2003, three different groups [Reg03, Joc03a, Zwi03] independently created the first molecular BEC, where these dimers consisting of two fermions had been formed near a Feshbach resonance. Soon after, the crossover [Bar04, Bou04] to the side of the resonance with attractive interaction where the molecules are continuously transformed into many-body pairs, has been investigated. The appearance of a superfluid phase was examined by [Zwi05], working with large ensembles of cold fermions. Introducing optical lattices to cold atoms allows for studying phenomena which occur in solid state physics such as the fermionic Mott-insulator phase [Joe08]. The large diversity of tunable parameters in such systems could presumably open the possibility to investigate the phenomena of high-temperature superconductivity, which appearance in solid states is not yet completely understood. By studying the universal properties of ultracold gases we could even gain insight into phenomena in high energy physics and learn about quark matter. Therefore, a first step could be for instance the investigation of thermal three component Fermi gases [Ott08, Huc09].
The previous outstanding success of ultracold quantum gases for modeling many-body systems and the investigation of few-body phenomena, recommends to ex-

pand the field on systems of finite size, taking advantage of the exceptional nature of ultracold gases namely the tunability of the interaction strength. Together with the possibility to create various forms of trapping potentials, one should gain the possibility to create a generic system for few-fermion systems in "real nature" like the nucleons in nuclei, the electrons in atoms or atoms in cluster. Observation of a change in the shell structure and the appearance of orbitals in such a system could be the first phenomena to be investigated by the variation over a wide range from no interaction to strong interaction. Starting from a highly degenerate Fermi gas, statistically described in the limit of large particle numbers, it is interesting to study experimentally when the thermodynamical description by a Fermi sea breaks down and effects of finite size becomes visible.
On the way towards these systems it will be essential to fill all quantum states of the potential by one fermion. Commonly experiments start from thermal gases which are evaporatively cooled to the degenerate regime. However, there still exist holes - unoccupied states whose energy are lower than the energy of another occupied state - in the Fermi Sea. If the thermal energy is larger than the level spacing of the states it is possible that atoms are scattered to higher levels which can be seen as an excitation inside the potential. Hence, to obtain high level spacing we need a micrometer sized trap! Furthermore, this trap in combination with a shallow trap allows for the creation of a highly degenerate Fermi gas. The realization of such a microtrap for ^{6}Li atoms will be described in the course of this thesis. We also aim for control of the quantum states of the microtrap. Descriptively by a deep cut into the Fermi sea we want to achieve control of the particle number as well as ensure that the probability of state occupation diverges to one.

Outline

In the beginning we summarize the interaction properties of ^{6}Li atoms at ultracold temperatures including a conceptional description of Feshbach resonances. After discussing the properties of Fermi gases, a short summary of the principle of Laser cooling and of the optical dipole traps we use, will be given. In the third chapter we will focus on the idea for the realization of a highly degenerate Fermi gas. Furthermore, our method to control the quantum states of the potential which is required for the preparation of a finite system of fermions, is described. In the next chapter we present our apparatus for creating a degenerate ensemble of ^{6}Li atoms, with emphasis on the detection scheme. We give a detailed description of the assembly of our coils, which create the large magnetic fields for tuning the interaction strength. The fifth chapter will concentrate on the realization of the micrometer-sized optical dipole trap. First the requirements on the high-resolution assembly are discussed and the actual design is presented. In an external test setup

the optical properties of the trap are determined. From this the expected parameters of the microtrap for trapped ^{6}Li atoms are calculated. The limits of the current microtrap design are discussed and compared with simulations of different designs, which we could be able to implement in future. In the sixth chapter we report on the creation of a highly degenerate Fermi gas in our microtrap. Initially we describe our method of spatially superimposing the microtrap with the shallow optical crossed-beam dipole trap. After discussing the optimised transfer of atoms to the microtrap, we determine the lifetime of the trapped fermions. We also measure the trap frequencies from which we can calculate characteristic parameters of the trapped ensemble such as the Fermi temperature. This allows us to give an estimation of the achieved degeneracy of the prepared Fermi gas in the microtrap. In the outlook we discuss our next step towards a finite system of fermions. We finish by presenting our first promising attempt to control the particle number in the microtrap.

Chapter 2

Ultracold Fermi Gases

Our long-term goal is the preparation of a finite system of degenerate fermions. On the way towards this, the emphasis of this thesis lies on the realization of a highly degenerate Fermi gas in a tiny and deep potential. Therefore, in this chapter, we give an overview over the thermodynamical properties of a Fermi gas in the noninteracting as well as in interacting case. First we give a short introduction to the collisional interaction at ultracold temperatures. At the end of this chapter the cooling and trapping techniques used in the experiment are briefly summarized.

2.1 Two-body interaction of ultracold fermions

A fundamental property of particles with half-odd-integer spin is the antisymmetry of their total wave function which has defining consequences on their interaction properties. Whether fermionic elementary particles or compound fermions in the dilute low energy regime, they exhibit similar physical properties. For preparing a Fermi gas at ultracold temperatures interaction is required. Elastic collisions are favoured by the experimentalists since inelastic collisions lead to a change of the internal state and the released energy causes the particles to escape of the trapping potential. For ultracold temperatures we can describe the elastic interaction by only one parameter, the scattering length a. A nice feature of ^{6}Li is the availability of a broad Feshbach resonance which allows for tuning of the scattering length to arbitrary values. Thereby, we can enter the whole region of possible interactions from attractive to repulsive interaction. If the scattering length is larger than the range of the interaction potential the system exhibits universal properties valid for all fermions only defined by the scattering length and independent of the type of interaction potential. Thus, ultracold gases are particularly predestined for studying phenomena arising in fermionic systems. In the following section we

will focus on the collisional two-body interaction.

2.1.1 Elastic scattering at the zero energy limit

We are looking for the solution of two particles with an interaction potential $V(r)$ with equivalent mass m. As we are interested in the collisional process we only concentrate on the relative motion of the particles since the solution of the Schrödringer equation for the center of mass motion is the one of a free particle. The Schrödringer equation then reads

$$\left(-\frac{\hbar\vec{\nabla}^2}{2m_r} + V(\vec{r})\right)\Psi_k(\vec{r}) = E_k\Psi_k(\vec{r}) \tag{2.1}$$

with the reduced mass $m_r = 2m$ and the collisional energy $E_k = \hbar k^2/(2m_r)$. We look for a solution for $r = |\vec{r}|$ far away from the range of the potential being a superposition of an incident plane wave and a scattered spherical wave with scattering amplitude $f_k(\theta)$:

$$\Psi_k \propto e^{ikz} + f_k(\theta)\frac{e^{ikr}}{r} \tag{2.2}$$

whereas θ ($0 \leq \theta < \pi$) is the angle between the incident plane wave pointing into z-direction and the direction of observation. Using flux equations we can determine the differential cross section from the scattering amplitude:

$$\frac{d\sigma(k)}{d\theta} = |f_k(\theta)|^2. \tag{2.3}$$

The symmetry of the potential allows for solving the Schrödinger equation by an ansatz using the spherical harmonics as eigenfunctions of the angular momentum operator $\vec{L}^2$ and L_z and by a radial function which solution is given by a superposition of spherical Bessel functions. Additionally the plane wave in the wavefunction of equation 2.2 can be expanded by incoming and outgoing spherical waves. By comparison the latter expansion with the solution given by the Bessel functions, one obtains for the scattering amplitude:

$$f_k(\theta) = \frac{1}{2ik}\sum_{l=0}^{\infty}(2l+1)P_l(\cos\theta)(e^{2i\delta_l(k)} - 1) \tag{2.4}$$

with $P_l(\cos\theta)$ the Legendre polynomials. $\delta_l(k)$ is the phase shift of the l-th partial wave which incorporates the effect of the potential on the collision process. Then

the total cross section is the sum of all contributions arising from each partial wave

$$\frac{d\sigma(k)}{d\theta} = \sum_{l=0}^{\infty} \sigma_l(k) \tag{2.5}$$

with the partial cross section

$$\sigma_l(k) = \frac{4\pi}{k^2}(2l+1)\sin^2\delta_l(k). \tag{2.6}$$

For identical particles we cannot distinguish of the processes where the relative particle is either scattered to angle θ or to $\pi - \theta$ which is why particle exchange yield the same result. Since we are working with fermions the total wave function has to be antisymmetric. Because of parity -1 only partial waves with odd number contribute to the total cross section.
For low energy, however, partial waves higher than $l = 0$ are suppressed. The incident energy is not large enough to overcome the centrifugal barrier in the radial Schrödinger equation. This is why in ^{6}Li at energy lower than $E = k_B \times 7mk$ [Jul92] only s-wave scattering can occur. Because the cross section for identical fermions then vanishes, interaction is switched off for low temperatures. For non identical particles s-wave scattering, which is completely isotropic, remains. In the limit of momentum $k = \sqrt{2m_r E}/\hbar$ approaching 0 the cross section for non identical fermions can be written by

$$\sigma_0(k) = 4\pi a^2 \tag{2.7}$$

with a the s-wave scattering length defined by

$$a = -\lim_{k\to 0} \frac{\tan\delta_0(k)}{k} \tag{2.8}$$

At low energy the interaction strength can now be expressed by only one parameter, the s-wave scattering length a. However, a can diverge for the phase shift δ_0 approaching $\pi/2$ and so consequently the cross section diverges, which cannot be a physical solution, since the outgoing flux cannot exceed the incoming. The limit of outgoing flux equals the incoming is called the unitarity limit. In this regime the relation of equation 2.7 valid for $ka \ll 1$ is not correct. A more detailed investigation [Sch07, Sak94] shows that the cross section for $ka \gg 1$ is then only dependent on the particle momentum:

$$\sigma_0(k) = \frac{4\pi}{k^2} \tag{2.9}$$

Spin mixture

As mentioned, in the low energy limit spin polarized atoms cannot interact. As we study interacting Fermi gases, we need a mixture of non identical fermions. At a first glance one would think of a mixture of different species which has the advantage of setting the relative mass as an additional parameter by selecting the species. However, an additional specie more or less doubles the effort for building and maintaining the experiment. Instead we take a spin mixture of different Zeeman sublevels of the lowest hyperfine state of ^{6}Li . For zero angular momentum the electron spin $\vec{s}$ of the valence electron and the nuclear spin $\vec{I}$ couple to two hyperfine states, whereas the lowest states splits up in a Zeeman doublet for low magnetic fields. In the Paschen Back regime for fields larger than $50G$, the electron spin decouples from the nuclear spin and is aligned in the external field. In this regime the nuclear spin is aligned separately, with 3 different possible projections to the quantization axis. In our experiment we use a mixture of the states $|m_s = -1/2, m_I = 1 >$ connected to the $|F = 1/2, m_F = 1/2 >$ state at low field and $|m_s = -1/2, m_I = 0 >$ connected to $|F = 1/2, m_F = -1/2 >$. These states have the advantage that they cannot undergo inelastic spin exchange collisions due to the non existence of energetically reachable final states. These two lowest states we label by $|1\rangle$ and $|2\rangle$ taking a standard nomenclature often used in this system . The level scheme of ^{6}Li is illustrated in the appendix. Details on the preparation of such a mixture are described in the experimental part in chapter 4. Here, we concentrate on the tuneability of the interaction strength.

Resonance scattering

We are interested in how the scattering length depends on the presence of a bound state in the interaction potential close to the continuum. In the following we assume a box like potential with depth U and extend b; however, the result can be generalized to the inter-atomic potential. If we assume a potential well, one finds that the scattering length is always positive for the repulsive interaction [Dal98]. For a box potential with a depth/extend ratio too low for supplying any bound state near the continuum, the scattering length is small and negative while the interaction is attractive. By increasing the depth the scattering length diverges to $-\infty$ when the potential is large enough to hold a bound state. If the state becomes bound the scattering length goes from $+\infty$ to smaller positive values with increasing distance from the continuum during the further increase of the depth. The scattering length has to cross zero when a second bound state is getting to be supplied by the potential. Wouldn't it be nice to make use of such a resonance where a bound state is provided? If one finds a possibility to change the energy of the bound state the scattering length could be tuned to arbitrary values.

2.1.2 Feshbach resonances in ^{6}Li

The difference of a Feshbach resonance to the resonance described above is, that the scattering potential does not have to provide a bound state near the collision energy. Instead a bound state of a different collision channel is resonantly coupled to the scattering channel.

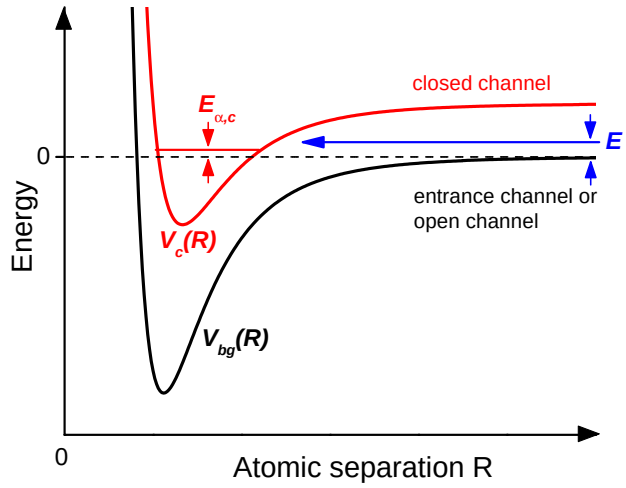

Figure 2.1: Illustration of the Feshbach resonance. The atoms enter the collision in the open channel with kinetic energy E. If there is a close channel bound state near the entrance energy, the open channel couples to the closed channel. The outgoing scattering wave experiences a phase shift which leads to a divergence of the scattering length at resonance. If one finds a way to control the energy difference $E - E_{\alpha,c}$, one can tune the coupling of the states and so the scattering length. The picture is taken from [Chi06] and slightly adapted.

In very high magnetic field state $|1\rangle$ and $|2\rangle$ are totally spin polarized. The two-particle state has to be a triplet state because of the conservation of the spin projection quantum number. Its potential in general provides less bound states than the singlet because the antisymmetric wave function reduces the possibility of the electrons being close together which could decrease their total energy. In ^{6}Li the triplet potential provides a quasi-bound state close above the continuum, from which the large value of the background scattering length arises.
For a pictorial explanation of the Feshbach resonance we define the channel energy E_α as the internal energy of the two separated atoms following the more detailed description of [Chi06]. A channel is called an open channel if the total energy $E_{tot} = E_{\alpha,o} + E$, with E the kinetic energy, is equal or larger then the total energy of the initial collision state; it is called a closed channel if the energy is lower and the atoms are not able to separate to free atoms. A Feshbach resonance

occurs when the energy of a bound state crosses the collision energy of the open channel. The situation is illustrated in figure 2.1. By coupling of the entrance channel to the closed channel the atoms can be virtually in the bound state before they separate. By that, they pick up a phase shift which leads to a resonant scattering length

$$a_{res} \propto \frac{1}{E_{tot} - E_{\alpha,c}} \tag{2.10}$$

which is inverse proportional to the energy difference of these states. Again the scattering length can adopt values from $-\infty$ to $+\infty$ dependent on the sign of the energy difference. In a magnetic Feshbach resonance this difference can be tuned by the magnetic field. If there is a difference in magnetic moment of the closed channel an the open channel,

$$\delta\mu = \mu_{atoms} - \mu_c \tag{2.11}$$

the energy difference tunes in the magnetic field. The resulting effective scattering length, dependent on the background scattering length a_{bg} and the width of the resonance Δ_B which is related to the coupling strength, is then given by

$$a(B) = a_{bg}\left(1 - \frac{\Delta_B}{B - B_0}\right). \tag{2.12}$$

B_0 denotes the position of the resonance. In the region from 0 to $1500G$ the $|1\rangle$-$|2\rangle$ spin-mixture provides two Feshbach resonances. This is due to the existence of two different hyperfine states with nuclear spin quantum number $I = 0$ and $I = 2$ for the highest vibrational singlet state to which the triplet state couples. The hyperfine coupling to the $I = 0$ is weak which expresses in a narrow resonance at $543G$. A broad resonance at $834G$ appears for the $I = 2$ state which can be extensively used in the experiments. By tuning the magnetic field any scattering length shown in figure 2.2 is accessible.

2.2 Thermodynamic description of a Fermi gas

In this section we want to give an overview of the properties of a Fermi gas. We want to point out the quantum statistical effects of the fermions at low temperatures leading to a degenerate Fermi gas. We focus on the discussion of the non-interacting case and derive the density profiles for a Fermi Gas in a harmonic potential. Additionally we describe the method of how we want to create a highly degenerate Fermi Gas. We give an outlook of how we can achieve a system with only few fermions where the thermodynamical description breaks down.

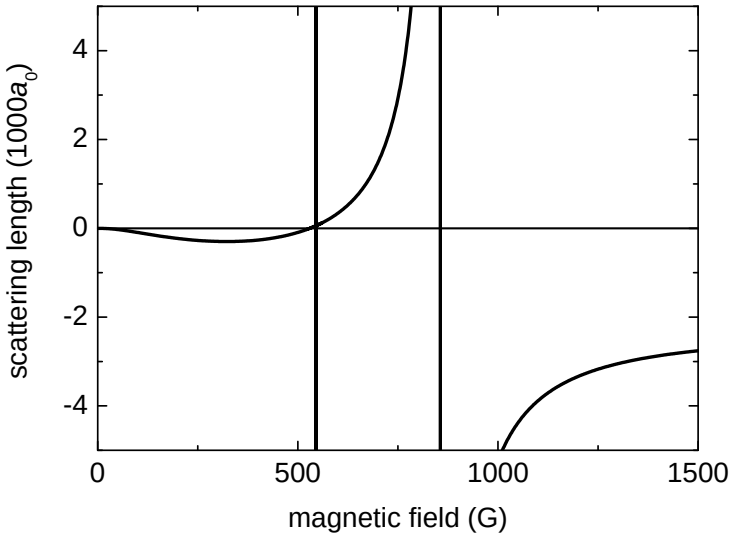

Figure 2.2: $|1\rangle$- $|2\rangle$ s-wave scattering length of ^{6}Li dependent on the applied homogeneous magnetic field. For low magnetic fields the singlet and triplet collision states mixes and the scattering length is almost completely zero. At $543G$ a narrow Feshbach resonance occurs. At $834G$ the system exhibits a nice broad Feshbach resonance which allows the experimentalist to tune the interaction from repulsive to attractive with a zero crossing of the scattering length at $530G$. Below the resonance, if a third particle is involved into the scattering process, it can carry away momentum and satisfy angular momentum conservation to keep the atoms in the bound molecular singlet state which can be used to create a molecular BEC [Gre03, Joc03b, Zwi03]. As a many-body phenomena on the upper side of the resonance at strong attractive interaction many-body atom-pairs [Chi04] can be formed. For large magnetic field the scattering length converges to the triplet background scattering length. The plot is taken from [Joc04].

2.2.1 Ideal Fermi gas in a harmonic potential

First of all, we only consider non-interacting fermions in a harmonic potential, which we find for identical fermions at low temperatures due to the absence of s-wave scattering as described in section 2.1. Most experiments work with magnetic or optical traps, which can be approximated as harmonic around its minimum. The Hamiltonian of a radially symmetric trap with an aspect ratio of the trapping frequencies $\omega_r/\omega_a = 1/\lambda$ then reads

$$H(\vec{r},\vec{p}) = \frac{\vec{p}^{\,2}}{2m} + \frac{m\omega_r^2}{2}\left(x^2+y^2+\lambda z^2\right). \tag{2.13}$$

If the thermal energy significantly exceeds the level spacing of the harmonic trap ($k_B T \gg \hbar\omega_r$) we can consider the states as a continuum of states which density

is given by

$$g(E) = \frac{E^2}{2\lambda(\hbar\omega_r)^3} \tag{2.14}$$

whereas E denotes the total energy of one fermion. The occupation probability of the states at a certain temperature T is given by the Fermi-Dirac distribution from which we can approximatively deduce the number density in phase space

$$n(\vec{p},\vec{r}) = \frac{1}{(2\pi\hbar)^3}\frac{1}{e^{\beta(H-\mu)}+1} \tag{2.15}$$

with $1/(2\pi\hbar)^3$ the phase space density and $\beta^{-1} = k_B T$ the thermal energy. For this semi-classical approximation, valid for large numbers of fermions, we have assumed that each fermion is represented by a wave packet with central momentum $\vec{p}$ and position $\vec{r}$ in phase space. However, integrating (2.15) over the whole phase space, which is substituted by the energy distribution of the harmonic oscillator by means of (2.14), has to give the correct number of fermions

$$N = \int n(\vec{p},\vec{r})d\vec{p}d\vec{r} = \frac{1}{2\lambda(\hbar\omega_r)^3}\int_0^\infty \frac{E^2 dE}{e^{\beta(E-\mu)}+1} \tag{2.16}$$

which constrains the chemical potential μ. Unfortunately, this equation cannot be solved for the chemical potential $\mu(T,N)$ analytically. So we first determine μ for $T = 0$ before we later give some approximative solution for finite temperature. For the description we follow [Joc09] and [But97].

Zero temperature

Assuming zero temperature the integration of equation can be performed because the Fermi-Dirac distribution ends up in a step function. For the chemical potential we obtain

$$\mu(T=0,N) := E_F := k_B T_F = \hbar\omega_r(6N\lambda)^{1/3} \tag{2.17}$$

which can be descriptively understood as the energy that is needed to add an additional particle at zero temperature to the edge of the Fermi sea. Thereby we also defined the Fermi energy E_F and the Fermi temperature T_F which are characteristic parameters of the Fermi gas only dependent on the particle number and the trapping frequencies. In experiments one of the most important observable is the spatial distribution of the particles in situ or after a certain time of flight. From the time of flight (TOF) measurement we can determine the initial momentum distribution while for large TOFs we can neglect the initial expansion [And95]. Due to the Pauli exclusion principle we expect an expansion of the fermionic cloud larger than the spatial distribution of the ground state. As well the momentum distribution associated with the Pauli pressure should be comparatively large. The

characteristic value for the size of the cloud is given by the excursion of a classical particle with energy E_f in the harmonic trapping potential:

$$r_F = \sqrt{\frac{2E_F}{m{\omega_r}^2}} \tag{2.18}$$

To get the actual spatial distribution at $T = 0$ we have to integrate equation 2.14 over momentum space. Therefore we define for each spatial position a "local" Fermi momentum

$$\frac{p_{F,l}^2}{2m} + V(r) = E_F. \tag{2.19}$$

The spatial number density at this point is then given by the volume $p_{F,l}^3$ of the local Fermi sea in momentum space multiplied by the phase space density:

$$n(\rho, T = 0) = \frac{N}{r_F^3}\frac{8}{\pi^2}\left(1 - \frac{\rho^2}{r_F^2}\right)^{3/2} \tag{2.20}$$

whereas we have defined $\rho = (x^2 + y^2 + \lambda z^2)^{1/2}$ as the effective distance. We note that this approximation only gives meaningful values for distances smaller than the r_F.
Analog we can determine the momentum number density by integrating 2.14 over position space:

$$n(\vec{p}, T = 0) = \frac{N}{p_F^3}\frac{8}{\pi^2}\left(1 - \frac{\vec{p}^2}{p_F^2}\right)^{3/2} \tag{2.21}$$

with the Fermi momentum p_F. In comparison to the spatial distribution which depends on the aspect ratio of the trapping potential, the momentum distribution is totally isotropic. So also for elongated traps the spatial distribution after long time of flight is radially symmetric.

Finite temperature

To give some approximate solution for the chemical potential, one can expand the Fermi-Dirac distribution around the Fermi edge by the Sommerfeld expansion. For only week derivations from a step function which is the case for $T/T_F \ll 1$ one gets

$$\mu(T, N) = E_F\left(1 - \frac{\pi^2}{3}\left(\frac{T}{T_F}\right)^2\right) \tag{2.22}$$

For large $T/T_F \ll 1$ the exponential function of the denominator far exceeds one, which is why the distribution converges to a Boltzmann distribution that can be

analytically integrated:

$$\mu(T) = -k_B T \ln\left(6\left(\frac{T}{T_F}\right)^3\right) \tag{2.23}$$

The momentum and spatial distribution at finite temperature can only be given in terms of a polylogarithmic function. To calculate the actual values one still needs an expression for the chemical potential. One either could use the previous approximation for the low and high T/T_F limit or utilize a numerical solution. For the actual dependency $n(r, T, \mu)$ and $n(p, T, \mu)$ we refer to [Wen09]. In plot 2.3 we show a numerical solution for different temperatures taken from [Joc09]. The shape of the plotted density distribution is the same for momentum and spatial density, if we have presupposed an isotropic potential. Then the Hamiltonian of (2.13) is symmetric in $\vec{p}$ and $\vec{r}$ and hence yield the same result.
In a weakly interacting two-component gas, the ration of mean field energy to Fermi energy is determined by the interaction strength $k_f a$ with $k_f = p_f/\hbar$. If, for a dilute gas, the inter-particle spacing $n^{1/3} \propto k_f$ is larger than the scattering length ($k_f a \ll 1$), the interaction will not change the density profile of the Fermi Gas drastically. Nevertheless, due to interaction in a Fermi Gas, interesting phenomena like the formation of many-body atom-pairs can occur, which effects has been studied in [Chi04] in the strongly interacting regime. Here, besides of mentioning the effect of interaction, we do not want to go into detail and refer to [Joc09] for further reading.

2.3 Cooling and trapping of ultracold gases

For entering the quantum degenerate regime we are using several established techniques in our experiment. Besides the so called "dimple trick" which we will explain in detail in the following section, these techniques already have been described extensively in previous work [Ser07, Lom08, Koh08]. Thus we here only give a very brief overview of the cooling methods we use, and introduce the optical dipole potentials.

2.3.1 Laser cooling and evaporative cooling

The cooling relies on 2 different mechanisms. The first step, which can cool ^{6}Li atoms from $\approx 1K$ down to $\approx 500\mu K$ is based on Doppler cooling. In this dissipative process an atom with velocity $\vec{v}$ in the presence of 2 counter-propagating laser beams red detuned by a frequency δ to the resonance transition ω_0 of the atom, absorbs photons with a mean energy $\hbar(\omega_0 - \vec{k}\vec{v})$ and spontaneously emits

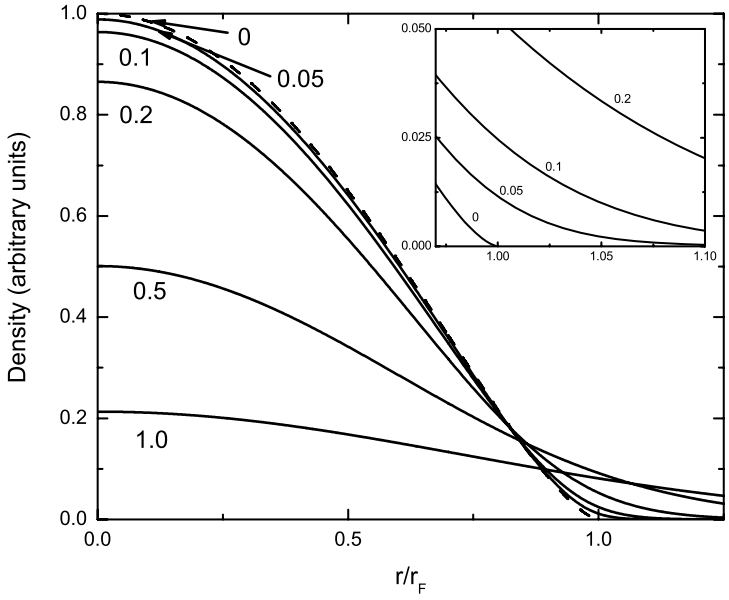

Figure 2.3: Density and momentum distribution calculated for a Fermi gas in an isotropic harmonic trap. The plot is scaled to the expansion at zero temperature which distribution is given by the dashed line. For $T/T_F > 0.5$ the density can be approximated by a Gaussian function. As illustrated in the inset, for small $T/T_F \ll 1$ the distribution exhibits only small variation from which information about temperature can be deduced. The polt is taken from [Joc09]

.

photons with $\hbar\omega_0$. The mean force on an atom can be written by

$$\left\langle \vec{F} \right\rangle = \hbar\vec{k_1}\gamma_1 + \hbar\vec{k_1}\gamma_1 \tag{2.24}$$

whereas the scattering rates γ_1 and γ_2 depends on the line-width Γ of the transition, the detuning $\delta_{v,i} = \hbar - \vec{k_i}\vec{v_i}$ and the saturation intensity of the two counter propagating beams. By inserting the two Lorentzian functions for the scattering rates and linear approximation about $v = 0$ one gets a mean force

$$\left\langle \vec{F} \right\rangle = -\beta\vec{v} \tag{2.25}$$

whereas β is the linear damping coefficient. According to this, if an atom was in the capture range which is the range between the extrema of both Lorentzian, it could be cooled to $v = 0$. However, due to the statistical nature of spontaneous emission, the atom undergoes a random walk in momentum space which heats the optical molasses. In thermal equilibrium we find a temperature of

$$k_B T = \hbar\frac{\gamma^2/4 + \delta^2}{-\delta} \tag{2.26}$$

which exhibits a minimum for $\delta = -\gamma/2$. In combination with a magnetic field the detuning to the resonant transition of different Zeeman Hyperfine sub-levels can be written as a function of position which leads to a position depending force if circular polarized light in different basis for the counter-propagating beams is correctly applied. In this Magneto-Optical-Trap (for details see [Met99]) the atoms are both cooled and spatially confined.
For reaching the degeneracy regime a much larger phase space density than achievable with laser cooling, limited by the photon recoil energy ($E_r = k_B \times 7\mu K$ for the ^{6}Li D-line), is required.
Therefore, we secondly apply the technique of evaporative cooling. Its principle is based on the release of the hottest particles off a trapping potential and the subsequent re-thermalization. If we assume a classical gas with temperature T in an ideal trap with depth U, there will be always a fraction $\exp = -U/k_BT$ of atoms that can escape of the trap and carry away energy $> U$. Descriptively the corresponding energy distribution function is continuously cut at energy larger than U while the residual atoms thermalize, which time constant is dependent on the scattering rate. This process leads to a decrease of the temperature which drops to zero for $N \to 0$. However, in a real trap with fluctuations of the trapping potential and photon scattering in an optical trap, constant heat per particle is induced with a certain rate which limits the lower temperature. So instead of keeping the potential at a certain hight until an equilibrium between cooling and heating is reached - which is called plain evaporation - , one can continuously lower the trap depth such that the fraction $\exp = -U/k_BT$ of particles able to escape, decreases slower. This so called forced evaporation allows for reaching temperatures down to the degeneracy regime. In this regime, further cooling of a Fermi gas is limited by Pauli blocking which considers the fact that the phase space of possible final scattering states is almost completely occupied by fermions and thus the scattering rate converges to zero. For efficient cooling several parameters have to be adapted according to the scattering and heating rate for which more than this conceptional description is necessary. For a detailed quantitative treatment of evaporative cooling we refer to [Luo06].

2.3.2 Optical dipole potentials

For generating our trapping potentials we make use of the dipole force of an atom in a light field. In this external field with intensity $I(\vec{r})$ the ground state of an two-level atom experience a shift in energy, the so called light shift, relative to its unperturbated state due to the coupling to its exited state which is given by [Gri00]:

$$\Delta E(\vec{r}) = -\frac{3\pi c^2}{2\omega_0^2}\left(\frac{\Gamma}{\omega_0 - \omega} + \frac{\Gamma}{\omega_0 + \omega}\right) I(r) \tag{2.27}$$

whereas ω_0 is the resonant frequency of the two-level atom, Γ its linewidth and ω the frequency of the driving light field. If the scattering rate

$$\gamma(\vec{r}) = -\frac{3\pi c^2}{2\hbar\omega_0^2}\left(\frac{\omega}{\omega_0}\right)^3\left(\frac{\Gamma}{\omega_0-\omega}+\frac{\Gamma}{\omega_0+\omega}\right)^2 I(r) \tag{2.28}$$

is small, which is the case for large detuning $\delta = (\omega_0 - \omega)$ the probability of being in the ground state is close to one. Then the potential $U(\vec{r})$ of an atom is given by (2.27) and is spatialy dependent of the intensity of the light field. For a red detuned beam we get an attractive conservative potential. If we keep the ratio of $I/\delta \propto U$ constant, according to (2.28) the scattering rate decreases when we increase the intensity. A small rate is desired since photon scattering leads to heating and loss of atoms of the trap, which is why we will select a large detuning and high power.
A confining potential can be provided by a crossed beam configuration which is in use for our large volume trap or by a single Gaussian beam which provides a cylindrically symmetric potential. The radial confinement is given by the Gaussian beam profile

$$I_{z=o}(r) = \frac{2P}{\pi {w_0}^2}\, exp\left(-2\frac{r^2}{{w_0}^2}\right) \tag{2.29}$$

and the axial confinement is indirectly given by the divergence of the beam

$$I_{r=o}(z) = \frac{2P}{\pi {w_0}^2\left(1+\left(\frac{z}{z_R}\right)^2\right)} \tag{2.30}$$

whereas w_0 is the $1/e^2$-waist of the beam spot and z_r the Rayleigh length. In a harmonic approximation the trapping potentials reads

$$U(r,z) = -U_0\left(1-2\left(\frac{r}{w_0}\right)^2-2\left(\frac{z}{z_R}\right)^2\right) \tag{2.31}$$

with $U_0 = \Delta E(r=0, z=0))$. The radial and axial frequency for an atom with mass m in this harmonic potential are given by

$$\omega_r = \sqrt{\frac{4U_0}{m{w_0}^2}} \qquad \omega_a = \sqrt{\frac{2U_0}{m{z_r}^2}} \tag{2.32}$$

with an aspect ratio of

$$\frac{\omega_r}{\omega_a} = \frac{\sqrt{2}\pi w_0}{\lambda} \tag{2.33}$$

In this thesis we realize a confining dipole potential by a single Gaussian beam, whereas we focus on large trapping frequencies corresponding to a small focal waist, for reasons we will give in the following chapter.

Chapter 3

Towards a few-Fermion System

3.1 Realization of a highly degenerate Fermi gas

On the way towards a finite system of fermions starting from a thermal gas we need to increase the degeneracy of the sample to obtain very high occupation probability of the quantum states in the trap. For the interpretation of future experiments it is crucial not to have any holes - unoccupied states with energy lower than other occupied states - in the Fermi Gas, since we cannot detect them. Interacting particle change the shell structure of the non-interacting case and hence fluctuations of holes in a sequence of experiments would lead to fluctuations in the detected structure, which is why we aim for a high degeneracy. For entering the high degenerate regime ($T \ll T_F$) we make use of the so called "dimple trick", with which we should be able to increase the Fermi energy of some fraction of the particle number while changing the temperature to less extent. This trick has first been used to increase the phase space density $n\Lambda^3$ of a Bose gas in the Boltzmann regime by a factor of 2 [Pin97] (n denotes the spatial density and $\Lambda = 2\pi\hbar^2/(mk_BT)$ the de Broglie wavelength of the gas). In a thermal gas the trick can be descriptively understood by assuming a double box potential with total volume $V_0 = V_1 + V_2$ and identical initial depth. Now the potential depth of box 2 is adiabatically lowered by U. The density in V_2 after being equilibrated at T is increases by the Boltzmann factor. The increase in phase space density of V_2 compared to the initial phase space density of V_0 is given by

$$\ln \Gamma_2/\Gamma_0 = \frac{U/k_BT}{1 + (V_2/V_1)e^{U/k_BT}} \tag{3.1}$$

which was calculated using the condition of constant entropy and constant particle number [SK98]. From that, one can deduce the maximum achievable rise in phase space density to $\approx \sqrt{V_1/V_2}$. In [SK98] this was used to form a BEC by starting from a Bose gas slightly above the critical temperature. By increasing the phase

space density, phase transition in the small volume, in which the potential had been lowered, was realized. Since no heat was induced, a reversible formation of a BEC was possible by adiabatically ramping up and down the tiny potential. In [Joc03b] the dimple trick has been applied to fermions for creating a BEC of ^{6}Li molecules.
For making use of the trick we add an optical potential (section 2.3.2) realized by a tightly focused laser beam to a shallow potential which can be approximated as a harmonic potential. Yet, in the presence of the shallow trap, the potential of the tightly focused beam trap, which we will denominate microtrap in the following, the non harmonic distribution of the Gaussian shape of the beam is not negligible, since it is located in the middle of the Fermi sea. However, a calculation of the density and momentum distribution for this combined harmonic and Gaussian potential seems to be quite challenging. First of all, we are interested in how large the occupation probability of the states inside the trap will be, for which T/T_F is the right indicator. $T_{F,mt}$ of the microtrap can be deduced from the measured trapping frequencies; however, as described in section 2.2.1 , it is hard to determine the temperature for low T/T_F. For giving an idea of the temperature in the microtrap we make the following estimation: We suppose we have a balanced $|1\rangle$ - $|2\rangle$ mixture of weakly attractively interacting fermions which we can realize by setting the magnetic field to a value where the scattering length is small and negative. While both traps, the shallow trap and the microtrap, whose trap depth U_{mt} is set to its final value, are switched on, we apply evaporative cooling by lowering the trap depth of the shallow trap until we have approximately reached a certain ration of N_{mt}/N_s of particles in the shallow trap and the microtrap. The situation is illustrated in figure 3.1. Now we make the assumption that, after some

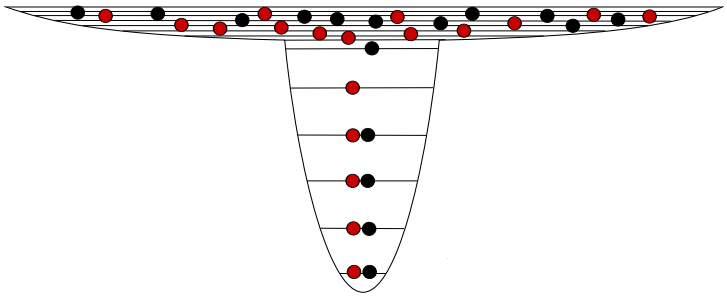

Figure 3.1: Illustration of a two-component mixture of fermions in a combined potential of a shallow and a tight harmonic trap. This "dimple trick" allows for reaching high degeneracy. Under the condition that the fermions in the dimple are in thermal contact to the shallow trap which acts as a reservoir, all fermions are cooled by evaporative cooling of the reservoir. Because of the large Fermi temperature of the combined trap one obtains high degeneracy.

additional sufficiently long time of holding the fermions in the potential, we are in thermal equilibrium. Then we can measure the temperature of the fermions in the shallow trap from which $T/T_{F,mt}$ is inferred. Furthermore, we are interested in the benefit of the dimple trick, which is the gain in T/T_F. To calculate the Fermi temperature of the combined potential we make a simplification in which we neglect the Gaussian shape of the tiny trap and assume a totally harmonic potential for the microtrap. Then the Hamiltonian of 2.13 can be written by

$$H(\vec{r},\vec{p}) = \frac{\vec{p}^{\,2}}{2m} + \frac{m\vec{r}^{\,2}}{2}\left(\omega_s^{\,2} + \omega_{mt}^{\,2}\,\Theta\left[\frac{2U_{mt}}{m\omega^2} - \vec{r}^{\,2}\right]\right) \tag{3.2}$$

whereas we have defined the mean trapping frequency to

$$\omega = (\omega_r^2\omega_a)^{1/3} \tag{3.3}$$

while the indexes denote the shallow trap or the microtrap respectively. We assume that the eigen-energy of the states in the shallow potential is not significantly influenced by the tiny trap. Then the density of states inside the combined potential is given by

$$g(E) = \frac{E^2}{2\hbar}\left(\frac{1}{\omega_{mt}^3}\,\theta\left[U-E\right] + \frac{1}{\omega_s^{\,3}}\,\theta\left[E-U\right]\right) \tag{3.4}$$

From the total particle number, following the calculation for zero temperature, we easily derive the chemical potential

$$\mu = \omega_s\left(6N\hbar^3 - \left(\frac{1}{\omega_{mt}^3} - \frac{1}{\omega_s^{\,3}}\right)U_{mt}^3\right)^{1/3} \tag{3.5}$$

which defines us the desired Fermi temperature $T_{F,c}$ of the combined trap. For typically realised N_{mt}/N_s and ω_{mt}/ω_s the Fermi temperature is mostly dominated by the microtrap, which is why we can approximate $T_{F,c} \approx T_{F,mt}$ (note: $1 - T_{F,c}/T_{F,mt} = 10^{-3}$ for the following parameters: $\omega_s = 800Hz$, $\omega_{mt} = 11kHz$, $U_{mt} = k_B \times 4\mu K$, $N_s = 1.5 \cdot 10^5$, $N_{mt} = 2 \cdot 10^4$). Hence, to calculate the gain in degeneracy we have to compare the Fermi temperature of the microtrap with the Fermi temperature of $N \approx N_s$ particles in the shallow trap at the same temperature:

$$\frac{T_{F,c}}{T_{F,s}} \approx \frac{T_{F,mt}}{T_{F,s}} = \left(\frac{N_{mt}}{N_s}\right)^{1/3}\frac{\omega_{mt}}{\omega_s} \tag{3.6}$$

According to this relation, one could go to arbitrary high degeneracy; however, for very high trapping frequencies of the microtrap, the assumption of thermal equilibrium may not be correct. The region of interaction, given by the spatial overlap

of the wavefunctions of the microtrap and the shallow trap, gets very small for high ω_{mt} and thus thermalization cannot finalize within the lifetime of the sample. For the mentioned values of the trapping parameters and the particle numbers which we expect to realize, one would achieve a gain in degeneracy by a factor of 6 . So if we were able to realize $T/T_{F,s} = 0.15$ in the shallow trap, we would end up with a highly degenerate Fermi gas at $T/T_{F,mt} = 0.025$! We could even reach lower temperatures if we start with a molecular BEC in the combined trap which can be cooled more efficiently by evaporation since Pauli blocking [DeM99] does not occur, which is the case for fermions. Then an adiabatic magnetic field sweep over the Feshbach resonance [Bar04] continuously separates the dimers into free fermions ending up with a degenerate Fermi gas with very low T/T_F. Additionally, we are interested in the occupation probability of the states of the microtrap potential, which is given by the Fermi-Dirac distribution

$$p_o(E_n) = \frac{1}{e^{\frac{E_n-\mu}{k_b T}}+1} = \frac{1}{e^{-\left(\frac{T}{T_F}\right)^{-1}\left(1-\frac{E_n}{E_{F,c}}\right)}+1}. \tag{3.7}$$

By plugging in the derived number of $T/T_F = 0.025$, we get an occupation probability for the upper state in the microtrap potential with $E_n = U_{mt}$ of

$$p_o(U_{mt}) = 0.52 \tag{3.8}$$

which is still far away from 1. However, this is not surprising, since the trap depth of the microtrap is almost equal to the Fermi temperature of the combined trap and thus, the upper level is very close to the Fermi edge. But we still have got a large number of particles left in the trap. Since we want to go to a few-fermion system with ≈ 100 particles, we are interested in the occupation probability of the lowest 100 states. If we find a way to remove all particles with larger energy, without "exciting" the residual atoms, the probability of finding an unoccupied state, is given by

$$p_h(E_{100}) = 1 - p_o\left(U_{mt}\left(\frac{100}{N_{mt}}\right)^{1/3}\right) = 6 \cdot 10^{-15} \tag{3.9}$$

Hence, if the assumption of thermalization was right and if we found a method of removing the residual particles without further excitations, the probability of having a hole would be zero!

3.2 Control of the quantum states

To control the particle number which is required for experiments with few fermions, we need to spill particles off the trap in a controlled way. This also would allow

us to remove the atoms from the non-harmonic domain of the Gaussian microtrap potential. So we have to find a way how to tilt the potential by applying a magnetic field gradient. The energy of atoms with magnetic moment μ in an external magnetic field is given by $\vec{\mu}\vec{B}$. In an offset field $\vec{B} = B_0\vec{e}_z$ the spins are aligned into z-direction. This is why we need a gradient into z-direction. The Hamiltonian for an atom then reads

$$H(\vec{r},\vec{p}) = \frac{\vec{p}^{\,2}}{2m} + \frac{m\omega^2\vec{r}^{\,2}}{2} + \mu\frac{\partial B}{\partial z}z \tag{3.10}$$

which potential is illustrated in figure 3.2 b). A time independent solution for the

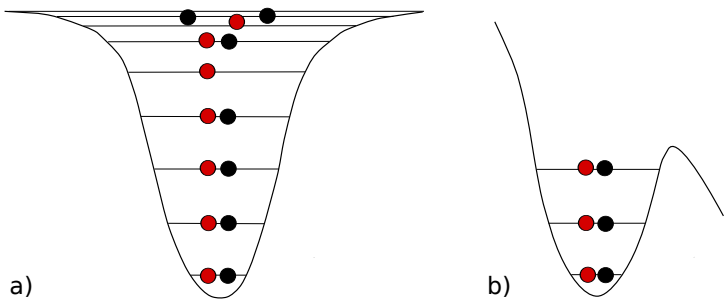

Figure 3.2: a) Illustration of a two-component Fermi mixture filled up to the non harmonic part of the microtrap. b) By applying a magnetic field gradient the atoms can be spilled of the trap in a controlled way. Additionally the deep cut into the Fermi sea removes the quantum states around the Fermi surface which are not occupied. The probability of occupation of the remaining states is expected to be be very high.

particles close to the "edge" of the potential cannot be given since the probability of particles tunneling through the barrier into the continuum is not negligible. To reduce the probability of tunneling the confining potential must we very narrow which is equivalent to a high level spacing $\hbar\omega$. For this purpose we need high trapping frequencies of the microtrap which is extensively discussed in this thesis. If the technique of bending the potential by application of a magnetic field gradient provides the desired control of the quantum states, has to be experimentally tested. A first test of this technique is given in chapter 7. Here we only give an estimation to what extent the particle number can be determined, if we have control except of the upper last shell. Therefore, we assume that the gradient does not significantly change the states of the harmonic potential. For a non interacting Fermi gas in a harmonic potential the degeneracy of a shell is given by:

$$g_n = \frac{1}{2}\left(\widetilde{n}+1\right)\left(\widetilde{n}+2\right) \tag{3.11}$$

whereas $\widetilde{n} = n/\Lambda$, with $n = \Lambda n_x + \Lambda n_y + n_z$ the shell quantum number, defined by the well known harmonic oscillator quantum number n_i. $\Lambda = 1/\lambda$ denotes the aspect ration which we assume to be an integer for simplicity. Then the shell quantum number of the upper last level is implicitly given by the total particle number [O'S09]

$$N = \sum_{n=0}^{n_F} g_n = \frac{1}{6}\left(\widetilde{n}+1\right)\left(\widetilde{n}+2\right)\left(\widetilde{n}+3\right) \tag{3.12}$$

from which we can calculate the particles in the upper shell for $T = 0$ by inserting n_F in (3.11). When we detect the particle number, we do not know whether the particles are already tunneled through the potential "edge" or not. Thus, we take this number as an upper limit for the absolute error in particles. We get a relative error for a total number of 110 particles of 9%, which increases with decrease of particles. Hence, for realizing low particle numbers with an error less than the standart deviation we definetly need control of each quantum state which is why we aim for really high trapping frequencies.

3.3 Few-particle description

If we were able to make this deep cut into the Fermi sea with only a few 10 fermions left, we could not treat the problem in the thermodynamic limit. Presumably we will find that most of the time we measure the particle number, there will be all states filled and only few times there will be some holes in the state spectrum which is a statistical fluctuation of each measurement M. Only in the case of $M \to \infty$ measurements, we would get a distribution given by a fraction of the lowest part of the Fermi-Dirac distribution. So if we had realized a few-fermion system where each state is occupied, the thermodynamic description would not give any further insight. Since the system is isolated from any thermal bath, except of excitations induced by fluctuations of the trapping potential, one could argue we are in the $T = 0$ regime, if the temperature was still an adequate measure. However, to study the system, one has to go back to few-particle description. In the case of non-interacting fermions, one would simply get the eigenstates of the harmonic oscillator. Its shell structure (3.11) would be the first thing to observe which can be done by gradually increasing the magnetic field gradient and by counting the remaining particle number. The more interesting case is when interaction comes into play. Then we are looking for the solution of the Hamiltonian

$$H(\vec{r},\vec{p}) = \sum_{\substack{i,j=1\\ i\neq j}}^{n} \frac{\vec{p}_i^{\,2}}{2m} + \frac{m_i\omega^2\vec{r}_i^{\,2}}{2} + \frac{1}{2}\underbrace{V(r_i - r_j)}_{\text{"}g(a)\ \delta[r_i - r_j]\text{"}} \tag{3.13}$$

which is a few-particle problem and can't be solved analytically without further simplification. However, the interaction can still be described by contact interaction and the s-wave scattering length, which is indicated by the delta-potential. We note that for a correct treatment of such potential, a regularization of the contact potential has to be made [Dal98].
Experimentally one could study how the shell structure changes by the increase of interaction strength. If we were able to modify the potential, for example by realizing a box potential, one could even realize an analog system to different fermionic few-particle systems like nucleons in nuclei or electrons in atoms. One advantage of this system - which might not be as "perfect" as the systems "in real nature" - would be the possibility of tuning the interaction strength which allows to study the physics of the wide range of non-interacting to strongly interacting fermions in an almost arbitrary potential.

Chapter 4

Experimental Setup

In this chapter the apparatus and technique for the preparation of a molecular BEC of ^{6}Li, and a degenerate Fermi Gas respectively, is described. In an UHV environment, lithium atoms, evaporated in an oven and collimated to form an atomic beam, are slowed and subsequently captured by a Magneto Optical Trap (MOT). The cooled atoms in the MOT are transfered to an optical dipole trap where the ensemble is brought to quantum degeneracy by evaporative cooling. This will be starting point for the experiments with few fermions. Additionally, the coil design for creating the large magnetic fields needed to manipulate the interaction properties of the atoms, will be discussed.

4.1 Vacuum and optical traps

The basic concept for our apparatus is keeping the design at the same time as complex as required and as simple as possible. Although all features crucial for our experiment with cold atoms must be properly implemented, any additions that do not lead to an essential benefit for the experiment should be avoided to simplify the operation of the experiment and allow for faster debugging. The basic design is inspired by an experiment run in Innsbruck [Joc03b]. For trapping and cooling use an all optical approach which allows for a high experimental cycle rate. With this, we get the possibility to quickly tune parameters when we are trying out a new experimental procedure. Additionally, a high repetition rate allows for measurements with small statistic errors. In this section gives a brief overview over the vacuum chamber which is explicitly described in [Ser07]. The MOT and dipole trap will be introduced as well, their details are discussed in [Lom08, Koh08].

4.1.1 Vacuum chamber

Due to the possibility of collisions of with background gas, which leads to losses from the trap, the experiments take place in an ultra high vacuum environment. Figure 5.1 gives an insight into our vacuum chamber. An oven is heated up to

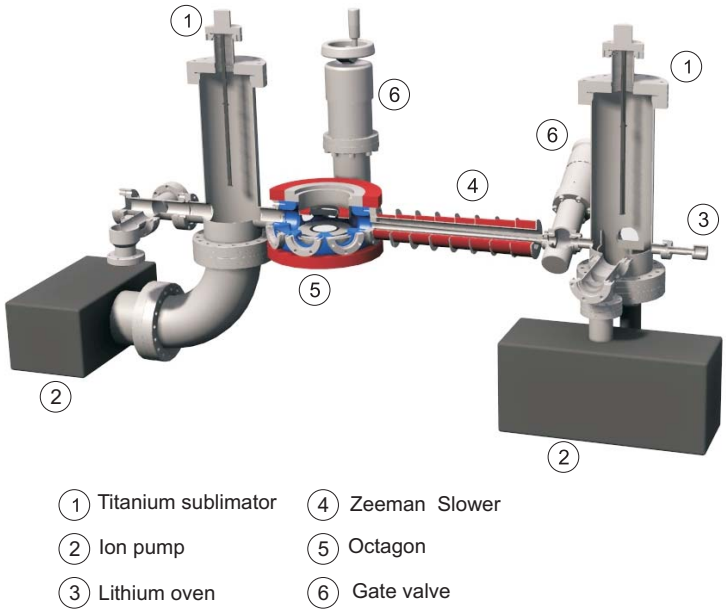

Figure 4.1: Cut through our complete vacuum chamber

$350°C$ to get a large lithium vapor pressure for a sufficient flux of lithium atoms. The vacuum in the oven region is provided by two types of vacuum pumps, a titanium sublimator and an ion getter pump. However, the pressure is limited by outgasing material in the heated oven to $\approx 10^{-10}mbar$. For experiments with few fermions where the atom number is a critical parameter a loss of particles due to background collisions is undesirable. Therefore, the vacuum chamber is divided into two sections; the octagon, our experimental chamber, is separated by a drift tube, which serves as a differential pumping stage, and is at an a pressure on the order of $10^{-12}mbar$. An non-evaporable getter coating [NEG] developed at CERN coated on the octagons' surface decreases the pressure and therefore the number of background collisions. The spherical octagon provides optical access via six CF40 view ports in radial direction and two reentrant view ports in axial direction. The latter allow for a numerical aperture of $NA \approx 0.65$, which is necessary to achieve a high imaging resolution an a small microtrap. Orthogonal to the drift tube a gate valve is connected to the octagon which gives us the opportunity to put further equipment into the octagon or to add a glass cell if better optical access is required some day.

4.1.2 MOT

The divergent atomic beam coming from the oven is collimated by an aperture in the oven chamber and is decelerated by a Zeeman slower. For details to the slower see [Ser07]. At an oven temperature of $350°C$ we get a flux of $10^8 atoms/s$ that we can capture with our MOT. As the number of atoms we transfer into our optical dipoletrap saturates at a number of $10^8 atoms/s$ atoms in the MOT we usually load the MOT only for one second. The MOT consisting of a quadrupole field and light, red detuned to an atomic transition, provides spatial confinement and cooling. However, the achieved temperature is limited by the heating of the sample due to spontaneous emission resulting in a recoil in random direction. For the cooling cycle we use the $S_{1/2}\ (F = 3/2) \rightarrow P_{3/2}\ (F = 5/2)$ transition of the ^{6}Li valence electron. Since the natural line width of the $P_{3/2}$ hyperfine states is larger than the hyperfine splitting, the probability to relax to the $S_{1/2}\ (F = 1/2)$ ground state is on the same order as the decay to the state for the cooling transition. Therefore we need a repumper beam with almost the same power as the cooler. The coherent light for these beams as well as for the Zeeman slower beam is provided by a $500mW$ tapered amplifier (TA100, Toptica) seeded by a grating-stabilized diode lasers. The diode laser is detuned by $(+76Mhz + \omega_{tune})$ via an offset lock in respect to an identical laser stabilized on the $S_{1/2}\ (F = 3/2) \rightarrow P_{3/2}$ transition by Doppler-free RF-spectroscopy of ^{6}Li. The offset lock as well as the spectroscopy are explained in section 4.2.1. The TA beam is divided by a polarizing beam splitter, the relative power of both output channels can be adjusted by a $\lambda/2$ wave plate. The cooler is shifted by $-114Mhz$, half the hyperfine splitting of the ground state, the repumpeer by $+114MHz$ using Acousto Optical Modulators (AOM driver see section 5.1.2). Adding up all shifts the MOT beams are $(38Mhz - \omega_{tune})$ red detuned to the atomic transition. Since the optical setup is located on a separate table to avoid vibrations disturbing the experiment or the laser lock respectively, the light is distributed to the experimental chamber by 3 optical fibers, each for one retro-reflected MOT beam ($P_{out} \approx 40mW$), and a fourth fiber for the Zeeman slower beam. The retro-reflection of the vertical MOT beam is discussed in detail in section 5.1, since it has to share the same axis with the high-resolution imaging and the microtrap. A full review of our MOT is given in [Ser07, Lom08]. A nice feature of our MOT system is that it can be kept running without much effort. The only thing we have to readjust every couple of weeks are the coupling of the seed laser to the TA and the fibre coupling of the beams.

4.1.3 Dipole trap

In the MOT we achieve a temperature of about $500\mu K$ and a phase space density of 10^{-5}. However, to enter the quantum degenerate regime a phase space density of the order of unity is necessary. Since both parameters are limited by dissipative processes, we have to transfer the atoms to a conservative potential. So we can increase the phase space density by evaporative cooling. This works by releasing the hottest atoms from the trap and subsequent re-thermalisation of the remaining atoms the temperature decreases. We can accept the disadvantage of losing an order in magnitude in particle number for reaching high phase space densities, as we want to go to a few particle system. Thermalization of course requires interaction of the particles to interchange energy and momentum. Identical fermions cannot interact at low temperatures as there is no s-wave scattering due to the antisymmetry of the total fermionic wave function; higher partial scattering amplitudes do not contribute as the energy for overcoming the centrifugal barrier is much higher than the temperature of the gas. A system of non identical fermions could be a mixture of two elementary species. However, this would implicate a different oven and slower design as well as a second laser system, which takes an additional effort to built up and maintain. Instead, we use a mixture of two different spin states of the same species, the two lowest Zeeman substate of the ^{6}Li hyperfine state $S_{1/2}$ $(F = 1/2)$, labeled by $|1\rangle$ and $|2\rangle$ in chapter 2.1.1. The two states exhibit a broad Feshbach resonance (2.1.2) around $834G$ which allows tuning the interaction strength by varying the magnetic field. Therefore, we have implemented a pair of Feshbach coils described in section 4.3. To study the physics we are interested in, it is not necessary to use an interspecies mixture. The trapping potential in general could be created magnetically or by optical dipole traps. However, since the lowest Zeeman substates are both high field seekers for fields exceeding $30G$, we cannot trap them magnetically. One could think of a combination of optical and magnetic traps, where low field seeking states are precooled in a magnetic trap and afterwards transfered to an optical dipole trap. Applying Landau-Zeener sweeps could bring the atoms back to the $|1\rangle$ and $|2\rangle$ states. Yet, a conceptually much simpler scheme is to load the atoms directly from the MOT into an optical dipole trap. The properties of such traps for red detuned light are derived in chapter 2.3.2. The trap depth for a Gaussian beam with power P and waist w is proportional to $P/(w^2\Delta)$. Since we need a large detuning Δ to suppress the scattering of trapping light by the atoms, we also need high power to achieve a sufficient trap depth. Therefore, we use a $200W$ Ytterbium fiber laser (YLR-200-LP, IPG Photonics) at a wavelength of $1070nm$. In addition to the trap depth, large spatial overlap of the MOT and the dipole trap is required for an efficient transfer. Hence, the minimum waist of the beam is set to $50\mu m$, which is a compromise between good overlap and high trap depth. Restricting the

trap to only one beam would result in an aspect ratio of radial and axial trapping frequencies of $w_r/w_a = \sqrt{2}\pi w/\lambda \approx 100$. To get a better axial confinement, we reflect the beam back through the same view ports, which is depicted in figure 4.3. The numerical aperture of the viewports allows for a crossing angle of $14°$ resulting in an aspect ratio of 10:1. The trapping frequencies measured by dipole excitations are $\omega_r = 2\pi \times 1650Hz$ and $\omega_a = 2\pi \times 150Hz$ at $1W$ beam power. The beams are linearly polarized which orientation is selected to be perpendicular to each other, otherwise a significant loss of atoms is observed, which is not yet totally understood. The position of the crossed-beam dipole trap can be adjusted by a mirror, mounted on a ultra-stable mirror-mount (KS1D, Thorlabs). Due to the lockable differential drive adjusters the angular resolution is 3μrad. A high positioning resolution and long run stability will be essential for experiments with the microtrap. In resent experiments the crossing and its position has been optimized for particle numbers measured after the transfer to the dipole trap. However, for transferring a degenerate ensemble to the microtrap, the crossed-beam trap has to be aligned for a good overlap with the microtrap since the microtrap is passively fixed in radial direction.
To loose hot atoms during the evaporation process the trap depth is lowered by reducing the beam power over four orders of magnitude. For high power from $200W$ to $40W$ this is done by directly controlling the output power of the IPG laser. In this regime thermal lensing can occur due to the absorption of light, which leads to heating and subsequently to a change of the diffraction index inside the optical material. This effect was extensively discussed in [Lom08, Koh08] and has to be considered when operating at high power. From 40W down to 20mW the power is controlled by an AOM in analog to the scheme described in section 5.1.2. For a detailed description of our production sequence of a degenerate gas, we refer [Lom08].

4.2 Detection

The only observable accessible in our experiments is the spatial distribution of atoms, either in situ, or after a certain time of flight. The detection is done by imaging the atoms onto a CCD camera. From this we can deduce density, particle number and temperature of the atomic ensemble.

4.2.1 Spectroscopy and offset lock

For absorption imaging we use the same optical transitions $S_{1/2} \rightarrow P_{3/2}$ which are used for the MOT. To be able to accurately determine the particle number, the line width of the probe laser has to be much smaller than the natural line

width of $\approx 6Mhz$. Therefore the frequency of the laser has to be stable with a relative precession of 10^{-9}. For this we use a grating-stabilized diode lasers (DL 100, Toptica) which are thermally stabilized and built to be mechanically stable. Since the frequency can jump due to acoustic vibrations and drift due to thermal effects, the laser also has to be actively stabilized by "locking" to the ^{6}Li $S_{1/2}$ $(F = 3/2) \rightarrow P_{3/2}$ transition done by Doppler free rf spectroscopy. The principle of saturated absorption spectroscopy is pumping vapored atoms velocity selective into the exited state and probing their ground state population by a counter-propagating beam [Foo05]. The incoming beam burns a hole into the Doppler broadened number density of atoms in the ground state, at a position where atoms move with a velocity v so that the Doppler shifted frequency is matched to the laser frequency. The retro-reflected counter propagating beam detected on a photodiode is doing exactly the same except for burning a hole where atoms move with velocity $-v$. If the laser is exactly on resonance, the pump beam burns a hole at $v = 0$. The counter-propagating probe sees the reduced density of atoms at $v = 0$ and is passed with less total absorption, resulting in a hump in the detected Doppler valley.
From the spectroscopy an error signal for a feedback loop, which "locks" the laser to the transition, has to be generated. Therefore we use a Pound-Drever-Hall laser frequency stabilization which is explained conceptionally in [Bla01]. The frequency ω_c of the spectroscopy laser is modulated by a frequency $\omega_s = 2\pi\ 20Mhz$ by modulating the laser current which creates two sidebands with $(\omega_c - \omega_s)$ and $(\omega_c + \omega_s)$. The carrier and the sideband experience absorption and phase shifts in the atom vapor, which is considered by the complex absorption coefficient $F(\omega) = E_{abs}/E_{inc}$, where E_{inc} (E_{abs}) is the electrical field of the incident (outgoing) beam. The AC signal recorded on a photodiode is proportional to the beating of the two sidebands with the carrier, where we neglect the beating of the sidebands itself:

$$\begin{aligned} U_{PD} \ \propto \quad & \Re\left\{F(\omega_c)F^*(\omega_c+\omega_s) - F^*(\omega_c)F(\omega_c-\omega_s)\right\}\cos(\omega_s t) \\ & + \Im\left\{F(\omega_c)F^*(\omega_c+\omega_s) - F^*(\omega_c)F(\omega_c-\omega_s)\right\}\sin(\omega_s t) \end{aligned}$$

The real part denotes the intensity difference of the sideband-carrier beatings and the imaginary part the corresponding phase difference. The signal is shifted by an adjustable phase ϕ, demodulated by mixing with the modulation frequency and low passed to eliminate AC contributions to generate the error signal. By varying the phase shift one can continuously tune the error signal from only having an absorptive to only having an dispersive contribution. The error signal exhibits a zero crossing at the resonant frequency which one can intuitively understand, since for this totally symmetric configuration both sideband beatings are equal. For the modulation of the laser current, the demodulation and for the PID controller we use commercial equipment (PDD110, PID110, Toptica). The only self

assembled design of the feedback loop is the photodiode(S9055-0, Hamamatsu), biased with -9V using a bias tee(ZFBT-4R2G-FT+, MiniCircuits) and amplified by an rf amplifier (ZX60-3018G-S+, MiniCircuits). This design has the advantage that one can easily switch from an AC to a DC signal to directly examine the Doppler broadened absorption signal.
The Zeeman sublevels of the hyperfine ground state tune over a range of $\approx 2Ghz$ in a magnetic field up to $1500G$. So our two imaging lasers (two more DL100's) are locked to the spectroscopy laser by beat-offset-locks [Sch99], which allows us to tune the frequency offset by almost one octave. A schematic of our lock is sketched in figure 4.2. For creating the error signal both lasers are superimposed

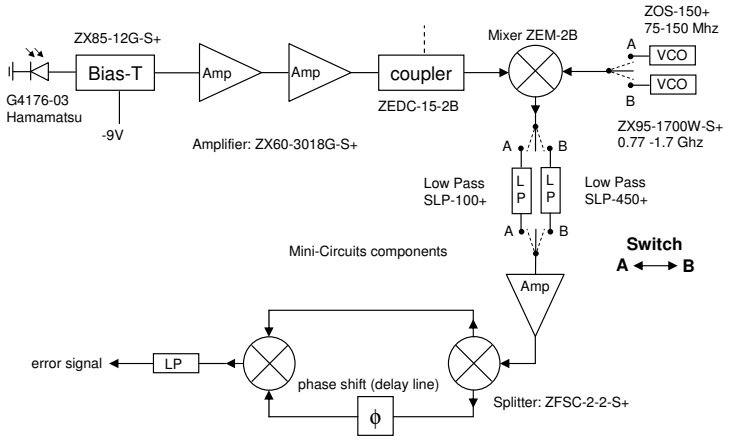

Figure 4.2: Signal processing for creating the error signal for the offset lock. By reversing the switch manually, the frequency range can be selected. After operating the switch, the laser has to be relocked to a new locking point.

on a Photodiode; the beating signal ω_b is mixed with a frequency ω_{vco} from a VCO and sent through a low pass filter to get only the frequency difference. This signal is split up and the signal in one arm is delayed by a coaxial cable with length l, which results in a frequency dependent phase shift $\phi = (\omega_b - \omega_{vco})\, l/c_{cable}$. Then the signals are recombined in a mixer and the output is again sent through a low pass. This leaves only a signal that depends on the phase shift, expressed by the frequency difference to the VCO,

$$U \propto \cos\left((\omega_b - \omega_{vco})\, l/c_{cable}\right).$$

This signal is used as the error signal. The laser is locked to a zero crossing of one fringe of the cosine, which sets the fixed frequency offset. The laser frequency can now be tuned by varying the VCO frequency as long as the ramp speed does not exceed the bandwidth of the feedback loop, so that the change in the lock point can

be followed by the laser. For low field imaging the offset frequency has to be on the order of $100Mhz$ while we need frequencies of $500\,Mhz - 2\,GHz$ for the high field region. A dynamic tuning over the whole frequency range would complicate the circuit. One would need a synthesizer which provides continuous frequency sweeps over the whole range and frequency dependent low pass filters. Instead, we implemented a circuit that can be switched manually between different VCO's and different low pass filters for the corresponding field region.

4.2.2 Imaging in horizontal plane

For the detection we use the well established technique of absorption imaging where we shine resonant light to the atoms and image the shadow on a CCD-chip. The intensity of the beam after interacting with atoms of a column density $n(x, y)$ and cross section σ is given by

$$I(x, y) = I_0(x, y)e^{\sigma n(x,y)}, \tag{4.1}$$

assuming that the intensity is small enough that saturation effects can be neglected. To determine $n(x, y)$ without having to know the intensity distribution $I_0(x, y)$ of the beam, which can include interference patterns, the image is divided by a second image (reference picture) with no atoms present but the same beam settings taken shortly after the first one. A third image (background picture) is taken with the laser light off to help canceling offsets on the CCD. From the optical density

$$OD = ln\left(\frac{I_{abs} - I_{bg}}{I_{ref} - I_{bg}}\right) \tag{4.2}$$

one can calculate the column density by inserting the cross section of the used closed transition $S_{1/2}(m_s = -1/2) \rightarrow P_{3/2}(m_j = -3/2)$ for imaging in the Paschen-Back regime at high fields:

$$n(x, y) = OD\frac{2\pi}{3\lambda^2} \tag{4.3}$$

Since the photon number in the beam have statistical fluctuations (shotnoise) of $\sqrt{N}$, as well as the number of scattered photons, the best signal to noise ratio is achieved for $\approx 50\%$ absorption which corresponds roughly to an optical density on the order of one. Light pulses should be rather short $(1 - 10\mu s)$ to avoid the information of the atoms' position to be smeared out due to the random walk of the atoms during the scattering. To determine temperature, particle number and density distribution the column density is integrated along one direction and fitted afterwards by the corresponding distribution function. Currently we can do imaging in three axes with two different diode lasers. Due to the individually tunable

axis	name	CCD camera label	px-size[μm]	resolution	ϵ	σ-scaling
-90° H	Stingray	AVT Stingray F-033B	9.9×9.9	$\approx$ 4-5μm	σ_x	1/4
-45° H	Guppy	AVT Guppy F-038 B/NIR	8.4×19.6	$\approx 20\mu m$	π_z	1/2
V	Andor	Andor iXon DV 887 DC	16×16	$\approx 3\mu m$	σ_z	1

Table 4.1: Imaging in different axes. H denotes the horizontal plane, V the vertical axis. The axis of the Guppy has an angle of $45°$ to the axial axis of the dipole trap; the Stingray axis is perpendicular to the axial dipole trap axis and shares it with one MOT beam. This is realized by using a reflective polarizer (Moxtec) which retro-reflects the MOT beam and transmits the imaging beam. An explicitly description to this scheme is given in section 5.1.2. Since in the $90°$ H axis the polarization ϵ of the imaging beam is fixed to σ_x by the assembly, only the σ_z fraction of this polarization is scattered. This also applies for the π_z polarization of the $45°$ H axis. Accordingly the cross section σ for the absorption has to be scaled.

frequency of the lasers we are able to image atoms with different nuclear spin states in the lowest hyperfine state at the same time, since in the high field region their splitting of $\approx 80Mhz$ is much larger than the natural line width. For the alignment of the microtrap it is convenient to have imaging in two independent axes in the horizontal plane. When the crossed-beam dipole trap has to be superimposed with the microtrap the positions of both traps have to be determined. With only one horizontal imaging axis one can only trace a line of possible positions. A second independent axis fixes the position in the horizontal plane. The properties of the different imaging axes are listed in table 4.1, the axes in the horizontal plane are depicted in figure 4.3, in which the optics around our vacuum chamber is shown.

4.2.3 High-resolution imaging for detecting few fermions

For experiments with few fermions a high detection efficiency for photons is essential. This is why we use the Andor with an Electron Multiplying CCD with a quantum efficiency of over 0.9. The details on the camera are described in [Wen09]. A useful feature of this camera is the possibility of frame transfer. Half of the CCD chip is covered and therefore not illuminated during imaging. The imaged area of the chip can then be shifted to the covered region. A second image, in our case the reference picture, can be taken instantaneously after the frame transfer which takes about $1ms$ for a frame height of 256 pixels. This time is about a factor of 500 shorter than normally needed for the readout of the CCD until a second image can be taken without frame transfer. A shorter time between

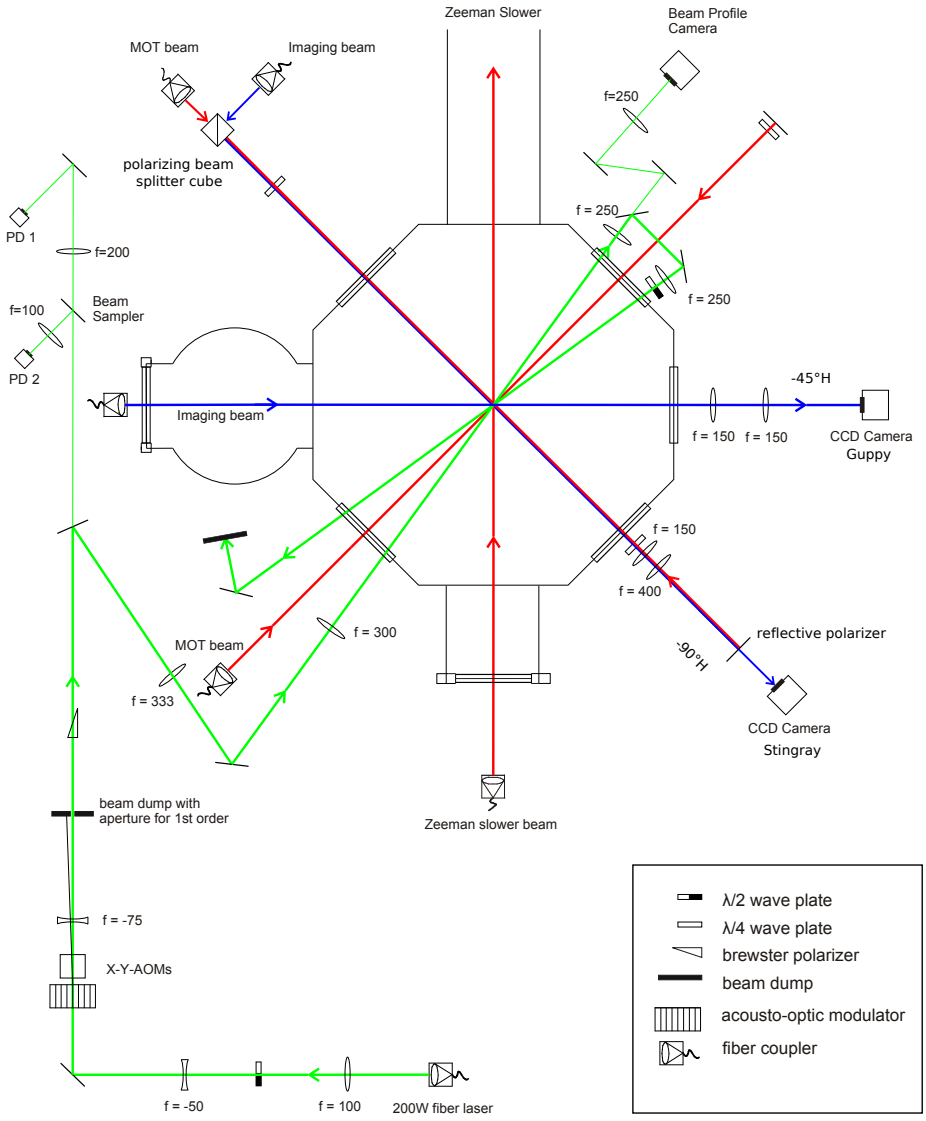

Figure 4.3: View from top to our experimental chamber. The optics and the beams around the chamber for the MOT, the crossed-beam optical dipole-trap and for imaging in the two different axes is shown.

absorption an reference picture is important when interference patterns move between taking these pictures, as they are no longer removed by dividing the images. The axis for high-resolution imaging with large NA was chosen to be vertical. In this direction we have optical access to the ensemble with $NA \approx 0.65$. We image the atoms directly onto the CCD by an aspheric lens without generating an intermediate image. The magnification is fixed by the distance of the object to the

asphere with given focal length. An aspheric lens is needed as otherwise spherical aberrations would occur for this large NA. Such an assembly has crucial consequences on the design of the microtrap, since we use the same asphere to focus into the chamber. The total assembly including the MOT is discussed in detail in section 5.1. Using the asphere described in the microtrap chapter which is available from stock (AL4532-B, Thorlabs), we achive a resolution of $3\mu m$. This is good enough for making in situ images of the atoms trapped in the crossed-beam optical dipole trap; however, the atoms in the microtrap are much more localized. This is why we observe them after release from trap after a certain time of flight. We believe that in the future we will be able to improve the resolution by using a custom designed aspheric lens (see section 5.2.4). But first we want to study the microtrap design and its interplay with the imaging with a standard lens before we order a custom designed lens.

When doing experiments with really few fermions, we will have atom numbers between a few tens and a hundred atoms. Then the cloud becomes dilute after the release from the trap that we will need single atom detection. The information about the few-fermion system is contained in the momenta of the single particles after time of flight. The less particles we detect the more information we loose about our system. But since the optical density is so low, the absorption signal disappears in the shot noise of the imaging beam. So it is difficult to study the few-fermion system by absorption imaging. This is why in future we will have to switch to fluorescence imaging. The idea is to illuminate the atoms from the side and observe the scattered photons. To determine the presence of an atom we have to detect at least one scattered photon if no stray photons are around. As this will not be the case since there will be background light due to scattering at the vacuum view ports, to distinguish a photon emitted by the atom from a stray photon more than one fluorescence photon has to be detected. Since the atoms undergo a random walk after scattering, the second photon might be detected on a nearby CCD pixel. So one will have to look at the correlation between neighbored pixels to determine whether a photon indicates the existence of an atom or is just appearing due to stray light. The probability[Her08] of a spontaneous emitted photon of a transition with change in magnetic quantum number $\Delta m_j = -1$ to be emitted into direction with angle θ to the quantization axis is given by

$$f(\theta) = \frac{3}{16\pi}(1 + \cos^2\theta) \tag{4.4}$$

Hence, the advantage of imaging in direction of spin alignment is collecting twice as much photons than in perpendicular direction. With an numerical aperture of $NA = 0.65$ covering 12% of the total solid angle we should be able to collect 16% of the scattered photons. With our current test assembly ($NA = 0.43$ corresponding to 5% of total solid angle) we could collect a fraction of 7%. So in average

we have to scatter 6 photons, or 14 photons in the case of our test assembly, for detecting one on the CCD. To get a high scattering rate the propability to be in the exited state has to be as large as possible, close to $1/2$; therefore the atom should be driven with several times the saturation intensity. For this we plan to take two counterpropagating laser beams shining in from the radial direction. The power of the beams has to be accurately balanced not to avoid a net momentum transfer from impalanced absorbtion. Still there will be displacement of the atom due to the spontanious emmission of n photons with recoil momentum $\vec{p}_{rec} = \hbar\vec{k}$. Therefore the photon scattering causes a random walk in momentum space. By neclecting the distribution function 4.4 we assume each direction to be equally propable for simplicity. For an estimation of the averaged displacement in one direction we integrate the one dimensional momentum variance:

$$\Delta_x \approx \int \frac{\sigma_{p_x}}{m} dt = \int \frac{1}{3} \frac{\sqrt{n}\, p_{rec}}{m} \frac{dn}{\Gamma_s} = \frac{2}{9} n^{3/2} \frac{2\pi}{\lambda} \frac{\hbar}{m\Gamma_s} \tag{4.5}$$

With a scattering rate $\Gamma_s = 1/2\ \Gamma_{line}$ of $2\pi \cdot 3Mhz$ we obtain $\Delta_x = 1.18nm\ n^{2/3}$. For 14 scattered photons, which we would need with our test asphere to detect 1 Photon on the CCD, we expect a displacement of $60nm$. In a more realistic case where we wanted to detect 10 photons to discriminate from diffused photons we would get an average displacement of $2\mu m$. Then these photons are possibly distributed over few neighbored pixels. To get lower displacement one could also think of Doppler cooling in radial direction, by slightly red detuning the excitation beams.
One way to strongly suppress movement of the atoms over a region larger than the diffraction limit is to capture the atoms in a near resonant lattice. After time of flight the lattice is immediately switched on and the atoms are trapped on one lattice site. The light which the atoms scatter off the near resonant lattice could then be used for detection.

4.3 Feshbach coils

To tune the strength of the interaction between the atoms by means of Feshbach resonances we need a homogeneous magnetic field which can be varied over a wide range. Due to the broad $|1\rangle - |2\rangle$ Feshbach resonance (2.1.2) at $834G$, the scattering length converges slowly to the background scattering length and can be treated as constant at $1500G$. Therefore, if we want to access the whole range of scattering length, a coil design must be able to provide these high field strengths. Especially for creating a molecular BEC we permanently need a field of $760G$; and for doing experiments on the BCS side of the resonance the coils must generate a field up to $1500G$ for a sufficiently long period, which should be at least

$500ms$. The created homogeneous field should be constant over the whole atomic cloud to achieve equal scattering length over the ensemble. Also the Zeemann splittings of the hyperfine states tune with magnetic field. If one prepares all fermions in a single superposition state by applying a rf-pulse, the inhomogeneity leads to dephasing of the fermions at different spatial position ending up in an incoherent mixture due to collisions. Although the inhomogeneity was already used in our experiment to create a three components spin mixture [Ott08], the field should be as homogeneous as possible for studying coherent processes. Furthermore, the inductance of the coils should be small to achieve high ramping and switching speeds of the field. Another main design rule is getting a robust and reliable coil, which is simple to built once a plan has been developed.

4.3.1 Design principle and first generation of coils

The design principle of the coils has already been described in [Ser07, Lom08, Koh08]. Here, a brief overview of the design shall be given together with the measured properties. We will see that the coils of the first generation do not fulfill all requirements and cause some additional problems.
To obtain a homogeneous field, two coils close to Helmholz configuration, where the radius of the coils is equal to the distance of the coil pair, are used. Because the field strength scales with the inverse of the squared distance of the coils one has to place the pair as close as possible to the center of the vacuum cell. This is necessary to keep the needed currents on a level which can be provided with common high current power supplies and to limit the power dissipation in the coil. Additionally a compact design keeps the inductance small, allowing for fast switching of the field. We place our coils inside the to the reentrant view port lowered into the vacuum chamber (5.1). To get a high filling of the limited space, water cooled tube wires are not useful in our setup. We have chosen a solid copper wire with rectangular cross section of $1mm \times 5mm$. This aspect ratio guarantees a reasonable number of loops as well as high filling while the negative effects on the homogeneity of the field are still sufficiently small.
As $B_z \gg B_r$ and $|\vec{B}| = \sqrt{B_z^2 + B_r^2}$ only the field B_z in axial direction has to be considered in the following discussion. In a good approximation the field strength in the $z = z_0$ plane, with the geometric center at $z_0 = 0$, is given by

$$B_{z_0}(r) = \frac{\mu_0}{2\pi} I \sum_{i=0}^{n-1} \int_{-\pi}^{\pi} d\theta \frac{r_i^2 - r_i r\, cos\theta}{(r_i^2 + a^2 + r^2 - 2r_i\, r cos\theta)^{3/2}} \tag{4.6}$$

where $r_i = (r_c + (i+1/2)d)$ is the radius of the i-th loop, r_c the inner radius of one coil, d the distance of two neighbored loops, $a = (b+h)/2 + c$ with b the distance between the two coil surfaces, h the hight of wire, c the radius of the rounding of

the wire including the polyamid coating, and n the number of loops. For the axial magnetic field $B_z(z, r = 0)$ plotted in 4.4 we take a calculation that was done in [Ser07]. Because we are not in an exact Helmholz configuration ($r < b$), we get a local minimum at the center. Since we are working with high field seeking states

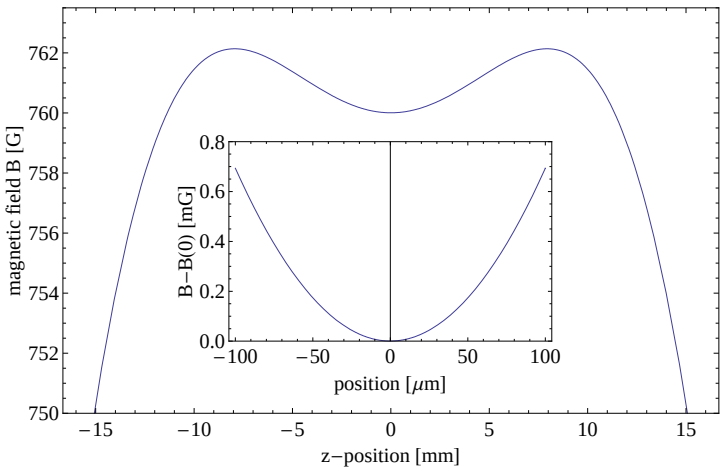

Figure 4.4: Axial magnetic field of the Feshbach coils calculated for a current of $210\,A$ with $n = 15$ and $b = 32.0\,mm$. The value of b has been calculated for the second generation coils mounted to the experimental chamber, by the calibration $B_{z_0}(0)[G] = -0.4598 + 3.6198\,I[A]$, from April 28, 2009. Its increase in comparison with the calculated b for the previous calibration of the first generation coils, is probably due to the larger space between the copper wire of the second generation coils and the experimental chamber. The residual geometric parameters for the calculation are also taken from the second generation coil (see figure 4.8). Although there is a local field minimum at $z = 0$, the inhomogeneity over the atomic cloud is only at the order of a mG.

of the atoms, the field is anti-trapping in z-direction. But the trapping frequency of the magnetic potential is much smaller then the usual radial trapping frequencies of the optical dipole trap. Therefore, effect of the potential only becomes relevant for extremely long time of flight measurements. Having a minimum in axial direction results in a maximum in radial direction (see figure 4.6). Hence the atoms are weakly trapped in radial direction which becomes noticeable if the axial trapping frequency of the dipole trap is on the same order, especially if both potential minima are spatially separated.
The manufacture process starts with winding the coils on a manually operated lathe. For the first generation coils we used a filled epoxy (Stycast 2762FT, Emerson & Cuming) to bond the loops together. We expect a power dissipation of about $1.2kW$ to $1.8kW$ when operating at $1130G$ at a current of $300A$. Therefore our

water cooled copper heat sink, drawn in figure 4.5, must be connected to the coil with good thermal contact, which turned out to be quite challenging. Since the coils as well as the surface of the wire are not flat and the wires are coated with a film of polyamid (thermal conductivity $0.25 W m^{-1} K^{-1}$), the coils have to be machined off to get a bare copper surface and a flatness of the order of $10 \mu m$ for increasing thermal contact. Afterwards the coils are bonded to the heat sink with the filled epoxy, taking care to avoid electrical contact. In a last step the connectors are soldered to the coils with common lead consisting tin-solder.
After mounting the first generation coils to the reentrant view port we calibrated the magnetic field versus the set current. The current is controlled by a feedback loop [Koh08], consisting of a current transducer (Danfysik, Ultrastab866-600) as an input for our $100 kHz$ digital PID controller (chapter 5.3), whose analog output is connected to the coils' power supply (SM15-400, Delta Elektronika). The calibration was done by RF spectroscopy of the transition $|1\rangle - |2\rangle$ which scales with magnetic field. With the calibration, $B_{z_0}(0)[G] = 1.630 + 3.561\ I[A]$, from August 28, 2008, and knowing the coil parameters, we can calculate the surface to surface distance between the coils to $29.5 mm$ by using equation 4.6.
Although the first generation coils had been successfully used for several experiments they exhibit some severe limitations we wish to overcome:

- The magnetic field maximum in the $z = z_0$ plane is located far off center (figure 4.6). Hence the atoms experience a force proportional to the field gradient $\partial_x B_{z_0}(x = 0)$. For a shallow potential of our crossed-beam optical trap with axial trapping frequencies lower than $30 Hz$ this causes the atoms to be pulled out of the optical trap, which is indeed a major problem.

- The coils are getting too hot at fields where we need continuous operation. At $760 G$, i.e. at a current of $213 A$ a temperature of $100°C$ was reached in continuous operation. After half a year of operation this value increased to $160°C$ which is far to hot. We believe that mechanical stress occurring while switching the magnetic field causes the thermal connection of the epoxy between coil and the heat sink to degrade gradually.

- The ohmic resistance between the coil and the connector seems to be too large. We deduce this from observation of melted tin-solder next to the connector.

- Instead of 15 windings for which we have done our calculations, we could only realize 14.19 windings to fit to the reentrant view port, which implies the need of a higher current for the same magnetic field.

4.3.2 Second generation coils

The objectives for the second generation coil were the elimination of the shift of the maximum and the improvement of the power dissipation capability. In detail the following modifications have been done:

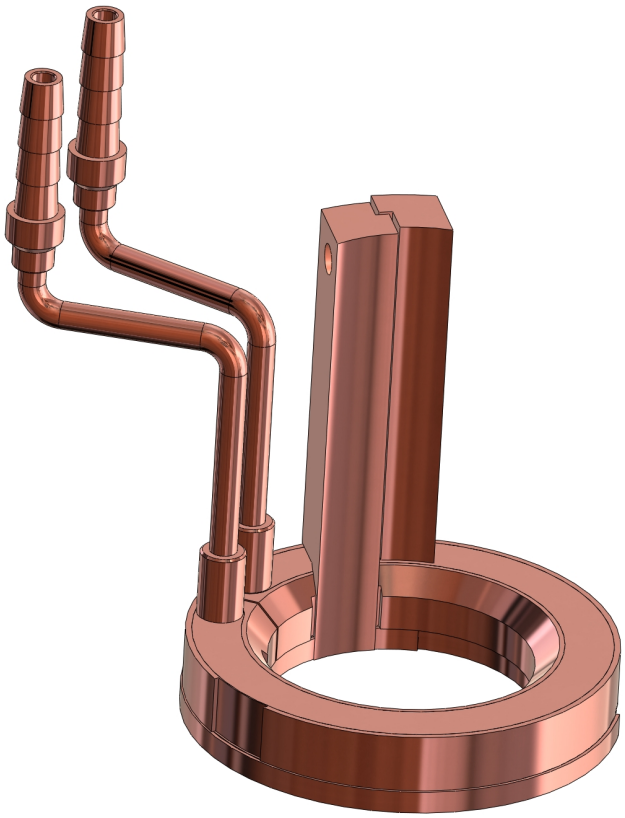

Figure 4.5: Second generation Feshbach coil with connectors and heat sink

Elimination of the magnetic field shift
When we first noticed the shift of the field maximum in the $z = z_0$ plane, we suspected that the field created by the current running through the connectors is responsible. To cancel this effect we wound one of the coils in opposite sense of rotation and reversed the direction of the current. This creates the same homogeneous magnetic field but reverses the current through the connectors. Now the current of the upper and lower coil connectors are running in opposite direction and the sum of their fields vanishes in the $z = z_0$ plane due to symmetry reasons. We haven't done any quantitative calculations for this effect, but after calculating the order of magnitude for other effects, we believe it to be comparatively small.
In the first generation design the two connectors of one coil are radially displaced

simply due ease manufacture. It turned out that this design drastically changes the shape of the field. When displacing the connectors the coil wire has to be overwinded resulting in a non integer number of turns; in our case 14.19 which corresponding to an overwinding of $68°$. Adding another term to equation 4.6 with radius r_n and integration limits equal to the angle of overwinding one finds that the magnetic field maximum is located $8mm$ off center (figure 4.6) from the desired position (figure 4.7)! We are convinced that the gradient created by the overwinding effected the escape of atoms from shallow optical traps. An obvious solution to eliminate the shift is taking an integer number of loops. Therefore the design of the connectors had been modified to be mounted at the same radial position. To fit exactly 15 loops next to the reentrant view port we decreased the effective distance between the loops by using an unfilled epoxy (EPO-TEK 353ND) instead of Stycast. An additional advantage of the unfilled epoxy is the easier machining of the coils.

Improvement of the thermal conductivity between coil and heat sink
Due to the high viscosity of the thermally conductive and therefore highly filled epoxy, excessive glue and air bubbles cannot escape over the large dimensions of the heat sink during bonding. To overcome this we implemented a quadratic, $0.3mm$ deep grid of $3mm$ spacing and 20% filling into the surface of the heat sink. The grid acts as a reservoir into which excessive glue and air bubbles can escape during the bonding process.
Additionally we had been looking for an epoxy which provides higher thermal conductivity while maintaining an electrical resistivity of at least $10^7 \Omega m$. Therefore we have taken some copper samples and tested several selected epoxy. For the test we tried to model the same conditions as we later have for the coil. This means we used the same material - a flat copper surface and a surface with implemented grid- and same curing temperature. Table 4.2 shows the specified thermal conductivity and our test results scaled onto the conductivity of the epoxy used for the first generation. For our application we measured the best conductivity with the diamond filled epoxy Prima-Bond ME7159 (AI Technologies). Obviously this is our new epoxy of choice for the second generation coils, since the other relevant properties such as maximum continiuos operation temperature ($150°C$) and shear strength ($6.9 N mm^{-2}$) are totally sufficient.
Another problem for the old coils had been the relatively high ohmic resistance of the connection between the coil and the connectors. For improvement we use indium instead of conventional solder which electrical conductivity is larger by a factor of 1.4. The lower melting point of indium also allows for lower soldering temperatures which prevents the epoxy from damaging during soldering. The solder joint also acts as an emergency fail-safe: If the temperature of a coil rises above $160°C$, the indium melts, thus hopefully preventing the complete destruc-

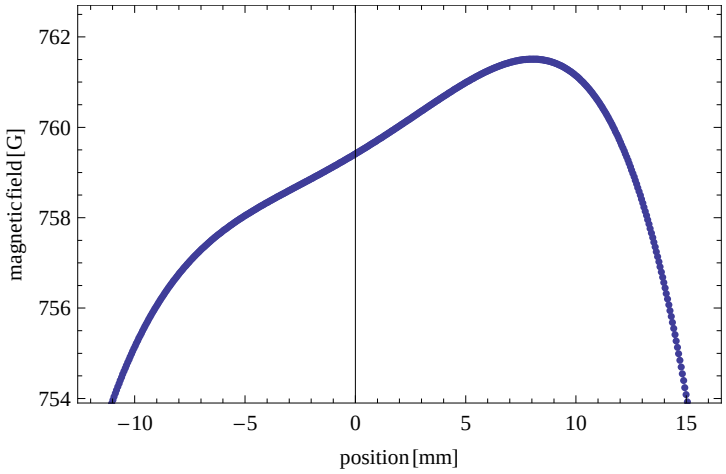

Figure 4.6: Calculation of the magnetic field $B_{z_0}(x)$ with consideration of $68°$ overwinding of the first generation coil. The position x denotes the distance from the geometric center into direction of the overwinding in the $z = z_0$ plane. We get a $8mm$ shift of the field maximum and a magnetic field gradient of $\partial_x B_{z_0} = 300G/m$ at the geometric center. The residual parameters of the first generation coil necessary for this calculation are: $I_0 = 213A$, $b = 29.5mm$, $c = 0.4mm$, $d = 1.26mm$, $h = 4.4mm$ and $n = 14.19$.

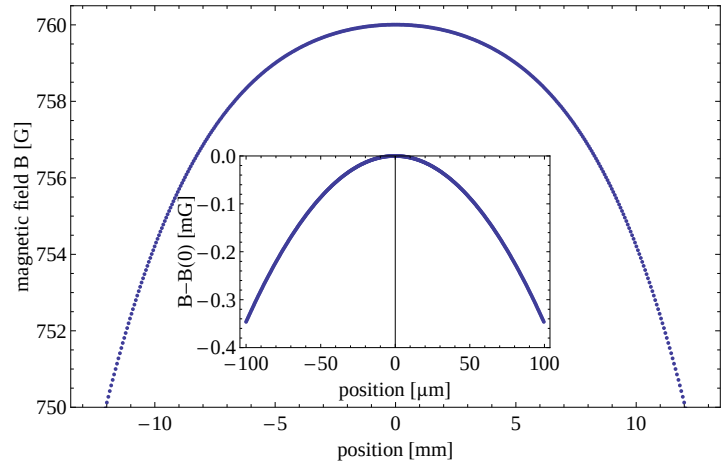

Figure 4.7: Calculation of the magnetic field $B_{z_0}(x)$ for an exact integer number of turns ($n = 15$). The residual parameters for the calculation are taken from the second generation coils which had been implemented to the experimental chamber in April 2009. The actual parameters are listed in the caption of figure 4.4.

epoxy	thermal conductivity		
	manufacturer spec	measurement	
	$[Wm^{-1}K^{-1}]$	Λ $[kWm^{-2}K^{-1}]$	relative
Stycast 2762 FT	1.37	10.2	1
Loctite 315	0.81	6.1	0.6
AIT ME7158	3.6	15.6	1.5
AIT ME7159	11.4	18.2	1.8

Table 4.2: Comparison of four different selected epoxy by measurement of the effective thermal conductivity $\Lambda = j/\Delta T$, with j the heat current density and ΔT the temperature difference between the bond copper samples.

tion of the coil. Additionally, we increased the area of contact by a factor of 1.6 up to $5mm \times 16mm$. Before placing the coils to the reentrant view port, we tried to coat the whole assembly with an insulating acrylic lacquer (Plastik 70, CRC Industries) to avoid electrical contact to the vacuum chamber. However, the acrylic lacquer does not adhere well on copper without undercoating. So instead of the lacquer we used Kapton tape to insulate the connectors from the octagon.

4.3.3 Properties of the new coils

In the following the properties of the second generation coil built with the modifications presented in 4.3.2 are listed. The dimension of the coil are given in the caption of figure 4.8. Plot 4.8a shows the measured temperature of the coil versed the set current. One can see that the new coils are a large improvement over the old ones. The effective thermal conductivity $\Lambda = j/\Delta T$, where j is the heat current density and ΔT the temperature difference between heat sink and coil, is fitted for the hottest and the coldest region of the coil. An infrared image of the coil is shown in figure 4.8b. The discrepancy of Λ between the test measurement and the cold region of the coil by a factor 2 might be explained by a different layer of epoxy due to the asperity of the coil and the heat sink surface.

Knowing the thermal conductivity one can study the dynamics of the coil. The following calculations are done using the conductivity of the hot region. Hence, any following result for temperature will be an upper limit. In a good approximation one can assume that the dissipated power is equal to the time derivative of the deposited thermal energy in the coil plus the heat current. The corresponding differential equation reads

$$R_0(1 + \alpha(T - T_{sink}))I^2 = c_m m \frac{dT}{dt} + \Lambda A(T - T_{sink}) \tag{4.7}$$

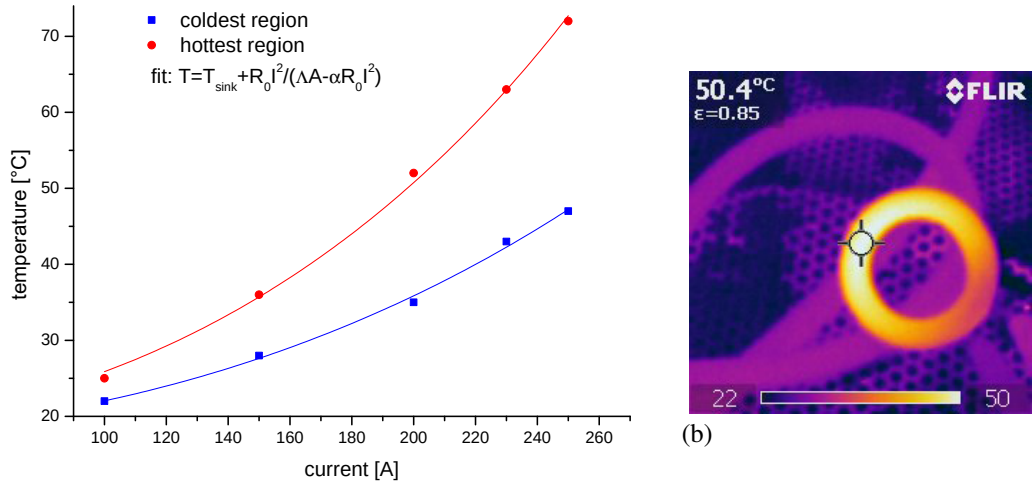

(a) (b)

Figure 4.8: (a) Measured temperature versus set current for the hottest and coldest region of the coil. The solid curve corresponds to the temperature fitted by the free parameters Λ and T_{sink} ($\approx 18°C$). For the effective thermal conductivity one gets $\Lambda_{hot} = 5.46kWm^{-2}K^{-1}$ and $\Lambda_{cold} = 9.24kWm^{-2}K^{-1}$. The other measured parameters of the coil are: $r_c = 28.5mm$, $d = 1.14mm$, $c = 0.4mm$, $h = 4.4mm$, $A = 34,8cm^2$ the area of thermal contact between the coil and the heat sink, $R_0 = 13.6m\Omega$ the resistance of the coil at T_{sink} and $\alpha = 3.9\ 10^{-3}K^{-1}$ the resistive linear temperature coefficient. (b) IR picture taken with InfraCAM Wester (FLIR Systems AB) at $200A$. One can identify the hottest and the coldest region. The coldest region is close to the water cooling connector of the heat sink.

with the solution

$$T(t) = T^* - (T^* - T_0)e^{-\Gamma t} \tag{4.8}$$

whereas $T^* = (R_0 I^2)/(\Gamma c_m m) + T_{sink}$ and $\Gamma = (\Lambda A + \alpha R_0 I^2)/(c_m m)$. In figure 4.9 the temperature for different selected currents versus time is plotted. According to the calculation we expect that we can permanently run $300A$ at a constant temperature of $105C$ while dissipating $1.6kW$ of thermal power. Higher temperatures should be avoided to prevent the vacuum chamber heating up. Furthermore, we deduce that we can run the maximum current of $400A$ for a period of $2.5s$ to reach the $100°C$ limit. The static temperature at this current would be $225°C$ with a power dissipation of $3.9kW$ which would irreversible destroy our coil. Hence, the absolute upper limit for any pulsed operation is equal to the maximum continuous operation temperature of the epoxy and the melting point of indium at $150°C$. For overheating prevention we have implemented a safety circuit that measures the resistance $R(T)$ of the coil and switches the current off

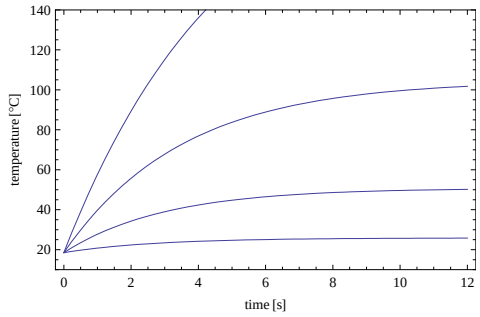

Figure 4.9: Temperature of the Feshbach coil starting with $T_{sink} = 18.5°C$ for different currents.

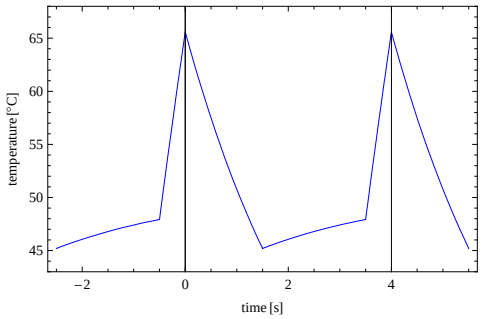

Figure 4.10: Temperature profile of the coil for a typical experimental sequence. [0-1.5]s I=0 MOT loading; [1.5-3.5]s I=200A evaporation; [3.5-4]s I=400A experiment at 1510G

if the temperature limit is exceeded. In figure 4.10 the temperature profile for a typical experimental sequence is shown. It stays below $65°C$ for the whole cycle with an averaged temperature of $51°C$. The simulated sequence was applied to the coils after both had been manufactured. The measured temperature agreed with the calculated temperature within $\pm\, 2°C$.
We conclude that we have developed a coil assembly that can be run permanently at $300A$ to create a homogeneous magnetic field of $1130G$. It gives us the possibility to do experiments on the BCS side of the Feshbach resonance up to $1510G$ for a period of $2.5s$.

4.3.4 Magnetic field gradient

To get to a finite number of fermions, we have to spill atoms out of the microtrap, which we plan to achieve by applying a magnetic field gradient. The strength of the gradient has to be on the order of the trapping frequencies in the direction of the gradient. We can either create the field by our MOT coils which are already in anti-Helmholz configuration or using the Feshbach coils. The advantage of the latter is the higher field strength they can create due to the short distance from the atoms. The low inductance also allows for high ramping and switching speed of the gradient. So far a MOSFET H-bridge is implemented to switch the polarity of one Feshbach coil to change from Helmholz to anti-Helmholz configuration and vice versa. The H-bridge together with a different driver and a modified feedback loop can be used to add a gradient while keeping the strength of the field constant (figure 4.11). The field at the center is given by $B_{z_0}(0) = c_1 I_{c1} + c_2 I_{c2}$, whereas

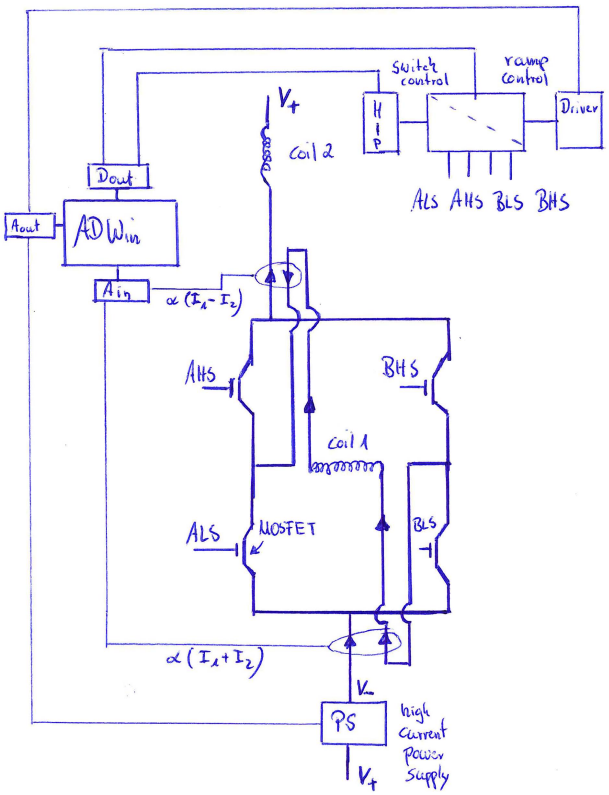

Figure 4.11: Schematic diagram for the stabilization of the offset field and the magnetic field gradient. One of the coils is connected to an H-bridge [Koh08] which allows for reversing the current in this coil (switch control by HIP). An analog driver (to be built) allows for controlling the gate-source voltage of the MOSFETs. Thus, a part of the total current can be bypassed around one coil. Two feedback loops sensing the sum of the current of both coils and the difference stabilize the field and the gradient.

I_{c1} (I_{c2}) is the current of coil_1 (coil_2). If both coils have the same dimension, the absolute field value is proportional to the sum of both currents, which can be used as a signal for a feedback loop setting the current of the power supply. Again assuming same coil dimensions, the gradient at the center is linearly dependent on the difference of the currents. Tuning the gradient can be realized by changing the difference of both currents, which is done by bypassing some part of the current around coil_1 through either MOSFET ALS or BHS. A second feedback loop measuring the current difference and setting I_{c1} stabilizes the gradient. The first feedback loop ensures that the absolute field value stays constant while the current through coil_1 gets modified by the second one. Since both loops are coupled, one has to take care, while setting the PID parameters, that the feedback

loops do not start to oscillate. We calculated that we can achieve a gradient of $0.57\,G/cm \cdot (I_{c1} - I_{c2})$. For an experiment at a field of $1130G$ we should be able to apply a maximum field gradient of $114\,G/cm$ at $I_{c2} = 400A$ for $2.5s$ until the temperature limit is reached. In comparison the axial gradient created by the MOT field is $40\,G/cm$ at a current of $32A$. Adding up both we can achieve a total gradient $150\,G/cm$.

Chapter 5

The Microtrap Assembly

For studying systems consisting of few fermions, we need a harmonic trap with large trapping frequencies in which we can perform experiments with a small number of fermions. The starting point of these experiments is a degenerate Fermi gas in a shallow optical trap at finite temperature. To obtain high occupation probability of states, the level spacing $\hbar\omega$ has to be much larger than the thermal energy $k_B T$. Hence, to fulfill this condition, we need high trapping frequencies. Atom chips with constant magnetic wire traps which provide high trapping frequencies can't be used since we are working with high field seeking states. In our case, the trap of choice is an optical microtrap created by a red detuned focused laser beam at $1070nm$. The atoms are confined in radial direction by the Gaussian shape of the beam, in axial direction by the divergence of the beam. The properties of a focused beam trap are given in the theory part of this thesis in section 2.3.2. In this chapter the assembly and its performance will be described in detail. The following requirements have to be implemented into the design of our trap.

- A small focal waist w_0 of the tightly focused beam is crucial since the radial trapping frequency is proportional to the inverse of the squared waist. Also the aspect ratio of the radial and axial trapping frequencies depends on the size of the waist:
$$\frac{\omega_r}{\omega_a} = \sqrt{2}\,\frac{\pi w_0}{\lambda} \tag{5.1}$$
To achieve an aspect aspect ratio close to one the waist has to be as small as possible, ideally only diffraction limited.

- The microtrap has to be integrated into the existing system with imaging and MOT already implemented. Alignment without changing any settings of these components is wished.

- To vary the trap depth which is proportional to the beam power, we have

to set the intensity of the beam. Noise with frequency on the order of the trapping frequency leads to heating of the ensemble.

First we present the assembly for a small volume trap followed by the determination of its properties. Finally in this chapter the intensity stabilization will be discussed.

5.1 High-resolution assembly

Our high-resolution assembly will be implemented into the vertical axis. An overview of the assembly is given in the cut through our experimental chamber in figure 5.1. What is the motivation to use the vertical axis? The adjustment of the components would be much easier in the horizontal plane if they were mounted on the optical table or on our bread board located $100mm$ underneath the center of the experimental chamber. The homogeneous magnetic field of the Feshbach coils points into the z-direction which aligns the atoms' spin to the same direction as well. As described in section 4.2.3, for imaging we take advantage of the excessive scattering rate into vertical direction. This is why our octagon is designed to have large optical access in this direction. The incident beam for the microtrap should propagate opposed to the scattered photons for not shining trapping light onto the CCD before releasing the atoms. To create the focused beam trap we use the same asphere as we use for imaging. The aspheric lens (AL4532-B, Thorlabs) with a design wavelenth of $780nm$ has an effective focal length of $f = 32.0mm$ (focal distance to flat lens surface: $f_0 = 24.1mm$) and a clear focusing aperture of $37.30mm$ which results in a numerical aperture of $NA = 0.612$. The lens is coated with a broadband anti-reflex coating covering our imaging light at $671nm$ and our trapping light at $1070nm$. We use this aspheric lens from stock, since its parameters fit well to the required parameters given by the dimensions of the octagon and the trapping light although we expect lens aberrations. Yet, an assembly including this lens should give an idea of the potential of the microtrap and should give us the possibility to learn about the obstacles and difficulties on the way towards an optimal setup. We can examine how the alignment and the superimposing of the microtrap with the crossed beam trap works and whether some changes to the design have to be made. However, when we have gained experience, we definitely aim for an assembly where we use a lens or an objective where aberrations are corrected. At the end of this chapter we briefly discuss some simulations for custom designed aspheric lenses.

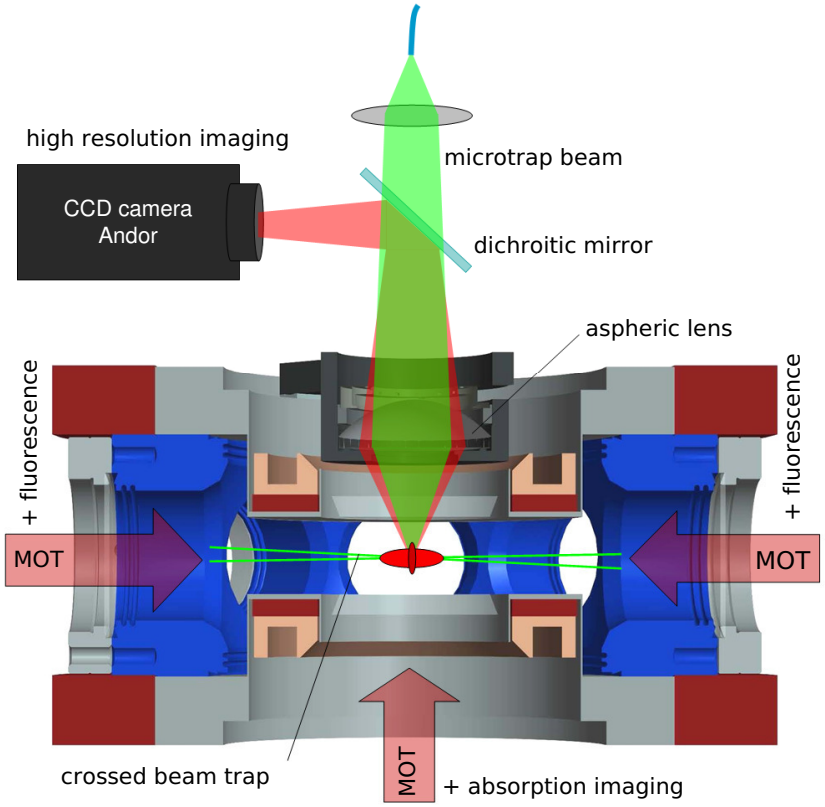

Figure 5.1: High-resolution assembly integrated to our experimental chamber. The atoms trapped by an optical dipole potential created by 2 counter propagating beams crossing at an angle of 14° have to be transferred to a micrometer sized trap. Optical access with high NA is provided from the vertical direction. The aspheric lens is mounted on top of the reentrant view port; a dichroitic mirror separates the imaging light from the microtrap which has to be superimposed with the crossed beam trap. Light for absorption imaging enters from the bottom. For future fluorescence imaging we will use the view ports in the horizontal plane to shine in resonant light.

5.1.1 Beam shaping for the microtrap

For an ideal microtrap a Gaussian beam is required which is focused by the aspheric lens. To get high trapping frequencies we aim for a very small spot size. In a good approximation the waist at the focal point [Sal91] is given by

$$w_0 = \frac{\lambda f}{\pi w_l} \tag{5.2}$$

which is valid for a thin lens using the paraxial approximation $NA < 0.1$. For larger NA a limit of the spot can be given by the diffraction limit,

$$d = \frac{0.91\lambda}{2NA} \tag{5.3}$$

whereas d is defined as the $1/e^2$ width of the 0-order maximum of the spot, achieved by a Gaussian beam which is clipped by an aperture with a radius equivalent to the $1/e^2$ waist of the beam. Hence, the larger the waist of the incident beam, the smaller the spot size we can achieve. For a typial waist of $w_l = 5mm$ we should get a focal waist of $w_0 \approx 2\mu m$ and a corresponding Rayleigh length of $z_R = \pi w_0^2/\lambda \approx 12\mu m$. In principle we could increase the waist of the beam further. However, at some point, the known lens aberration will limit the spot size, which we exactly observe in the test measurement as described later. Since the position of the lens is fixed and the atoms are not located at the focal distance of the lens, we cannot take a collimated beam. The refractive index of the lens' material (S-LAH64) for $1070nm$ light is 0.8% smaller than for $671nm$ which approximately shifts the distance of the focus $250\mu m$ away from the lens. Furthermore the expected distance of the atoms to the lens surface we only know by an uncertainty of $\pm 500\mu m$. Thus, the working distance, which we define as the distance bettween the lens surface and the atoms, has to be adjustable over a range of about $1mm$. The realization is done by using a diverging beam and making an image of a virtual spot whose distance can be adjusted. An illustration is given in Figure 5.2. The light is provided to the experiment by an optical single mode

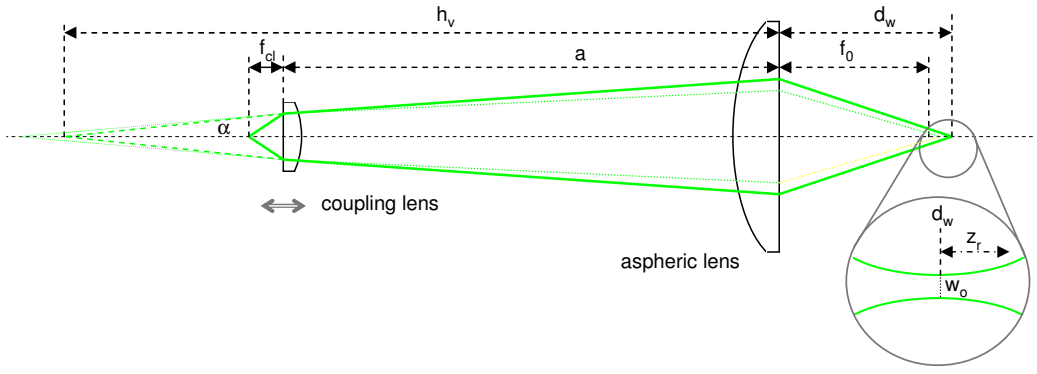

Figure 5.2: Sketch illustrating the beam shaping. For focusing the beam we use an aspheric lens from stock whose focal length f_0 is shorter than the distance to the atoms. Hence the beam has to be divergent. The angle of aperture α is set by an position adjustable fiber coupler lens. We define the distance of a virtual spot h_v which is imaged to the working distance d_w, given by equation 5.4. The zoomed section shows the shape of the beam in the Rayleigh range.

fiber (P3-1064PM-FC-5, Thorlabs). The TEM00 mode ensures a beam with a nice Gaussian profile coming out of the fiber. The beam having a numerical aperture of $NA = 0.1$ is collimated by an aspheric molded glass lens (coupling lens, C560TM-B, Thorlabs) with $f_{cl} = 13.86mm$. A totally collimated beam would be focused by the aspheric lens to the focal distance, so we move the coupling lens towards the fiber to get a slightly divergent beam. At an aperture angle of $\alpha \approx 0.6°$, for the asphere it looks like the light is coming from a virtual spot at distance h_v with waist $w_{cl} = \lambda/(\pi\alpha) = 33\mu m$ and Rayleigh length $z_{cl} = w_{cl}/\alpha = 3.1mm$. The Rayleigh length of th virtual spot is much smaller than its distance to the asphere, so the distance of the image d_w can be calculated in the ray optic limit. As d_w is comparably close to the focal distance, the objective distance h_v has to be large with respect to the focal length. In this regime d_w can be approximated by a series expansion to the first order around $h_v \to \infty$

$$d_w = f_0 + \frac{f^2}{h_v} = f_0 + \frac{f^2}{w_l}\alpha \tag{5.4}$$

By keeping the waist w_l on the lens at its optimum value the working distance can be changed by varying the angle of aperture. This is exactly what we will do to adjust the focal point of the microtrap. Changing α by moving the coupling lens automatically changes w_l. If w_l deviates significantly from its optimum value, it has to be readjusted by moving the coupler inclusively the fiber to a different distance a.

5.1.2 Components of the assembly

The light for the microtrap was originally planned to be coupled out of the $200W$ beam for the crossed beam optical dipole trap. The power of a transient beam of a $45°$ mirror providing $70mW$ should be enough to achieve sufficiently high trap depth for the transfer from the crossed beam trap to the microtrap. However, during the alignment process when the traps are not yet well superimposed, more power is helpful to detect an effect of the microtrap on the crossed beam trap. This is why we use a separate 5W Ytterbium doped Fiber laser (YLM-5-LP, IPG Photonics). To control the intensity of the microtrap we use an Acousto-optical modulator (AOM, 3110-197, Crystal Technology). Thereby light traveling through a TeO_2-crystal is diffracted by interacting with phonons getting momentum and energy transferred from these phonons. The traveling wave of acoustic phonons is created by a piezo-oscillator driven at a center frequency of $110MHz$ at which we can achieve a maximum first order diffraction efficiency of 95%. The intensity of the beam can now be controlled by the amplitude of the piezo oscillation frequency provided by an Voltage Controlled Oscillator (VCO). A schematic

of the driver circuit mainly consisting of commercial RF components (Minicircuits) is given in figure 5.3 which illustrates the optical setup as well. After the

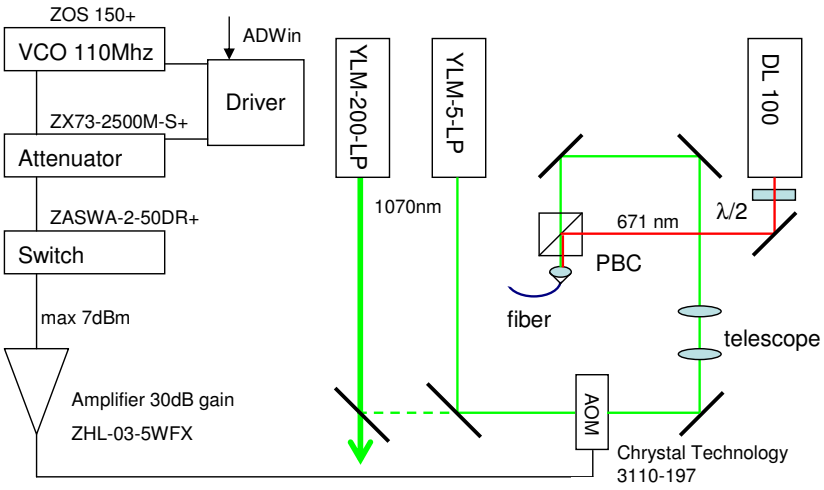

Figure 5.3: Preparation of the microtrap beam. $1070nm$ light from a fiber laser is feed through an AOM for intensity stabilization and switching. After combining with an $671nm$ beam the light is coupled into an optical fiber. Additionally the AOM driver, which creates an adjustable rf signal for the piezo oscillation, is depicted.

AOM a telescope is used for matching the beam diameter to the mode of the fiber. This is a critical issue when high power around $1.5W$ is used, which may destroy the fibre when the coupling is not properly optimised. For the future alignment we also couple a resonant 671nm beam from our imaging laser into the fiber, which now provides both, the microtrap and the resonant beam to the experiment.
As mentioned several times before the vertical axis has to be shared by the following:

- microtrap
- imaging
- MOT

The assembly has to be designed to accumulate all components into one axis. Figure 5.4 shows a draft of the implementation. First the microtrap has to be combined with the imaging which is realized by a dichroitic mirror (15L694000, Laser Components) which is designed to be highly reflective for $671nm$ (99%) and highly transmittive for 1070nm (95%). The introduced fused silica substrate of the mirror with refractive index $n = 1.46$ and constant thickness $d = 6.35mm$ causes

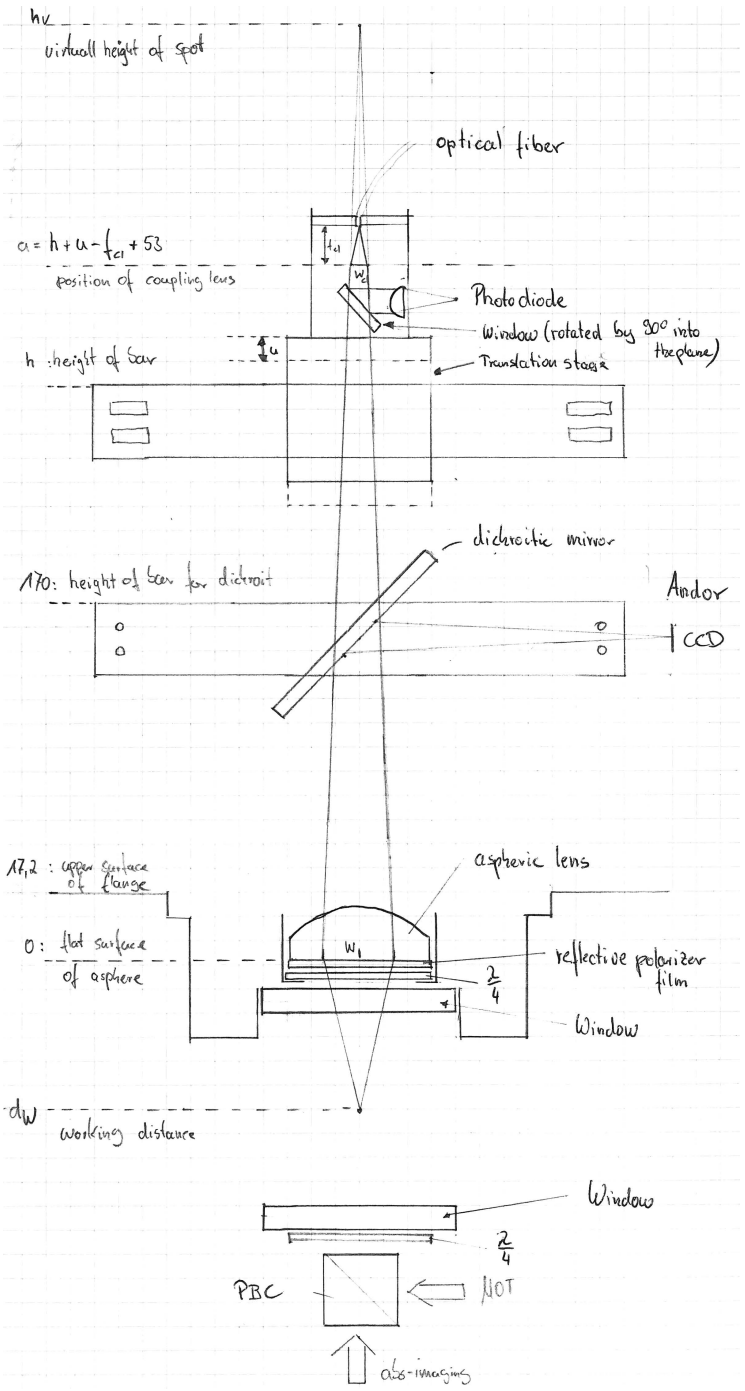

Figure 5.4: Detailed sketch of the whole microtrap assembly in vertical direction. All relevant parameters are indicated, an detailed description is given in the text.

rays incoming with an angle θ to the normal vector of the substrate's surface to be shifted parallelly by

$$s(\theta) = d\left(\tan\theta - \frac{\sin\theta}{n\sqrt{1-\frac{\sin^2\theta}{n^2}}}\right). \tag{5.5}$$

This results in an unequal change of the beam waist in the plane of incidence and in its perpendicular plane

$$\Delta w_{\parallel} = \frac{1}{\sqrt{2}}\left(s\left(\frac{\pi}{4}+\alpha\right) - s\left(\frac{\pi}{4}-\alpha\right)\right) \tag{5.6}$$

$$\Delta w_{\perp} = s(\alpha) - s(-\alpha) \tag{5.7}$$

with α being the angle of the beam divergence which is the same for the transient beam due to the plane parallel substrate. This results in an astigmatism of the focused spot created by the aspheric lens. The shift of the focus in the two orthogonal planes along the beam is given according to equation 5.4:

$$\Delta d_w = f_{eff}^2 \alpha \left(\frac{1}{w_l - w_{\parallel}} - \frac{1}{w_l - w_{\perp}}\right). \tag{5.8}$$

With $\alpha = 0.6°$ and $w_l = 5mm$ we calculate a shift of $34\mu m$. This value is larger than the expected Rayleigh length of $12\mu m$ and hence would drastically change the symmetry of the microtrap. The axial confinement would be washed out over a range of the shift. Therefore we have to compensate the effect of the mirror substrate responsible for the astigmatism.
For stabilization of the trap intensity we need to couple out a part of the beam for the feedback loop. So we planned to take a $3mm$ thick beam sampler (BSF05-B1, Thorlabs) with the same substrate as the mirror and place it into the beam under the same angle of $45°$ but rotated by $90°$ to the orientation of the dichroitic mirror which should reduce the effect of astigmatism by a factor of 2. Unfortunately the beam sampler is wedged by $0.5°$. This changes the angle of divergence differently for the two orthogonal planes along the beam. By that, we would introduce an additional astigmatism of $45\mu m$. As this is not tolerable we had to remove the wedged sampler out of the beam. Instead we use a single sided IR broadband antireflex-coated window made of the same material and thickness as the dichroitic mirror. The astigmatism ideally should now vanish completely. Due to errors of the positioning angle of the mirror and window there could still be a contribution; however, this should be an order of magnitude smaller than the Rayleigh length which does not notably influence the symmetry parameters of the microtrap.
Additionally, the beam for the MOT has to be integrated to the setup. MOT and

imaging light enter the chamber from the bottom combined by a polarizing beam splitter cube. A $\lambda/4$ retarder transposes the imaging polarization to $\sigma-$ and the MOT light to $\sigma+$. After passing the experimental chamber the MOT light has to be retro-reflected. We tested how the beam is influenced when the light was first transmitted through the aspheric lens, reflected by a mirror located at the focal position and sent back through the aspheric lens. The shape of the profile was strongly distorted due to the non perfect focusing and the asymmetric design of the aspheric lens. So the idea of plugging in a reflective element after the aspheric lens is temporarily discarded. Instead we use a much simpler element. We laminated a reflective polarizer film (producer: 3M), normally used in liquid crystal displays, onto the flat surface of the aspheric lens. This polarizer reflects one orientation of linear polarization and transmits the perpendicular polarization with an extinction ratio of 1:1000. MOT and imaging light are retarded again by $\lambda/4$ after coming from the experimental chamber. Both beams are now linear polarized in perpendicular direction. With this low cost and powerful construction the MOT light is reflected by the linear polarizer film and the imaging light is transmitted. The MOT light is retarded once more on its way back to the atoms, ending up in $\sigma+$ light again. This design works very well for the MOT, we do not recognize any change to a mirror construction. However, we have observed, that the film reduces the resolution of the imaging and effects the size of the microtrap unfavorably.
For the microtrap it is essential that the beam position on the lens does not vary during the run of an experiment. Otherwise the position of the microtrap would move. Shaking on the order of the trapping frequencies would lead to heating of the sample. Acoustic vibrations are in the range of expected trapping frequencies. So the mounting of the fiber coupler has to be very stable. Since the microtrap is located in the vertical direction we need a robust construction to mount the fiber and the coupling lens above the experimental chamber. Therefore we designed an aluminum tower with heavy mass which should lower possible vibration frequencies and fasten its damping. Furthermore several bars connected to the horizontal breadboard stabilizes the tower. The coupler and the dichroitic mirror are mounted on bars which can be fixed to the tower at variable height. Additionally the tower is constructed to hold a $300mm \times 450mm$ aluminum breadboard (MB3045/M, Thorlabs) in the case one needs further optics in the vertical direction.

5.1.3 Degrees of freedom for alignment of the trap

With the fiber coupler assembly mounted on a bar at height h above the aspheric lens the angle of divergence has to be set and fine tuning of the distance of the virtual spot h_v is required. Additionally, the angle and position on which the beam hits the lens surface has to be adjustable. A picture of the complete fiber

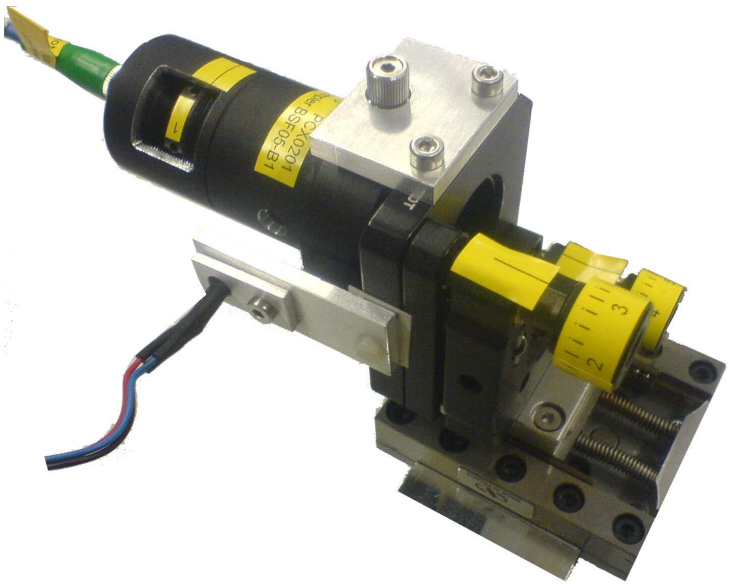

Figure 5.5: Fiber coupler assembly. The coupling lens can be moved inside the lens tube. A special mount not visible on this picture holds a window which compensates the astigmatism effect of the dichroitic mirror and couples out a part of the light for intensity stabilization. The error signal is recorded by a photodiode fixed on the x-y-translation mount for not losing the signal when readjusting the microtrap. The assembly mounted on a standard kinematic mount is located on a stage for fine- tuning the z-position.

coupler assembly is shown in figure 5.5.
The fiber holder is put into a modified lens tube system (SM1, Thorlabs) as well as the coupling lens which is fixed on a mount which can be moved inside the lens tube by rotating the mount. The mount is intersected into 6 parts so the distance of the coupling lens to the fiber can be adjusted in steps of one sixth of a full revolution of the SM1 thread. With this construction the height of the virtual spot can be set. Into the same lens tube assembly the $6.35mm$ window for the compensation of astigmatism and for coupling out a part of the beam is integrated by a custom made 0.75 inch, $45°$ holder which also mounts an 0.5 inch, $f = 20mm$ spheric lens that focuses the out coupled beam on a photodiode (G8370-81, Hamamatsu). The lens tube is screwed onto a x- and y- translation mount (LM1XY, Thorlabs) to precisely align the beam to the center of the aspheric lens. The angle in x and y direction, labeled according figure 6.2 by θ and ξ , under which the beams hits the lens, can be set by a standard kinematic mount. Finally, for fine adjustment of the distance of the virtual spot, the assembly is mounted on a precision translation stage (M-UMR5.16, Newport) which can be moved over a

range of $15mm$ into z-direction.
To sum up we have enough degrees of freedom to adjust the position of the focal point in 3D. In the following we want to study quantitatively how the degrees of freedom effect the position and the size of the microtrap.

5.2 Properties of the microtrap

A basic prerequisite for the achievement of atom transfer from the crossed beam optical dipole trap and for low losses inside the microtrap, is that the beam of the microtrap exhibits same parameters as predicted. Additionally, we wish to know the expected trapping frequencies which can be calculated from the measured waist and from the beam power. Another question tried to be answered is, if in principle we will be able to control the atom number with the used aspheric lens and go for a few-fermion system. Furthermore, for superimposing the microtrap with the crossed beam trap, we need to determine the focal position dependent on the settings of the assembly. So before implementing the assembly into our experiment we tested it in an external test setup. Therefore, we ordered a second identical aspheric lens, as with the removal of the first asphere, the high-resolution imaging and the MOT would also be unmounted. However, for the first test we excluded the polarizer film in order to get the information about the asphere unperturbed by the polarizer. Additionally we left out the $\lambda/4$-retarder simply due to the non availability of a second with the same thickness, but we considered the influence on the working distance by its refraction. For the test we use the fiber coupler assembly described 5.1.2 which we will later implement to the experiment.

5.2.1 Test measurements

To determine the properties of the beam we have to measure the beam profile at different spatial position. Since the waist at the focal point is too small for detecting directly with a CCD beam profile camera, we apply an indirect measurement of the profile by the following method: We block a part of the beam at a position along the beam by a sharp edged plate and measure the residual transmitted light. Then the intensity of the beam detected by the photodiode reads

$$I_{pd} = I_0 \int_x^\infty \exp\left(\frac{-2(x-x_0)^2}{w^2(z)}\right) = I_0\left(1 - \mathrm{erf}\left(\frac{\sqrt{2}}{w(z)}(x-x_0\right)\right) \tag{5.9}$$

with erf being the Gauss error function, x the position of the plate, x_0 the center position of the beam and $w(z)$ the waist of the beam at a certain position in

z-direction. We note that the value for the waist we measure is defined by the distance from the center where the intensity has dropped to $1/e^2$. To fit the function to a set of measurements we need to record several intensities for different x-positions of the plate. Instead of moving a plate manually into the beam and record the intensity individually, we move the plate with constant velocity through the beam and measure the time evolution of the intensity. Knowing the velocity of the plate we can substitute time by the spatial position and fit equation 5.9 to the measured data. For the plate we use a razor plate which provides a sharp and straight edge which is crucial for not distorting the intensity signal. The plate is mounted onto a motorized Micro-Translation Stage (M-111.2DGX, PI) which can be automatically moved into x-direction in multiples of the design resolution of $8.6nm$. This stage is mounted onto another manually operated stage setting the z-direction. For detection of the beam intensity we use a photodiode (S1722-02, Hamamatsu) with a large active area to collect all light since the beam is strongly divergent. The first test run showed that the beam is not perfectly Gaussian and exhibits small wings on the outer region of the Gaussian. As one can see in figure 5.6 the fit of the error function is sensitive to the deviations in the outer region of the Gaussian and does not fit the slope corresponding to the center region that well. Since we are interested in the waist we reduced the weight of the wings compared to the center by fitting the derivative of 5.9, a Gaussian, to the modified set of data. To fit the derivative, each data point is subtracted by its previous, which can be done without taking care about the temporal spacing of the points as the amplitude is not a relevant parameter. One only has to ensure that the difference in the region of interest is an order larger than the fluctuation of the data points. This can be realized by setting a suitable razor plate velocity and sampling rate for the detection. By applying that method as shown in figure 5.7, we believe we can determine the waist with an relative uncertainty of about 10%. One source of error that has not been studied quantitatively might also be defraction at the razor plate which causes some light not beeing detected on the photodiode. However, other aspects like the exact positioning of the manually operated stage are a larger source of errors but still small enough to determine the waist with a sufficient accuracy.

Minimum focal waist

The parameter of main interest is the waist at the focal point which determines the radial trapping frequencies and the Rayleigh length determining the axial frequency.
Before starting a run - a run is the procedure of driving the plate through the beam as described - the waist of the aligned incident beam is measured at 2 different position with a beam profile CCD cam (U2382, WinCamD) to get the waist w_l of the

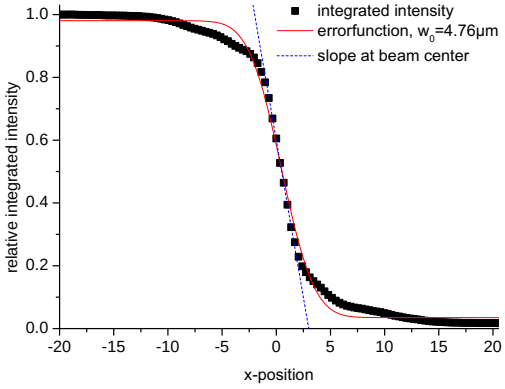

Figure 5.6: Intensity recorded by the photodiode while moving the razer plate through the beam. The temporal dependency is already substituted by the spatial position. The fit of the error function does not fit the slope at the beam center very well due to derivations in the outer region.

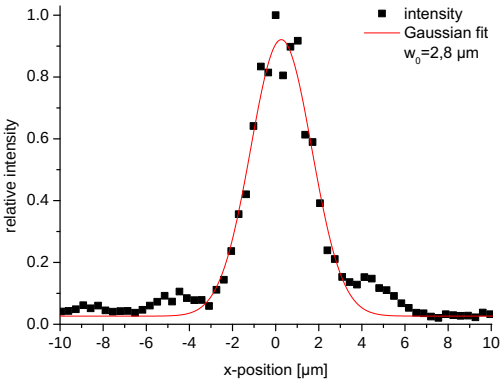

Figure 5.7: Derived intensity profile from left hand side figure. The Gaussian fits the intensity at the center quite well. The waist of the beam at a certain z-position is deduced from this fit. Wings occurring from lens aberrations are clearly visible.

beam on the asphere (extrapolated to its plane surface) and the angle of aperture. Additionally the manually operated stage is moved to the z-position going to be observed. From one run we can determine the waist as seen in figure 5.7. The first measurement was done to determine the optimum waist w_l of the incident beam with which we achieve the smallest spot size. Figure 5.8 shows the result from which we deduce an optimum waist of $w_l = 5.1mm$. For larger incident beam waist, lens aberrations occur and the spot size increases again. After determination of the best incident beam waist for the experiment, we also use this constant value for all further test measurements. At an angle of aperture around $\alpha = 0.6°$ we determine the minimum waist we can achieve to

$$w_0 = (2.98 \pm 0.26)\mu m$$

with a statistical error calculated from 6 individual measurements.
Knowing the focal position we are now able to map the beam waist around the Rayleigh range. Therefore we do several runs for different z-position. From figure 5.9 we can deduce the Rayleigh length:

$$z_R = (26 \pm 5)\mu m$$

which is in agreement with the expected Rayleigh length of $27\mu m$ calculated from measured waist w_0! The data show a non symmetric beam with a stronger diver-

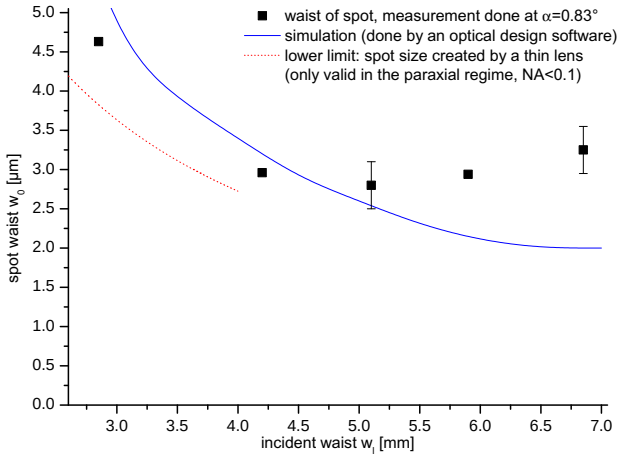

Figure 5.8: Focal waist dependent on the waist of the incident beam. From the measurement we determine an optimum waist w_l of $5.1mm$. The doted red curve shows the waist expected for a thin lens (5.1). This approximation is only valid in the paraxial regime for $NA < 0.1$. The blue curve shows a simulation done with the lens coefficients given by the manufacturer. The glass plate is also considered. Lens aberrations occur for rays with larger distance from the optical axis. Further aberrations occur, since after the lens, the strongly convergent beam passes a glass plate in the test setup, which simulates the window of the vacuum chamber in the experiment.

gence than expected for a Gaussian. This could tell us that the beam is not optimal shaped after the transmission through the lens and the window.

Working distance

For the later superposition of the microtrap with the crossed beam trap we need to know how we can set the working distance of the microtrap to the actual distance of the atoms. Since the incident waist is fixed we determined the dependency of the working distance by the angle of aperture. From figure 5.10 we can deduce the working distance for small angle of aperture to:

$$d_w = 27.1\ mm + 4.5\ mm/^\circ \times \alpha$$

The linear dependency is an approximation for small values of α. The fitted slope is in the range of the expected value from equation 5.4 which is $3.6\ mm/^\circ$ for the parameters we used. Course adjustment of the working distance is done by setting the angle of aperture. Fine tuning the microtrap to the position of the atoms is done by the translation stage. Moving $1mm$ on the stage translates to a $-6.4\mu m$ shift in working distance. This is only valid for a certain angle of aperture

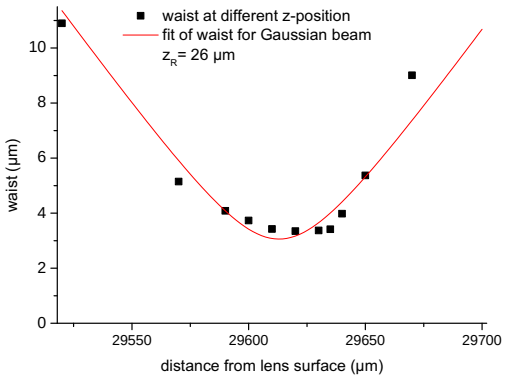

Figure 5.9: Waist of the beam around the minimum beam size. The measurement is fitted by the waist for a Gaussian beam $w(z) = w_0\sqrt{1 + (\frac{z-d_w}{z_R})^2}$

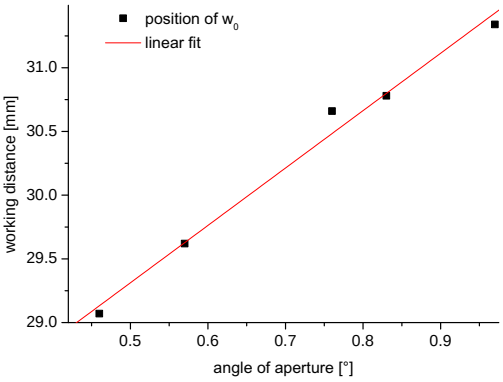

Figure 5.10: Working distance dependent on the angle of aperture α. The linear fit with a slope of $4.1\ mm/°$ is an approximation for small α.

($\alpha = 0.73°$) because of the reciprocal dependency of the working distance on the distance of the imaged object. In a real performed experiment with trapped atoms we have seen that we can move the atomic cloud by $2\mu m$ per $1mm$ for $\alpha = 0.5°$. For alignment of the microtrap it is convenient to know the difference of the focal position of $1070nm$ light and $671nm$ light coming from the same optical fiber at a typical height h = $300mm$. The shift which occurs due to the different refraction amounts $40\mu m$ while the assembly is kept in constant position. Adapting the parameters for the incident beam we get a shift of $200\mu m$. Since the refraction index of $671nm$ light is larger, the working distance is closer to the lens surface, which has to be considered when resonant $671nm$ light is used to determine the vertical position of the atoms with respect to the lens.

Horizontal position

Further information we need for alignment is the change of the spot location in the horizontal plane by the variation of the angle of incidence and the beam offset from the optical axis. Figure 5.11 and 5.12 depict the relation which had been measured for an angle of aperture of $\alpha = 0.57°$. For large offsets on the order of $2mm$ the beam is focused not very well anymore which manifests in a bigger waist. Large angles of incidence increase lens aberrations which is getting noticeable in the rise of the wings in the outer region of the profile.
An additional remark on position has to be made which is relevant for the alignment process: The coupling lens we use is not perfectly radially-symmetric mounted in the rotational mount. A change of its radial position also varies the angle of incidence. So after rotating, the beam has to be readjusted to the correct angle of

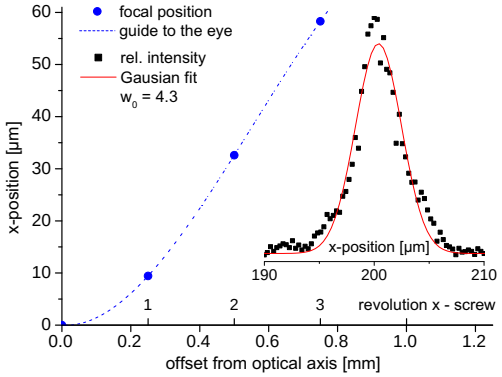

Figure 5.11: Position of the microtrap dependent on the offset from the optical axis. The inset shows that the waist of the focal position increases with larger offsets compared to the on axis waist of $3\mu m$.

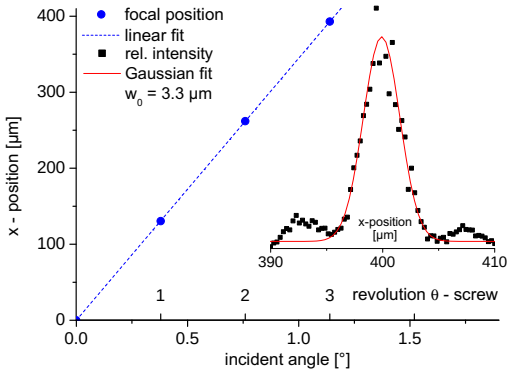

Figure 5.12: Position of the microtrap dependent on the angle of incidence. For large angles the rise of the wings due to increased lens aberrations can be seen in the inset.

incidence.

Reflective polarizer

As mentioned in the beginning of this section we have done the previous test measurements without the reflective polarizer film to get an idea about the possible capability of the microtrap using the aspheric lens from stock. However, during the experiment we need the reflective polarizer to create the MOT. So we also applied a measurement with a reflective polarizer laminated onto the lens. The polarizer film adds further not totally understood distortion which results in a minimum achieved waist of about $3.7\mu m$. One reason might be the observed ripples on the polarizer surface visible with the eye which could introduce wave front distortion. An alternative reflective polarizer from Moxtek which we have already in use for one horizontal MOT beam yields not a better result. Also the Moxtek polarizer worses the waist about $1\mu m$.

5.2.2 Calculated trapping parameters

From the measured results we can calculate expected parameters of the microtrap like trap frequencies or trap depth equations derived in section 2.3.2. For a waist of $3.7\mu m$ and a beam power of $0.5mW$ we expect a trap depth of

$$U = 1.4\ \mu K.$$

$$\omega_r = 2\pi \times 3.8\ kHz$$

$$\omega_a = 2\pi \times 250\ Hz$$

are the corresponding radial and axial trap frequencies resulting in a mean trap frequency of $2\pi \times 1.5kHz$ and an aspect ratio of 15. The level spacing in axial direction for this configuration is $\approx 2nK$. If it is possible to spill atoms only of single shells while tilting the trap by applying a magnetic field gradient, can not yet be told exactly and has to be studied in the experiment.

5.2.3 Conclusions from the test measurements

From the test measurements we obtained various information for the alignment and about the possible performance of the microtrap.

- The achieved focal waist is limited by lens aberrations to $3\mu m$. If one wants to further increase the resolution one needs to design an achromatic lens system with consideration of the window in the convergent beam.
- The spot size is minimized for an incident beam waist of $w_l = 5.1mm$. It is not a too critical parameter for the setup of the microtrap, since the spot size only slowly increases for small deviations from the optimum.
- For a beam profile with less wings it is crucial to keep the incident beam on the optical axis. Only within a small range the deviations are acceptably small. This has direct consequences on the alignment routine for superimposing the microtrap trap with the crossed beam trap. By keeping the beam on the optical axis the horizontal position of the microtrap is totally fixed on the position of the lens. So either the crossed beam trap or the aspheric lens has to be rearranged for getting the required spatial overlap.
- The reflective polarizer worses the resolution of the microtrap. So far we tolerate this but take advantage of the compact design. In future when we want to go for smaller trap sizes, we have to find a new idea how we retro reflect the MOT beam without affecting the resolution of the imaging and the microtrap.

5.2.4 Future improvement and simulation

Although we will use this design of the microtrap to perform the first experiments with highly degenerate Fermi gases, one can regard it as test assembly for learning more about the properties of such a microtrap system. We will identify redundant degrees of freedom as well as further degrees of freedom we would like to have.

lens	AL4532-B, Thorlabs		designed asphere	achromatic objective
	measurement	simulation	for $1070nm$	$1070nm$ and $671nm$
$w_l[mm]$	5	6	-	-
NA	(0.13)	(0.13)	0.65	0.5
$w_0[\mu m]$	3.0 ± 0.3	2.0	0.75	0.97

Table 5.1: Comparison of the optical capability of the actual microtrap design with simulations done for different lens systems. The custom asphere is only designed for 1070nm and diffraction limited (5.3). In the last column a simulation for an achromatic objective is listed, which consist of 6 individual lenses. The spot size is the same for both wavelength. The simulation was done by Friedhelm Servane by means of an optical design software (Oslo Premium 6.4, Lambdares).

Limitations, such as the linear polarizer film, can be realized and improvements be done. Additionally, we first want to experience, how good the transfer of the atoms from the crossed beam trap to the microtrap works, before we implement a more sophisticated assembly.
Also, with this actual design, we never had the ambition to reach the diffraction limit given by the NA of our vacuum chamber. In a new design the resolution of the microtrap will surely be larger. To give an impression what spot size we could reach, some simulations for different designs of a possible microtrap assembly are listed in table 5.1. For example with a custom designed diffraction limited aspheric lens we could reach a spot size of $0.75\mu m$. Currently, Friedhelm Servane, who has done the simulations, is working on a design for a second generation microtrap. The experience we get from the actual microtrap, will have impact on the new design.

5.3 Intensity stabilization

For an ideal microtrap the intensity of the beam should be constant in time. However, in real experiments there are always sources of noise creating contributions in various frequency ranges. The laser itself generates not a totally constant output power. Long term drifts depend on temperature; higher frequency noise arise from noise of the pumping diode current. Opto-mechanical equipment like mirrors and lenses can vibrate on the optical table and create acoustic noise since the variation of the beam path changes the coupling to the optical fiber as well. Fluctuations of the polarization is translated into power noise when a polarizer or a polarizing beam splitter is in the optical path.
But not all sources effect the performance of the microtrap equally. One has to distinguish between different frequency ranges referring to the trapping frequency

to tell if the noise is critical:

- Frequencies lower than the trapping frequency do not effect temperature and lifetime of the trapped ensemble. The atoms can follow the change of the potential induced by the intensity noise adiabatically, no heat is deposited to the atoms.

- Frequencies on the order of the trapping frequency lead to heating of the atoms. The change of the potential is faster than the ensemble can expand and increase its volume. The internal energy and temperature rises which results in loss of atoms and decreased lifetime.

- Frequency noise larger than the trapping frequencies does not influence the state of the atoms. Since the speed of the time evolution is given by the trapping frequencies, the atoms only see the time averaged potential created by the high frequency noise.

Hence we have to concentrate on noise up to $30kHz$ since the expected radial trapping frequencies are about $3kHz$ at a trap depth of $1\mu m$. All lower frequencies will also be covered in the experiment when the trap depth is getting lowered. We want to damp the noise by an active intensity stabilization. Therefore we use the AOM assembly described in section 5.1.2. The time constant for switching light is given by the sound velocity with which the phonons travel through crystal and the waist of the transmitted beam. The reaction delay is the time the phonons need from the crystal surface to the beam. For a delay of $0.5\mu m$ and a maximum phase shift of π between the source and its feedback, the bandwidth limit of the AOM is $1Mhz$, enough for our application. We detect the process variable, proportional to the intensity of the beam, by a photodiode, whose bandwidth does not have to be larger than the one of the AOM. At last for stabilization the feedback loop is closed by a PID controller.

5.3.1 Digital PID controller

We implemented a digital PID controller to stabilize different variables of our experiment. Therefore we use a real-time processor (Sharc-DSP @ 300Mhz) running on a controlling system (ADwin Pro II System, Jaeger Messtechnik) with analog and digital IO modules. The processor continuously executes a program code within its process delay of 3000 processor cycles which is equivalent to $10\mu s$. Within this time the value of the photodiode is read out, compared with the set point and an output value is generated. The output signal consists of 3 parts: The P-fraction is proportional to the error which is the difference between the setpoint and the process variable. The I-fraction is proportional to the sum of the current

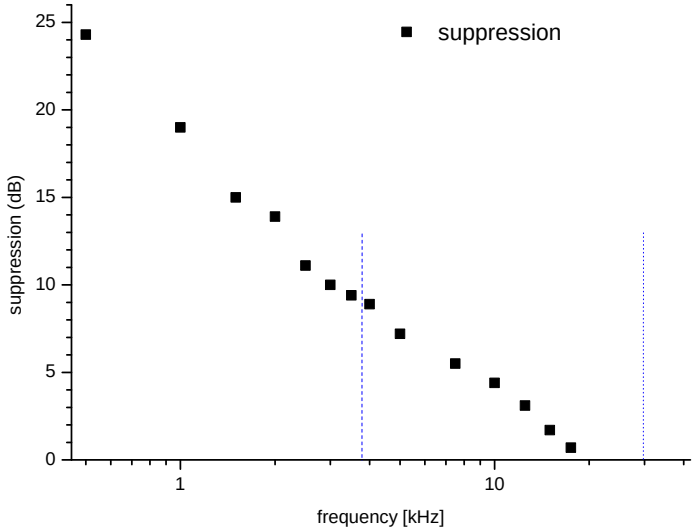

Figure 5.13: Suppression of noise by the PID controller at different frequencies. The blue dotted line at $3.8kHz$ indicates the trapping frequency and the second one the next higher order. The suppression for frequencies lower than $3.8kHz$ is good, for higher frequency the damping could be better. If this is a problem for the lifetime of the trapped atoms one would switch to an analog controller which we have not done yet but kept the advantage of the digital PID. The measurement was performed by modulating the corresponding frequency onto the laser current at a modulation amplitude of 5%. The controller parameters had been: p=0.05, i=0.5, d=0.

error and all previous. The D-fraction is linearly dependent on the difference between the error and the previous error. The corresponding proportionality factors have to be set to get a large bandwidth as well as no induced oscillation. Before the calculated value is set to the output it is feed through a look up table which linearizes the feedback loop which is important since the AOM and the variable attenuator do not have a linear response over the whole dynamical range.
A special feature of our implementation is the possibility of switching from open loop to closed loop control within one cycle. The integrator always carries the correct value for continuing controlling. This becomes interesting for fast jumps from a low to a high set point where closed loop control would be to0 slow. Another nice feature is the capability to stabilize one variable on different inputs which allows for a large dynamical range. The switching between the different inputs proceeds within one cycle and without a jump in the controlled variable.
For the stabilization of the microtrap power we recorded the suppression of noise which we can achieve with the digital controller. Figure 5.13 shows the dependency on the frequency. Unfortunately the suppression for frequencies on the

order of the radial trapping frequencies is not very large. So for high trapping frequencies we expect losses due to heating if we have large noise on the laser power. However, if we lower the power and enter the regime with trapping frequencies around $1kHz$ we should be able to suppress noise that could cause heating and loss inside the microtrap.

Chapter 6

Preparation of a highly degenerate Fermi Gas in the Microtrap

For experiments with a finite number of fermions in a potential, we have to reduce the probability of unoccupied states in the trapping potential, since the shell structure in a finite system of Fermions gets modified by the absence of an interacting particle. We achieve a high occupation probability of the lowest levels in the potential by the preparation of a highly degenerate Fermi in our microtrap. We will increase the degeneracy of an atomic ensemble by applying the microtrap to our shallow crossed-beam trap as described in detail in chapter 3.1. Before any atoms can be transfered, one needs to find a way of spatially superimposing both traps inside the vacuum chamber. Thus, in the first section of this chapter, we present our developed scheme for the superposition of the microtrap with the crossed-beam trap. To transfer the atoms fast and efficient, while staying in thermal equilibrium, we discuss the optimization of the transfer process. The first characterization of the microtrap will be given by the measurement of the lifetime of trapped atoms. The loss of atoms should be kept small and its rate has to be determined, since it has to be considered during the evaluation of future experiments. Additionally, we will focus on the measurement of the trap frequencies. By that, we can determine the harmonic part of our trapping potential from which we can calculate characteristic parameters such as the Fermi temperature of a trapped ensemble. Furthermore, the aspect ratio of the frequencies in axial and radial direction give rise to the actual geometry of the trap. After we have successfully transfered atoms to the microtrap and determined its properties we finish the work of this thesis by giving an estimation of the degeneracy of the Fermi Gas in our microtrap .

6.1 Superposition of the traps and atom transfer

To be able to transfer any atoms from the crossed-beam optical dipole trap into the microtrap for preparing a highly degenerate Fermi Gas, we first have to spatially superimpose both traps. In principle we have to align the beams of both traps such that the focal position of the microtrap beam coincides with the crossing of the crossed-beam trap. However, inside the vacuum chamber, we do not have the possibility to probe the position directly. This is why we have to take a trapped atomic ensemble as an indicator for the position of the crossed-beam trap in wich we can transfer atoms from the MOT. Although we could reach a trap depth of $1mK$ with the microtrap, transferring a significant amount of atoms from the MOT into the microtrap does not work, since the phase space density of the MOT integrated over the volume and the momentum space of the microtrap results in a very small number of atom. If one does not know the expected position of the image of the atoms on the CCD, the small imaging signal of the atoms cannot be distinguished from noise on the CCD. Hence, we have to find a different indirect method to determine the position of the microtrap beam. Instead of far red detuned trapping light, we can use light, resonant to the imaging transition of the atom, which should effect the atoms in the MOT along the course of the resonant beam.
If one finds a possibility to determine the position of both traps, the alignment process will still be challenging, since the extend of the atomic cloud in the crossed-beam trap is roughly $10 \times 10 \times 100\,\mu m$ and the waist of the spot of the microtrap and its Rayleigh length are even smaller ($w_0 = 3.7\mu m$, $z_R = 40\mu m$). In the following we will present our first attempt for the superposition of both traps and discuss the arising difficulties. Subsequently, we will present an improved scheme with which we were able to transfer atoms from the crossed-beam trap to the microtrap.

6.1.1 First attempt to superimpose the traps

In our first attempt, we particularly payed regard to set up the correct vertical position of the focal spot of the microtrap, since initially the coincidence of the focal spot with the position of the atoms in the crossed-beam trap seemed to be essential for the transfer. To determine the vertical position of the focal spot, we prepared a dilute gas of atoms in a Magneto Optical Trap with weak quadrupole field, large detuning and low power of the cooler- and repumper beams. With the a CCD camera we observed the fluorescence light. By applying a beam to the MOT, $60\,Mhz$ red detuned to the cooling transition, which came from the same fiber as the microtrap beam, we detect an increased photon scattering rate along the beam. If this effect resulted from an increased scattering rate of the atoms along the beam due to an induced light shift, or from the increased density of the atoms along the

beam due to near resonance dipole trapping, was not further analysed. The important point for the alignment process is that the shape of the beam became visible (see figure 6.1). Hence, we were able to adjust the beam, so that the focal position coincided with the vertical position of the crossed-beam trap. By knowing

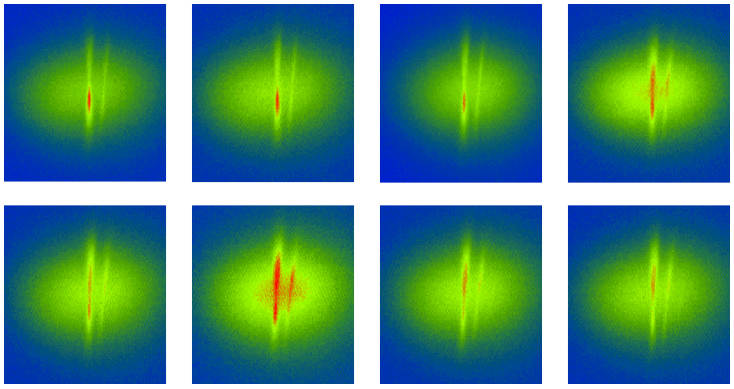

Figure 6.1: Fluorescence images of a dilute gas in a MOT to which a $60Mhz$ red detuned beam, originating from the microtrap fiber, is applied. The different images are taken to determine the vertical position of the focal spot of the microtrap beam. The dilute gas in the MOT is realized by a weak quadrupole field, large detuning and low cooler and repumper power. We observed an increased scattering rate along the beam of the microtrap. Thus, the shape of the beam became visible. Starting from the upper image on the left side, followed by the next image on the right, one can see how the position of the focal spot can be moved through the dilute gas in the MOT. Next to the strong fluorescing atoms along the resonant beam a second weaker beam is visible. This arises due to technical reasons. To transmit sufficient probe light through the dichroitic mirror (see figure 5.4) into the MOT, we need a large beam power, since the mirror is reflection coated for $671\,nm$ light. After passing the upper surface of the mirror substrate, most of the light is reflected by the reflexion coated second surface. The upper surface partly retro-reflects the beam again. The transmitted light of this retro reflex has an offset due to the angle of $45°$ of the mirror to the beam axis and is also focused into the vacuum chamber by the aspheric lens, which becomes visible in the fluorescence image by the second beam.

the difference in the axial position of the focal points of the $671\,nm$ and $1070\,nm$ beam, which we have measured for exactly the used microtrap configuration in the external test setup, we could adjust the position of the $1070\,nm$ beam to the vertical position of the crossed-beam trap. Afterwards we tried to observe an influence of the microtrap potential to a cold ensemble in the crossed-beam trap ($\omega_r \approx 2\pi \times 500\,Hz$). If the axial trap frequency of the microtrap beam was on the order of the radial trap frequency of the crossed-beam trap, we would expect that

the atoms are attracted by the microtrap potential which should become visible in the rise of density at the microtrap position and in a decrease of density in the shallow crossed-beam trap. Additionally, we set the magnetic field to $760\,G$ to achieve a large scattering rate with a scattering length of $a = 4000\,a_0$. For overlapping both traps in the horizontal plain, we planned to move the crossed-beam trap over an area constrained by the size of the MOT, with the hope to coincide with the microtrap beam. However, at this time we only had imaging available in the $-45°H$ axis which allowed us to determine the vertical position of the microtrap and the crossed-beam trap, but the horizontal position of the traps could only be determined to a line parallel to the $-45°H$ axis. Additionally, we did not know in which direction we moved the crossed-beam trap, when we changed the angle of its incoming beam which also effects the retro-reflected beam. This made scanning over an area of the Mot for finding the microtrap position almost impossible.

6.1.2 Improved scheme for the superposition of the traps

After we had tried to align both traps by estimating their horizontal position by only using one CCD camera, it was soon clear that we had to develop a more deterministic method for superimposing both traps. We decided to determine exactly the position of the crossed-beam trap and the microtrap in 3D, which should allow to align both traps such that the crossing of the crossed-beam trap coincides with the spot of the microtrap. To determine the position in 3D, we added an additional imaging system to an independent axis, which was already planned some time ago. By the introduction of the new imaging system, we were able to define a Cartesian coordinate system (figure 6.2) matching to our setup. Now, this allows us to allocate coordinates to any point, which is observed by 2 cameras in different axis. We defined the origin of the coordinate system by the center of the atomic cloud in a strongly confined MOT which we also have shortly before the transfer of the atoms from the MOT to the crossed-beam trap. This is realized by ramping up the quadrupole field by increasing the current in the Feshbach coils and by sweeping the detuning of the cooler and repumper beam closer to resonance. As a next step, we determined the position of the crossed-beam trap after we had optimized the atom transfer from the MOT. To pin down the position of the microtrap, we had to switch back to $671\,nm$ light and detect the influence of the resonant beam on a atomic cloud in a dilute MOT from which we could deduce the horizontal position of the beam. In principle one could observe the fluorescence light of the atoms along a slightly red detuned beam, targeting the MOT as described in section 6.1.1. However, this would only have been possible with one of our cameras, the guppy (figure 6.2). The second camera, the stingray, is located on the MOT axis, where MOT light is transmitted on the CCD chip as

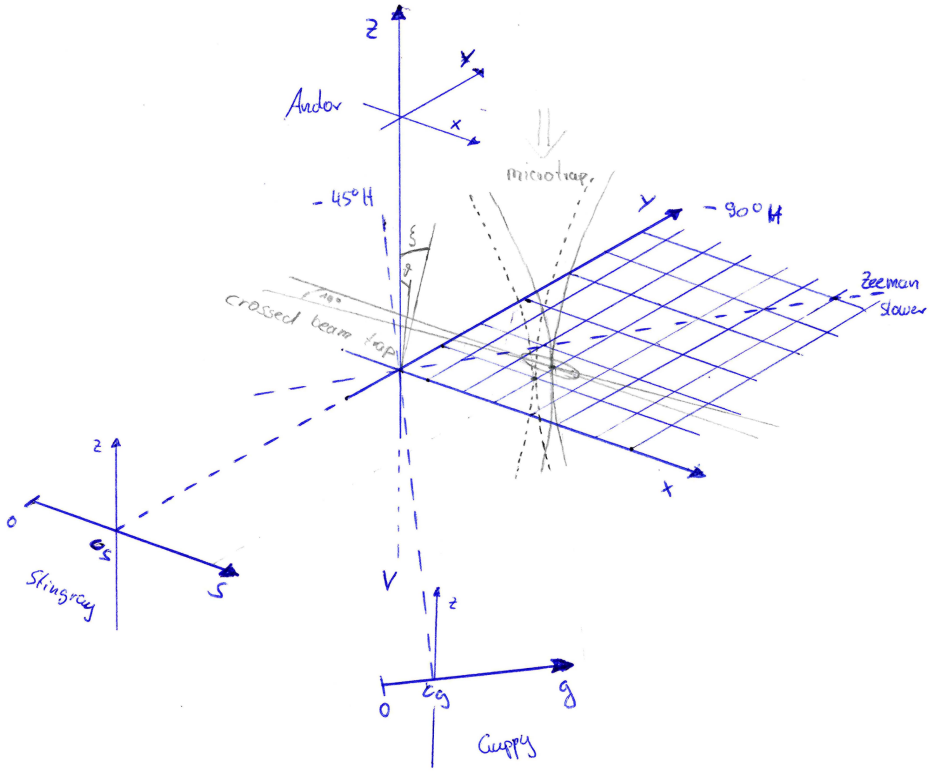

Figure 6.2: Definition of our Cartesian coordinate system. The x-axis is given by the axis of the crossed-beam optical dipole trap and possesses an angle of $45°$ to the Zeeman slower axis. The axis of the Stingray camera ($-90°H$) is perpendicular to the x-axis, the Guppy axis ($-45°H$) is located at $-45°$. The geometric center is defined by the position of a MOT that is strongly confined by a quadrupole field which is created by the Feshbach coils. The Cartesian coordinates of the atoms can be found by triangulation knowing its position on the cameras: $x = s - z_s$, $y = \sqrt{2}(g - z_g) - (s - z_s)$, whereas s is the position on the Stingray, g the position of the Guppy, and z_s and z_g the corresponding zero positions.

long as the MOT is switched on. As for fluorescence imaging we need exposure times of several $10\,ms$, the Stingray CCD would be completely saturated with MOT light within that time. Thus, we have to switch off the MOT light, before we can take images. We exactly did this and took absorption images instantly after the MOT was switched off. Therefore we only need exposure times of $10\mu\,s$ which is short enough that the spacial position of the atoms in the MOT has not significantly changed. Coincidently with the imaging light pulse, we flashed a $671nm$ beam, again coming from the microtrap fiber and directly on resonance

to the imaging transition, onto the dilute atomic cloud. By that, we saturated the transition of the atoms along the $671nm$ beam which could be observed in a decrease in optical density. So we could determine the horizontal position of the $671nm$ beam which is identical to the $1070nm$, preconditioned that the incident $671nm$ beam is on the symmetry axis of the aspheric lens which we ensured by a precise adjustment. A comparison of the position of the crossed-beam and the microtrap position yielded a discrepancy of $500\mu m$! This revealed, that the position of the passively mounted asphere strongly deviated from the position of the Feshbach coils, since they define the position of the MOT before transfer and subsequently the position of the crossed-beam trap. The simplest solution was to manually displace the mount of the aspheric lens until the $671nm$ beam coincided with the position of the crossed-beam trap.

6.1.3 Successful transfer of atoms to the microtrap

After we had been able to determine the position of both traps and after we had adjusted the focal point of the microtrap to the position of the crossing of the crossed-beam trap, we had to transfer atoms from the crossed-beam trap to the microtrap. For the transfer of atoms it is crucial to have a large elastic scattering rate such that the atoms can scatter to the low lying states of the deep microtrap potential. Therefore we set the magnetic field to $760G$ where the scattering length is large and positive ($a = 4000a_0$). Additionally, we selected this value since we are not limited by Pauli blocking when we enter the degenerate regime, because bosonic molecules, formed by 3-body recombination, dominate the ensemble when the thermal energy is lower than the binding energy ($E_B = \hbar^2/ma^2 = k_B \times 2.3\mu K$) of the molecules.
Originally we planned to adjust the microtrap beam that the horizontal position as well as the vertical position of the focal point coincides with the center of the atomic cloud in the crossed-beam trap. Assuming correct adjustment, if the axial trap frequencies of the microtrap is comparable to the radial trap frequency of the crossed-beam trap one expects an increase in density at the position of the microtrap and an decrease in density in the shallow crossed-beam trap. However, we had been lucky not to adjust the correct vertical position of the focal point as intended, which we simply had forgotten at the late hour that day. Thinking more precisely about the scheme, passively overlapping a beam of $3\mu m$ focal waist with an atomic cloud of $10\mu m$ size is rather complicated when the position of the beam can only be determined up to an uncertainty of $30\mu m$. The situation is illustrated in figure 6.2 where the deviation of the microtrap position is indicated by the dashed contour. However, if one adjusts the working distance $500\mu m$ vertically apart from the atomic cloud, the beam with $NA = 0.13$ has a waist of $70\mu m$ at the position of the atomic cloud. If the horizontal position

of the beam was correctly adjusted to $\pm 30\,\mu m$, this implies that the beam definitely coincides with the atomic cloud. The disadvantage is the decreased axial trap frequency of the microtrap due to the large waist. To effect the density of the atomic cloud, which is used as an indicator for the presence of the microtrap , the gradient of the microtrap potential must be large enough to remove atoms of the potential of the crossed-beam trap given by its radial trap frequency and its trap depth ($\omega_{r,s} = 2\pi \times 450Hz$, $P_{beam} = 110\,mW (U_{PDg} = 1\,V)$). Thus for a waist of $70\mu m$ we definitely needed high power to achieve a sufficient gradient into the vertical direction, which is why we slowly increased the power. We detected the first influence on the atomic cloud at $400mW$ beam power, while the beam was constantly switched on. Then at the maximum power which we could safely couple into our microtrap fiber ($600mW$), the gradient was strong enough that the potential of the crossed-beam could not trap atoms anymore, which lead to the observed loss of all atoms. Subsequently we gradually approached the focal spot to the cloud while lowering the beam power. At the same time we optimised the loss of atoms by moving the horizontal position of the microtrap beam. At some lower power level, we observed the first atoms trapped $\approx 300\mu m$ apart from the cloud of the crossed-beam trap. By further adjustment we completely superimposed the microtrap with the crossed-beam trap (Figure 6.3).

6.1.4 Optimizing the atom transfer for preparing a highly degenerate Fermi gas

The aim is to prepare a highly degenerate Fermi Gas, with which we can perform future experiments. For experiments with a small atom number it will be crucial that no holes - unoccupied states whose energy are lower than the energy of another occupied state - exist in the lowest states of the microtrap potential. Thus, we want to keep the atoms in the microtrap in thermal equilibrium with the crossed-beam trap such that during evaporative cooling of the reservoir in the crossed-beam trap, atoms can be scattered to the lowest states of the microtrap. Additionally, the rate of scattered photons, which is proportional to the power of the trapping beam, should be kept small because photon scattering leads to heating of the ensemble. Therefore, several parameters, such as the trap depth of both traps and the scattering length at certain stages of the atom transfer have to be set. For an optimum transfer of atoms and for thermalization, we keep the microtrap beam on, while we evaporate the atoms in the crossed-beam trap at large positive scattering length ($a \approx 4000 a_0$ at $760\,G$), to achieve fast and efficient evaporative cooling. Yet, we set the power of the beam to $P_{mt} = 10mW$ to loose less atoms by photon-scattering which we analysed by lifetime measurements discussed in

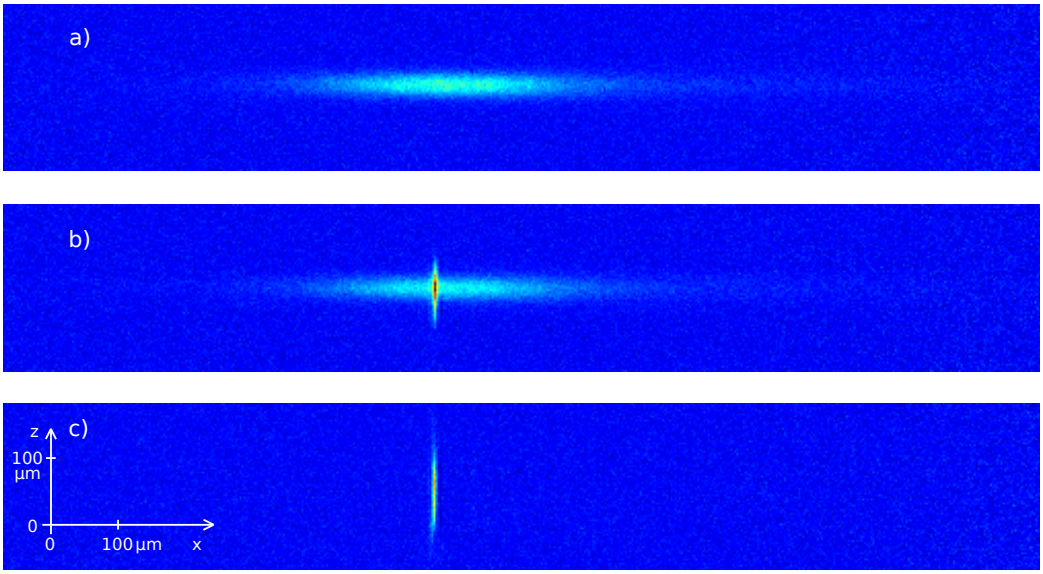

Figure 6.3: Illustration of the transfer of atoms into the microtrap. The in situ images, taken by the Stingray CCD camera, show the optical density of the atomic cloud for different trap configurations. Picture a) shows a large cloud in the crossed-beam trap with the microtrap switched off. The optical density in the wings of the cloud arises from atoms trapped in the single beams of the crossed-beam trap. Picture b) shows the combined trap of crossed-beam trap and microtrap. One can nicely see the rise in density inside the microtrap. In picture c) the shallow trap is switched off with only atoms remaining in the microtrap. The large aspect ration of the trap becomes clearly visible.

the following section. However, for measurements with larger trap depth, we set the corresponding beam power already during evaporation. The beam power is calibrated to the voltage of the photodiode which belongs to the feedback loop for the power stabilization (section 5.3): $P[mW] = 10.75 \times U_{PDmt}[V] \pm 15\%$ (date: 27.04.2009). The large error is a systematic error. We only know the power of the beam inside the vacuum chamber with a relative uncertainty of 15%, since we do not exactly know which constant fraction of the $1070\,nm$ microtrap beam is reflected by the linear polarizer film. However, the voltage on the photodiode can be controlled with a precession on the order of 10^{-3}.
If we want to realize a non interacting Fermi Gas, we have to sweep to lower magnetic field before molecule formation sets in at about $2\mu K$. Therefore we ramp the field to $B = 300G$, where we continue evaporative cooling at a maximum negative scattering length of $a = -300a_0$ until we have reached a trap depth of $2\mu K$ ($\omega_{r,s} = 2\pi \times 360Hz, \omega_a = 2\pi \times 33Hz, P_{beam} = 68mW (U_{PDg} = 0.5V)$).
Instead of switching off the shallow crossed-beam trap, we linearly ramp down the

trap depth to zero within $100ms$, which is slow in comparison with the trap frequencies. By this adiabatic release of the particles of the shallow trap, we remove the hottest particles near the Fermi edge while they can still scatter with atoms of the Fermi sea. However, the thermalization will stop during the release, since the probability to scatter with the residual atoms will drop to zero because of the large expansion of the atomic wavefunction and the subsequent reduced spatial overlap. To remove the particles of the inhomogeneous domain of the Gaussian shaped microtrap potential, we first ramp to the zero crossing of the scattering length at $B = 530G$ to switch off the attractive interaction, which would lower the level spacing. We spill the atoms by slowly applying a magnetic field gradient created by the MOT coils as described in 3.2, which afterwards is slowly turned off again. For studying the cold ensemble in the microtrap the desired scattering length is set by ramping the magnetic field to the corresponding value. In figure 6.3 and 6.4 absorption images of different stages of the transfer are selected. Picture a) shows the crossed-beam trap without the microtrap, at a trap depth were forced evaporative cooling is finished. Picture b) captures the same situation with the microtrap switched on. It nicely gives an expression of the different sizes of the ensembles in both traps. Picture c) illustrates the microtrap after the final step of the transfer. By the previous optimization of the mentioned parameters during

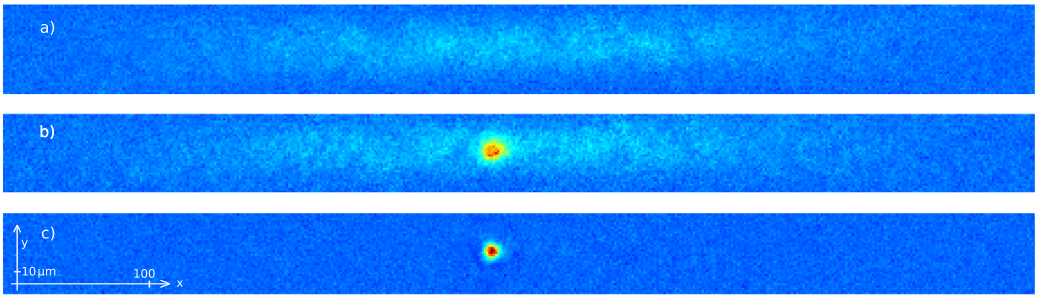

Figure 6.4: Optical density of the atomic cloud; (a) only in the crossed-beam trap, (b) in the combined trap and (c) only the microtrap. The pictures are taken with the Andor CCD camera with $60\mu s$ time of flight to reduce the optical density of the microtrap since the density is integrated over the long axial axis. Additionally the resolution of the Andor imaging system is to low to resolve the in situ cloud without aberration.

the atom transfer, we successfully created a degenerate Fermi Gas in the microtrap. But as described in chapter 2.2.1, it is hard to determine the temperature for very small $T/T_F \ll 0.5$ from the density distribution of a Fermi gas. However, we can still give an estimation of the degeneracy by knowing the Fermi energy of an ensemble in the microtrap, which we will be done in section 6.4. To calculate the Fermi energy, we first have to measure the trap frequencies of the microtrap

which is content of section 6.3.

6.2 Lifetime measurement

In the previous section we achieved the transfer of atoms to the microtrap. With a trapped ensemble in the microtrap, we are now able to characterize the trap. Before we will determine the trap frequencies in the following section we first concentrate on the lifetime of the ensemble in the microtrap. A large lifetime is desired, since we want to be able to study loss processes on long time scales arising from atomic interaction. To separate the "interesting physics" from the loss caused by the trap, we determine the lifetime of a non interacting Fermi gas in the microtrap.
For the measurement of the lifetime and the trap frequency, we follow the preparation scheme presented in the previous section. Thereby it is essential to keep the magnetic field at $530G$ where the scattering length is approximately zero, to realize a non interacting Fermi gas, since a large scattering rate would increase 2- or 3-body collisions which would distort the lifetime measurement and would damp the exited oscillation for the measurement of the trap frequency. To deduce the lifetime we determine the particle number at constant trap depth after various hold-times in the microtrap. Plot 6.5 shows the measured lifetime for 3 different beam power. One sees that the particle number nicely follows an exponential decay from which we can deduce that we are limited by 1-body losses. Since the measured lifetime scales linearly with the power, the dominant process seems to be photon scattering of trapping light (2.28) which causes the atoms to escape of the trap. We can give an estimation for the time scale of this process by calculation the photon scattering rate at a beam power of $10.5mW$ ($U_0 = k_b \times 19\mu K$). We get $\gamma = 0.5s^{-1}$. After scattering a photon the atom gets a recoil energy of $E_r = k_b \times 1.4\mu K$ which leads to heating of the ensemble. Considering only a single atom, it has to scatter 14 photons to escape the trap. This would be after $30s$ which is comparable to the lifetime. Another source of losses can be noise on the power of the microtrap beam which is on the order of the trap frequencies and leads to heating of the ensemble (see chapter 5.3). But as the timescale for the photon-scattering is comparable with the measured lifetime, we suppose that the contribution of the noise on the power of the beam is rather small.
At all, the lifetime we can achieve, is sufficiently long. For power lower than $10mW$, where most experiments will take place, we will have more than $25s$ to perform experiments.

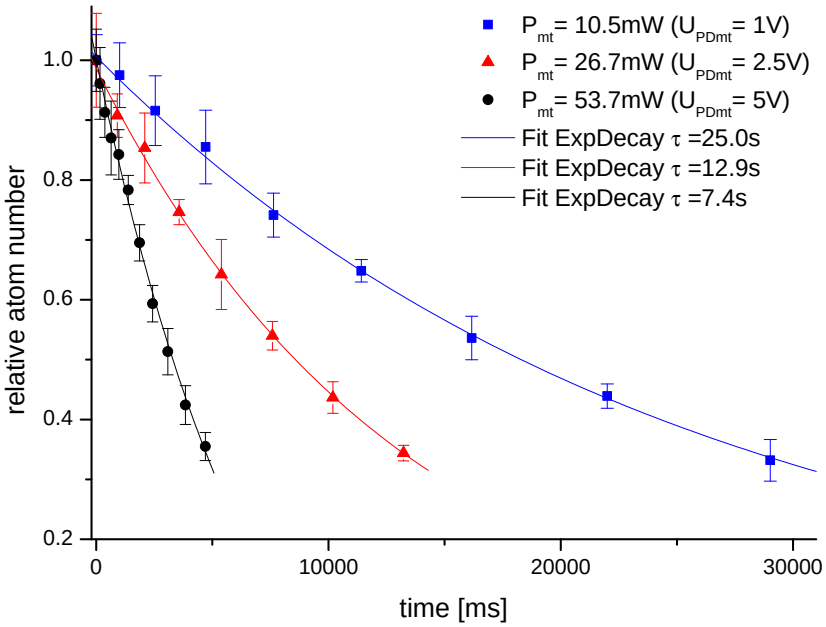

Figure 6.5: Lifetime measurement of a $|1\rangle$-$|2\rangle$ spin mixture at $a \approx 0$ for different beam power of the microtrap. The initial particle number in $|1\rangle$ is ≈ 4500. We plot a relative scale for a better comparison of the lifetime. The well fitting exponential decay shows a 1-body loss process. The lifetime is linearly dependent on the beam power from which we deduce the dominant process to be photon scattering of trapping light.

6.3 Determination of the trap frequencies

We continue the characterization of the microtrap by measuring the trap frequencies. From this measurement we will be able to conclude on the geometry of the microtrap. Additionally we want to determine these parameters to calculate the Fermi temperature of a number of fermions inside the microtrap. To measure the trap frequencies, we have to excite an collective oscillation mode of the atoms inside the microtrap. One possibility of excitation is the dipole-oscillation. Thereby, the center of mass of the trapped cloud oscillates with the trap frequency inside the potential. Another possible mode of excitation is the compression mode. In this mode the cloud is compressed an decompressed with twice the trap frequency. Since the axial and radial frequency is expected to differ by a factor of 15, the time scale for the excitation differs also by one order of magnitude. In the following we will present different methods of how we excite these modes and measure its frequencies to conclude on the trap frequencies. As already mentioned, we perform the measurement of the trap frequencies at $a \approx 0$ to reduce the damping of

the oscillation caused by the interaction of the atoms.

6.3.1 Axial trap frequency

The extent of the cloud in axial direction is comparatively large as one can see in figure 6.3. So if we were able to excite a dipole-oscillation, where the center of mass oscillates with the axial trap frequency, we should be able to observe this oscillation by taking in situ images and recording the center position. The idea is slowly moving the cloud away from its zero position in axial direction. An instant release should causes the atoms to oscillate in the dipole mode with trap frequency ω_a of the microtrap. The excursion from the center position of the microtrap is done by slowly ramping on a magnetic field gradient. The minimum of the combined potential is displaced from the center of the pure optical potential. However, we cannot apply the gradient by the MOT coils, since their inductance is to large. The time constant for their switch off is $30ms$, which is enough that the atoms can adiabatically follow the change in potential. Subsequently, no oscillation will be observed. Therefore, we apply an additional current to one of our Feshbach coils to create the gradient, which can be switched off within shorter than $1ms$ due to their small inductance. The set gradient depends on the trap depth for which the measurement is performed ($\partial_z B_z = 3.4G/cm$ $(I_{add} = 6A$) for $P_{mt} = 32mW$ $(U_{PDmt} = 3V)$ and $\partial_z B_z = 0.3G/cm$ $(I_{add} = 0.5A$) for $P_{mt} = 4mW$ $(U_{PDmt} = 0.4V)$). After switching off, the center of the cloud undergoes a damped oscillation as one can explicitly see in figure 6.6. We perform this measurement for different power of the microtrap to deduce the dependency of the trap frequency on the trap depth. If we approximate the potential harmonically, the relation of $\omega \propto \sqrt{U_0}/w_0^2$ is given according to (2.32). The fit of a square-root on the measurement represents the data quite well (figure 6.7). This shows that the harmonic contribution of the potential scales as expected with the beam power, from which we can deduce that the trap geometry does not change while varying the power.

6.3.2 Radial trap frequency

For exiting the radial dipole oscillation we would have to move the center of mass of the atomic cloud in radial direction and release it within a time faster than the radial oscillation period. Since we are working in a large offset field we cannot excite the atoms in the direction perpendicular to the spin alignment by applying a magnetic field gradient in radial direction. This is why we have to excite the compression mode in radial direction. We do this by switching of the trapping potential for $10\mu s$. The excitation of this mode can be understood as follows: Particles in the potential minimum realize almost no effect of the switch of the

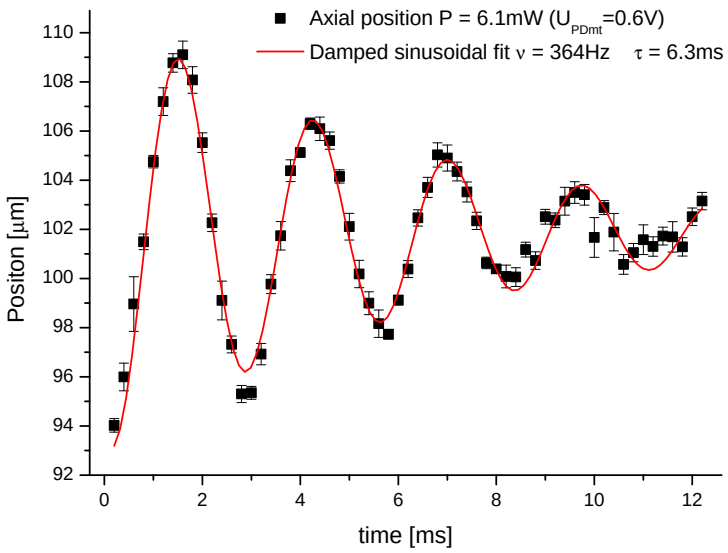

Figure 6.6: Axial dipole oscillation. The mode is excited by slowly moving the cloud apart from the center of the harmonic trap by the application of a magnetic field gradient $\partial_z B_z = 1.4G/cm$ ($I_{add} = 2.5A$). After the sudden release off the combined potential, the cloud oscillates with the axial trap frequency of the microtrap.

potential. However, particles at both turning points of their excursion experience a kick when the potential is switched on after $10\mu s$. As a consequence the cloud starts radially to compress and decompress with twice the radial trap frequency. We can determine this frequency by measuring the momentum distribution for different hold-times of the atoms in the potential by imaging the expanded cloud after a time of flight of $200\mu s$. The measured data is shown in figure 6.8. We observe that the oscillation is strongly damped after more than one periode. This could be due to weak non-harmonic contributions of the potential which lead to coupling between the different principal axis of the oscillator. However, the measurement of the radial frequency for different trap depth (figure 6.9) exhibits again a square root dependency which implies that the trap geometry in radial direction keeps constant while the power of the microtrap beam is changed.

6.3.3 Conclusion on the profile of the microtrap beam

From the measurement of the axial and radial trap frequency we concluded that the geometry of the trap does not change while changing the beam power of the microtrap. We are interested how the actual profile looks like and compare it with the results of the test measurement of section 5.2.1. If we assume a per-

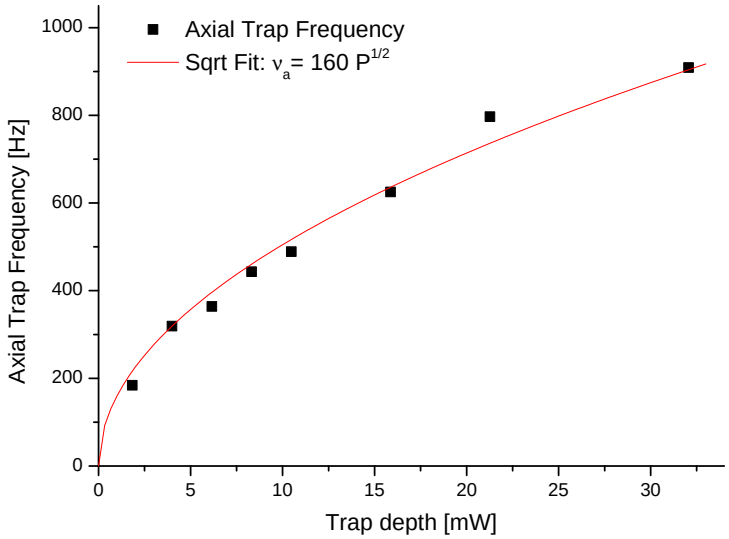

Figure 6.7: Measurement of the axial trap frequency for different trap depth. The data exhibit a square-root dependency on the beam power. Hence, we can assume the that trap geometry of the trapping potential in axial direction does not change while varying the power.

fect Gaussian beam for the microtrap beam, we could determine its focal waist to $w_0 = 4.3\mu m$ from the radial trap frequency. The same calculation for the axial trap frequency would give a focal waist of $w_0 = 5.0\mu m$. Here clearly a discrepancy becomes visible. The aspect ration of the frequencies ω_r/ω_a is ≈ 25 instead of the expected 18 for a Gaussian beam with $w_0 = 4.3\mu m$. A smaller value of the measured aspect ratio could be explained by a deviation of the Gaussian beam profile which could be caused by aberrations. However, no beam can be less divergent than this Gaussian beam. Some other reason must be responsible for this large discrepancy. So far, we have not done any further investigation on this. We only can bring up an argument which could explain the situation. If we assume an astigmatism the measured aspect ratio can be realistic. A simulation showed that a focal waist of $w_0 = 3.6\mu m$ and a shift of the foci in perpendicular planes along the beam axis of $50\mu m$ is consistent with the measurement, while the harmonic approximation is still well for the axial direction. The value of the simulated waist would also be comparable with the result from the test measurement, where we determined a waist of $w_0 = 3.7\mu m$.
Although we have compensated the astigmatism introduced by the dichroitic mirror, we still could have some astigmatism, since the microtrap beam is not exactly aligned to the center of the aspheric lens. This is a result of the limited time, in which the microtrap was superimposed with the crossed-beam trap. Here, further examination has to be done. However, if the worse alignment is the reason, the

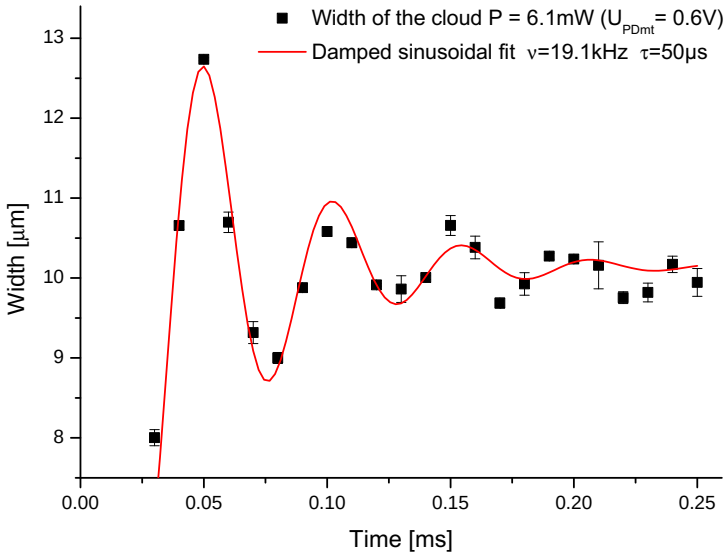

Figure 6.8: Excitation of the radial compression mode by shortly switching of the trapping potential for $10\mu s$. For different hold-times the momentum distribution is observed by the expansion of the cloud after a time of flight of $200\mu s$.

problem will be solvable.

6.4 Estimation of the degeneracy

In the previous sections we described the preparation of a highly degenerate Fermi Gas in the microtrap. By trapping a non interacting Fermi Gas, we were able to determine characteristic parameters of the trap such as the trap frequencies. At last, we want to present an estimation of the achieved degeneracy of the Fermi Gas in the microtrap.
As described in chapter 2.2.1, the temperature for very small $T/T_F \ll 0.5$ is hard to determine from the density distribution of a Fermi gas, especially if the atom number is small. However, we can give an estimation of its degeneracy by the method explained in 3.1. Therefore, we assume thermal equilibrium after evaporation has finalized at $a = -300a_0$. The temperature determination of the atoms in the shallow trap is done without the presence of the microtrap but with the same trap depth as we have at the final stage of evaporation in the combined trap. We measure an absolute temperature of $200nK$ which corresponds to $T/T_{F,s} = 0.27$ ($\omega_{r,s} = 2\pi \times 360Hz, \omega_{a,s} = 2\pi \times 33Hz, N_s = 150000$) in the shallow trap. By knowing the parameters of the microtrap at a beam power of $6.1mW$ ($\omega_{r,mt} = 2\pi \times 9.6\,kHz, \omega_{a,mt} = 2\pi \times 350\,Hz, N_{mt} = 5000$) we can calculate the Fermi temperature and obtain $T/T_{F,mt} = 0.04$! This is an increase of a factor of

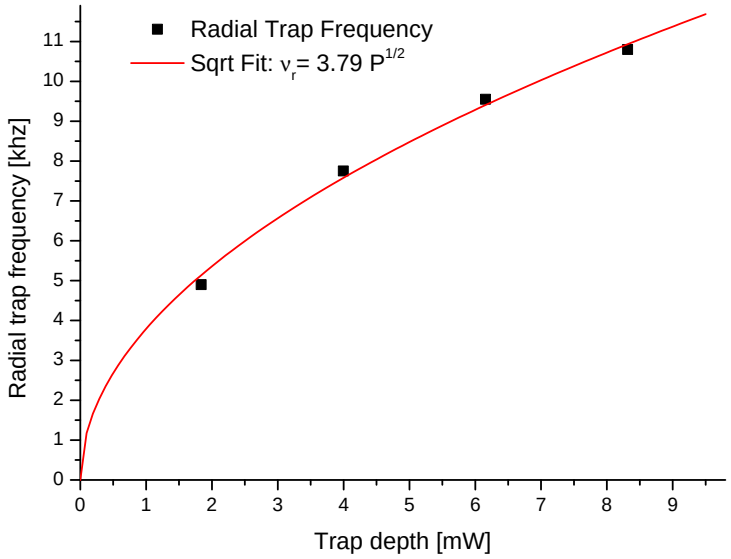

Figure 6.9: Measurement of the radial trap frequency for different trap depth. The data exhibit a square-root dependency on the beam power. Hence, we can assume that the trap geometry of the trapping potential in radial direction does not change while varying the power

6.6 compared to the shallow trap. We think this is a rather good approximation, although a proof for thermalization of atoms in both traps has still to be given. We believe we can even reach lower temperatures, if we form molecules at $760\,G$ and adiabatically separate the dimers into atoms by ramping to a field larger than $900\,G$ [Bar04, Bou04].

Furthermore, we want to give another estimation for the temperature of the Fermi Gas at a scattering length of $900G$. We do this by comparison the properties of our prepared Fermi Gas with the experiment recently performed in the group of John E. Thomas [Du09]. They have measured the inelastic two-body and three-body decay rates for a two-component Fermi Gas around the Feshbach resonance. At high temperature they observed a dominant three-body decay process and at low energy their data also showed a two-body decay process above the resonance. They suggested that this process arises from correlated pairs, which is a many-body process. Pair-atom or pair-pair collisions are possible which should become visible in a two-body decay process. The existence of such pairs at a certain temperature depends on the interaction strength given by $k_F a$. For smaller $k_F a$ they did not observe a two-body decay process. In the following we want to compare the particle loss in our Fermi Gas at $900G$ with the results from John E. Thomas' group. By that we get an idea about the temperature we have achieved in our prepared degenerate Fermi Gas. Hence, we recently measured a loss curve (figure

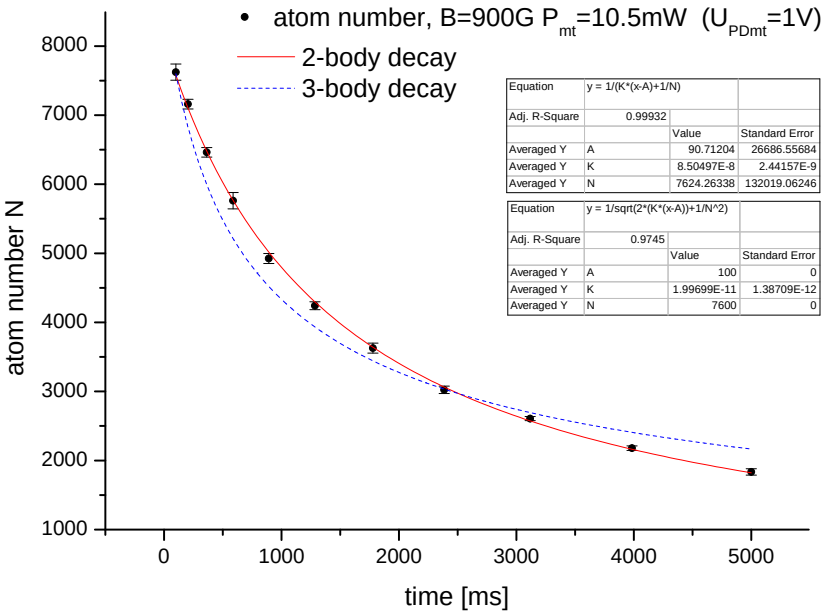

Figure 6.10: Loss in atoms at $B = 900G$ ($k_F a \leq -5$). Recorded is the atom number in $|1\rangle$ of a $|1\rangle$-$|2\rangle$ spin mixture. The measured data can be fitted quite well by a two-body loss, which can arise from two-body collisions of paired atoms. A 3-body loss curve which describes three-body relaxation deviates from the measured data. By comparison with the work done in the group of John E. Thomas [Du09], we can give an upper limit of $T/T_F = 0.14$.

6.10) at $900G$ and fitted a pure two-body decay

$$N = \frac{1}{K_2(t - t_0) + 1/N_0} \tag{6.1}$$

as well as a pure three-body decay, which is the case for three-body relaxation,

$$N = \frac{1}{\sqrt{2K_3(t - t_0) + 1/N_0^2}} \tag{6.2}$$

with the two-body (three-body) loss coefficient K_2 (K_3). One sees that the two-body decay fits well, whereas the three-body decay deviates from the measured data. Due to the limited time we have not been able to do any detailed analysis. For our estimation of temperature we neglect the actual density distribution and we assume the density to be proportional to the particle number all time. Yet, this should not disturb the conclusion of our estimation. If heating leads to a decrease in density, the three-body losses decreases faster than the two-body losses which would result even in an flatter curve of the fitted three-body decay for larger times.

One-body losses are also neglected since the measured one-body decay time of $25s$ is one order of magnitude larger than the time scale for the observed loss process. In the case the observed loss originates from two-body collisions of pairs, we can compare this measurement with the work of John E. Thomas' group. They have not observed 2-body losses for $k_F a \leq -11$ ($B > 860G$) at $E/E_F = 0.7$ (corresponding to $T/T_F = 0.14$ according to [Luo08]). In our case the interaction strength is smaller: $k_F a \leq -5$ ($\omega_{r,mt} = 2\pi \times 11kHz$, $\omega_{a,mt} = 2\pi \times 500Hz$, $N = 5000$, $a = -7860a_0$). This implies that pairs should only exists at lower temperature. If we still see a two-body loss, this gives us the hint that the degeneracy of our Fermi gas should be lower than $T/T_F = 0.14$ of [Du09].
With this estimation we finish the characterization of the trapped Fermi Gas. The future task will be finding a reliable method to determine the temperature of the degenerate Fermi gas in the microtrap.

Chapter 7

Conclusion and Outlook

In this thesis we reported on the realization of a micrometer-sized trap in which we have created a highly degenerate Fermi gas of ^{6}Li atoms. The microtrap is an important milestones on the way towards experiments with a finite number of fermions. Few-fermion systems are quite common in nature, like electrons in the atom or nucleons in the nuclei. Ultracold quantum gases in a microtrap could become a generic system to understand and model various of such systems.
In a two-component spin-mixture the interaction strength can be tuned by means of Feshbach resonances. To tune the scattering length we need large magnetic fields which is the reason why we built coils capable of conducting high currents. Due to limited space around our experimental chamber, this task was quite challenging. However, now we are able to create fields up to $1000\,G$ constantly. We can also enter the regime up to $1500\,G$ for at least $1s$ which is sufficient to perform experiments at this high field region.
As the focus of this thesis is the realization of a highly degenerate Fermi gas in a microtrap, we therefore discussed the used method, the so called "dimple trick". By applying a microtrap to a shallow trap, the phase space density in the microtrap can be increased. To obtain occupation probability of states in the microtrap close to one, high level spacing is required. Since we create the trap by an optical dipole potential of a single focused Gaussian beam, we put effort in achieving a small focal waist. We designed a compact high-resolution assembly and tested its performance. Thereby we used an standard aspheric lens to get an idea of the capability of our design and learn about its properties.
After the implementation to our apparatus, we successfully transfered atoms of our large volume optical dipoltrap into the microtrap. We were able to give a quantitative description of the trap properties by the determination of the lifetime and the trap frequencies. The trap geometry in radial and axial direction stays unchanged by varying the power of the microtrap beam. The reason for the measured large aspect ration is not yet completely understood; hence further

investigation will follow. Finally, we gave some estimation of the degeneracy of the fermions in the microtrap with an upper limit of $T/T_F = 0.14$.
In the future, it would be nice to find a scheme for the determination of the temperature of our ensemble. Also, we are currently working on simulations for a new lens system for the microtrap, with which we could even reach higher trap frequencies and subsequently higher level spacing. If we want to count only few fermions, which will be the case in future work, we will have to set up an imaging system for detecting fluorescence light with high quantum efficiency.
Furthermore, we have ideas for moving atoms from the shallow trap to a region with different magnetic field by means of the microtrap. This would allow us to manipulate the internal states of the atoms in the microtrap by resonant rf, without distorting the ensemble in the shallow trap. By that we could locally bring a third spin component into a two-component mixture and observe the subsequent dynamical processes.
Besides the various possible applications of the microtrap, the main future emphasis is the control of the particle number in the microtrap. For the interpretation of future experiments it is crucial not to have any holes - unoccupied states with energy lower than other occupied states - in the Fermi Gas, since we cannot detect them. Interacting particle change the shell structure of the non-interacting case and hence fluctuations of holes in a sequence of experiments would lead to fluctuations in the detected structure. This is why we have created a highly degenerate Fermi Gas where the probability for having holes in the lowest levels approaches zero. To remove the atoms in the upper level of the microtrap and to control the particle number we have applied a magnetic field gradient to the microtrap as described in this thesis. Figure 7.1 shows the particle number dependent on the

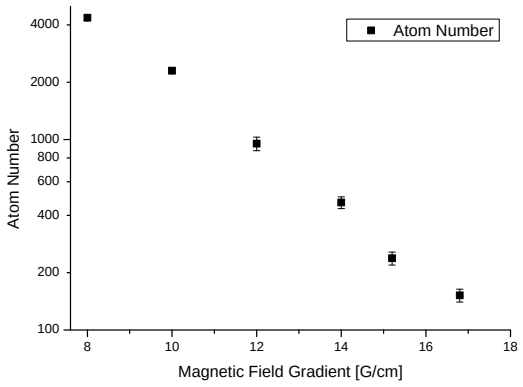

Figure 7.1: Particle number dependent on the gradient with which we spill the atoms from the microtrap. The gradient is applied by our MOT coils to the microtrap with trapping frequencies $\omega_a = 2\pi \times 350\,Hz$ and $\omega_r = 2\pi \times 8.5\,kHz$.

applied gradient. To get an idea, to which extend we so far can control the par-

ticle number by this technique, we observed the number fluctuations for different measurements with constant gradient and mean particle number of 120, without having done any optimization on the spilling process. The observed particle number is illustrated in the histogram of figure 7.2. One can see that the measured

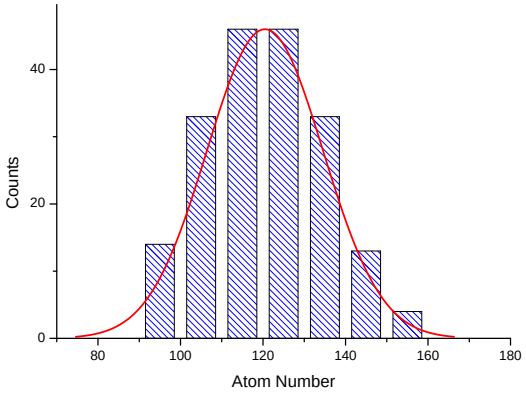

Figure 7.2: Illustration of the current control of the particle number. The Histogram shows the particle number after spilling the residual atoms of the microtrap by applying a magnetic field gradient as described in this, repeated for ≈ 200 measurements. If we have detected N particles in a measurement we added one count to the column which incorporates the number of measurements with particle number $10\,n \leq N < 10\,(n+1) \quad (n \in \mathbb{N})$. The red curve is a normal distribution fitted to the histogram. One sees that the measured particle number is approximately normal distributed with a standard deviation of $\sigma = 14$.

particle number is approximately normal distributed, even for that small particle number. The source of the measured fluctuations is not only the actual variation in particle number, which can occur from tunneling of atoms of the upper level through the potential barrier or from particle excitations during the application of the gradient. Also detection noise, which is not extracted, contributes to the observed fluctuations, which will vanish if we are able to detect single atoms after an expansion time of the atomic cloud by using fluorescence imaging in future. We are confident that we will also reduce the particle fluctuations by increasing the level spacing in a new microtrap design. The long term goal is the control of the atom number on the single particle level.
In conclusion, we are on a good way towards a finite system of fermions. If we achieve control of the quantum states, one of the first possible things to observe, will be the shell structure of non-interacting fermions in the harmonic potential and its change when interaction is turned on. We are confident that in the future we will be able to study interesting physics by the observation of few fermions in the microtrap.

A. Fundamental constants and ^{6}Li level scheme

Symbol	Value	Meaning
$\hbar$	$1.054571628\times10^{-34}$ Js	Planck's constant over 2π
h	6.62606896×10^{-34} Js	Planck's constant
c	2.99792458×10^{8} m/s	Speed of light in vacuum
k_B	1.3806504×10^{-23} JK^{-1}	Boltzmann's constant
a_0	$0.52917720859\times10^{-10}$ m	Bohr's radius
μ_B	927.400915×10^{-26} J/T	Bohr's magneton
m_e	9.10938215×10^{-31} kg	Mass of a electron
m_{Li}	9.98834146×10^{-27} kg	Mass of a ^{6}Li atom
Γ_{Li}	36.898×10^{6} s^{-1}	Natural linewidth of the D_2 line of ^{6}Li
λ_{Li}	670.977338×10^{-9} m	Wavelength of the D_2 line of ^{6}Li in vacuum

Table 1: Constants used in this thesis. The fundamental constants are taken from [NIS], the properties of ^{6}Li can be found in [Geh]. The table is taken from [Wen09] and slightly adapted.

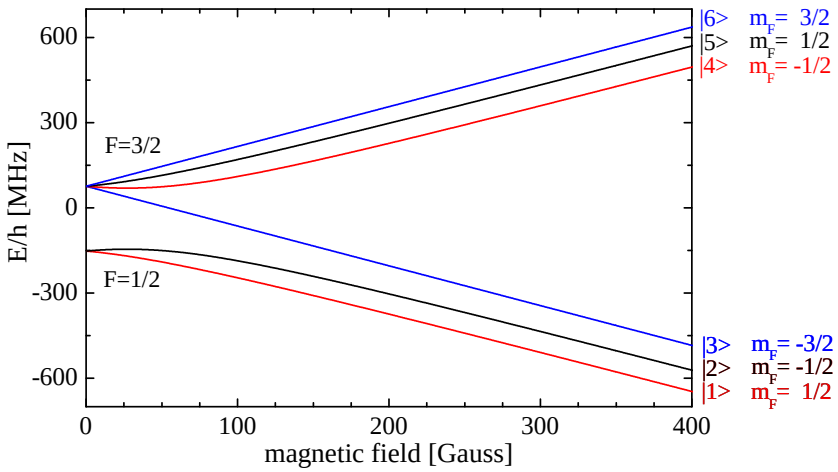

Figure 3: Zeeman hyperfine levels of the ^{6}Li electronic ground state. Plot taken from [Wen09].

B. Procedure of coil manufacture (German)

1. Schritt: Spule wickeln (4 Personen)
Benötigt: Kupferdraht, gereinigte Wickelkörper, Epotec epoxy, Drehbank in Werkstatt.

- Loch in Draht bohren und an Wickelkörper befestigen. Windungssinn auswählen
- Person 1: Drehbank. Person 2: Draht spannen. Person 3: Draht mit Epoxy einschmieren. Person 4: Neueste Drahtwindung mit Plastikstange an Wickelkörper andrücken.
- Nach ca. 17 Windungen Drehbank einrasten. Epoxy mit Heissluftfön direkt in der Drehbank curen bis Windungen fest.
- Nochmals im Backofen weitercuren.
- Spulen zum Abdrehen in Werkstatt geben.

2. Schritt: Spule aufkleben (2 Personen)
Benötigt: abgedrehte Spulen, Spulenkühlkörper, Diamantkleber, Schwefelsäure, Wasserstoffperoxid

- Kleber auftauen
- Ofen auf $60°C$ vorheizen.
- Spule mit gewünschtem Windungssinn auswählen
- Oxidschicht auf Oberfläche von Spulenkühlkörper und Spule reduzieren. Dazu 1% -ige Schwefelsäure nehmen und kurz bevor Spule bzw. Kühlkörper eingelegt wird 3% Wasserstoffperoxid hinzugeben, welches das Kupferoxid reduziert.
- Spule an Kühlkörper anpassen und innen auf der Spule die Kontaktstelle markieren um beim Kleben schnell die korrekte Orientierung zu finden.
- Spulenkühlkörper auf $60°C$ vorheizen
- Kleber auf Spule gleichmaessig mit dem Finger auftragen (mitteldick)
- Kühlkörper mit Kleber 10 min bei $60°C$ heizen
- Backofen auf $140°C$ vorheizen. Thermocouple als Temperaturkontrolle hinzulegen.
- Spulenkühlkörper auf Spulen auflegen, Orientierung für Anschlüsse beachten!! Kühlkörper auf Spule andrücken mit maximal von Hand erzeugtem Druck. Scherkräfte vermeiden. Auf elektrische Leitfähigkeit überprüfen.
- Spule bei $140°C$ 2 Stunden backen.

3.Schritt: Vorbereitungen Anschlüsse löten (1 Person)
Benötigt: Diamatkleber

- Kleber auftauen
- Ofen auf $130°C$ vorheizen.
- Windungen zählen. Ganzzahlig 15 Windungen. Überschüssige Windungen aussen abwickeln und entfernen. Dazu mit Dremel in Kupfer einfräsen und beachten nicht die Klebestelle zwischen Spule und Kühlkörper anzufeilen. Elektrischer Kontakt prüfen.
- Fugen und Löcher des versenkten Rasters mit Diamant-Kleber ausfüllen und bei

$130°C$ backen, damit beim Fräsen keine Späne in die Löcher gelangen können.
- Kontaktstelle für Anschlüsse in der Werkstatt einfräsen lassen. Beachten, dass nicht bis an Kühlkörper gefräst wird.

4. Schritt: Anschlüsse löten (3 Personen)
Benötigt: Anschlüsse, Indium, Flussmittel, Diamantkleber, Heizband, Thermocouple, PID Regler, Kaptonband

- Thermocouple auf Spulenkühlkörper kleben.
- dünne Schicht Diamantkleber auf Aussparung für Anschlüsse am Spulenkühlkörper auftragen.
- Ofen auf $200°C$ heizen (maximale Temperatur) und Anschlüsse hineinlegen
- Spule in Heizband einwickeln und mit Aluminium einpacken. Temperatur auf $140°C$ stabilisieren.
- Anschlüsse auf beiden Seiten mit Indium benetzen und zurück in Ofen bei $200°C$. Kontaktstellen mit Indium benetzen.
- erste (innere) Anschluss aus dem Ofen nehmen und anlöten. Erste Person hält Anschluss, zweite Person lötet und dritte Person kontrolliert ob Anschluss im korrekten Winkel zum Kühlkörper sitzt.
- Zwischenraum zwischen Anschluss und Kühlkörper mit Diamantkleber ausfüllen und bei $140°C$ eine Stunde curen
- Innere Kontaktstelle mit Kaptonband gegen zweiten Anschluss isolieren
- zweiter (äusserer) Anschluss anlöten, Zwischenraum mit Diamantkleber ausfüllen und eine Stunde bei $140°C$ curen.

5. Schritt: (1 Person)
Benötigt: Knetepoxy, Plastik 70, Auspufflack

- Anschlüsse und Kühlwasseranschlüsse mit Knetepoxy fixieren.
- Überschüssiges Indium und Kleber entfernen. Spule in Testhalterung einpassen. Evtl. von Kupferanschlüssen etwas abfeilen.
- Halterungen ankleben
- Innen- und Oberseite von Kühlkörper und Anschlüsse mit Auspufflack schwarz lackieren um Streulicht zu unterdrücken.
- Anschlüsse und blanke Kupferstellen an Spule mit Kapton tape isolieren

C. Electronic Circuits

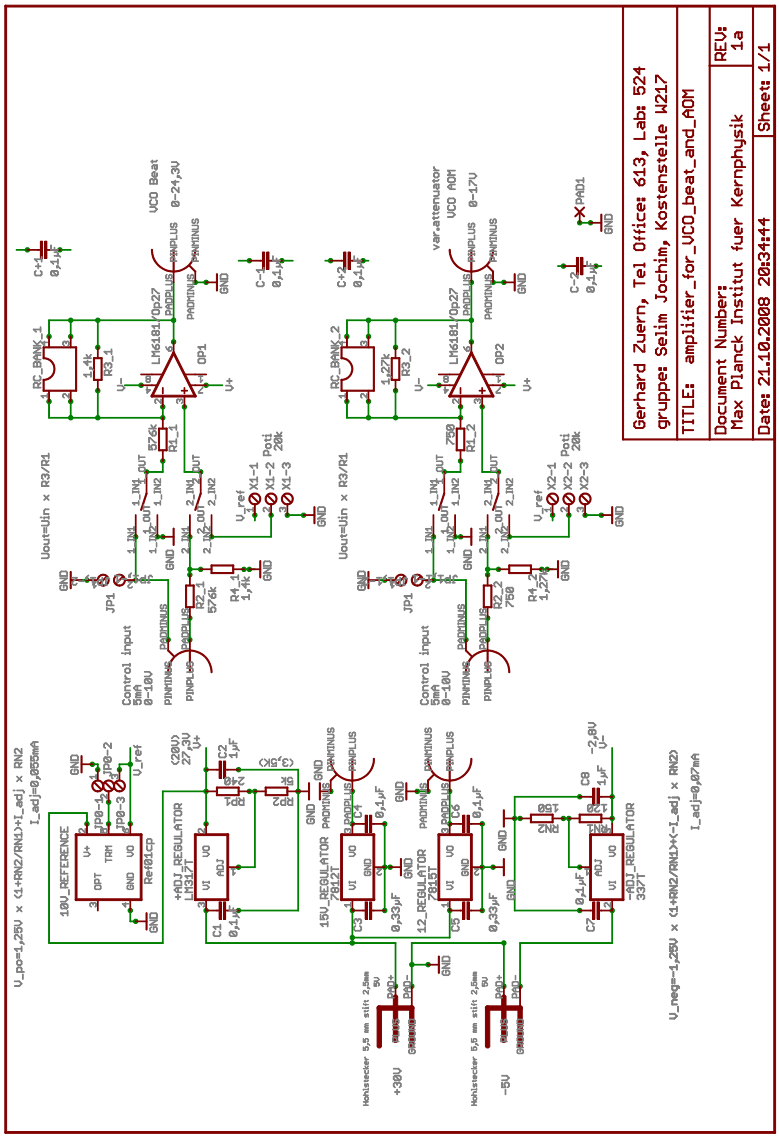

Figure 4: Amplifier for VCO of AOM and Beat lock

Bibliography

[And95] M. H. Anderson, J. R. Ensher, M. R. Matthews, C. E. Wieman, E. A. Cornell, *Observation of Bose-Einstein condensation in a Dilute Atomic Vapor*, Science **269**, 198–201 (Jul 1995).

[Bar04] M. Bartenstein, A. Altmeyer, S. Riedl, S. Jochim, C. Chin, J. H. Denschlag, R. Grimm, *Crossover from a molecular Bose-Einstein condensate to a Degenerate Fermi Gas*, Phys. Rev. Lett. **92**(12), 120401 (Mar 2004).

[Bla01] E. D. Black, *An introduction to Pound-Drever-Hall laser frequency stabilization*, American Journal of Physics, **69**(1), 79–87 (2001).

[Bou04] T. Bourdel, L. Khaykovich, J. Cubizolles, J. Zhang, F. Chevy, M. Teichmann, L. Tarruell, S. J. J. M. F. Kokkelmans, C. Salomon, *Experimental Study of the BEC-BCS Crossover Region in Lithium 6*, Phys. Rev. Lett. **93**(5), 050401 (2004).

[But97] D. A. Butts, D. S. Rokhsar, *Trapped Fermi gases*, Phys. Rev. A **55**(6), 4346–4350 (Jun 1997).

[Chi04] C. Chin, M. Bartenstein, A. Altmeyer, S. Riedl, S. Jochim, J. H. Denschlag, R. Grimm, *Observation of the Pairing Gap in a Strongly Interacting Fermi Gas*, Science **305**(5687), 1128–1130 (2004).

[Chi06] C. Chin, R. Grimm, P. Julienne, E. Tiesinga, *Feshbach resonances in ultracold gases* (2006).

[Dal98] J. Dalibard, *Collisional dynamics of ultra-cold atomic gases* (1998).

[Dav95] K. B. Davis, M. O. Mewes, M. R. Andrews, N. J. van Druten, D. S. Durfee, D. M. Kurn, W. Ketterle, *Bose-Einstein condensation in a gas of sodium atoms*, Phys. Rev. Lett. **75**(22), 3969–3973 (Nov 1995).

[DeM99] B. DeMarco, D. S. Jin, *Onset of Fermi degeneracy in a trapped atomic gas*, Science **285**(5434), 1703–1706 (1999).

[Dir26] P. A. M. Dirac, *On the Theory of Quantum Mechanics*, Proceedings of the Royal Society of London. Series A **112**(762), 661–677 (Oct 1926).

[Du09] X. Du, Y. Zhang, J. E. Thomas, *Inelastic Collisions of a Fermi Gas in the BEC-BCS Crossover* (2009).

[Foo05] C. Foot, *Atomic Physics* (Oxford University Press, 2005), 1st Edn.

[Geh] M. E. Gehm, *Properties of* ^{6}Lithium, *2003: http://www.phy.duke.edu/research/photon/qoptics/techdocs/pdf/PropertiesOfLi.pdf*.

[Gre03] M. Greiner, C. A. Regal, D. S. Jin, *Emergence of a molecular Bose-Einstein condensate from a Fermi gas*, Nature **426**, 537–540 (2003).

[Gri00] R. Grimm, M. Weidemüller, Y. B. Ovchinnikov, *Optical dipole traps for neutral atoms*, Advances in Atomic, Molecular and Optical Physics **42**, 95 (2000).

[Hae75] T. Haensch, A. Schawlow, *Cooling of gases by laser radiation*, Optics Communications **13**(1), 68–69 (Oct 1975).

[Her08] I. V. Hertel, C.-P. Schulz, *Atome, Moleküle und optische Physik 1* (Springer Berlin Heidelberg, 2008), 1st Edn.

[Huc09] J. H. Huckans, J. R. Williams, E. L. Hazlett, R. W. Stites, K. M. O'Hara, *Three-Body Recombination in a Three-State Fermi Gas with Widely Tunable Interactions*, Phys. Rev. Lett. **102**(16), 165302 (Apr 2009).

[Ino98] S. Inouye, M. R. Andrews, J. Stenger, H.-J. Miesner, D. M. Stamper-Kurn, W. Ketterle, *Observation of Feshbach resonances in a Bose-Einstein condensate*, Nature **392**, 151 (1998).

[Joc03a] S. Jochim, M. Bartenstein, A. Altmeyer, G. Hendl, C. Chin, J. H. Denschlag, R. Grimm, *Pure Gas of Optically Trapped Molecules Created from Fermionic Atoms*, Phys. Rev. Lett. **91**(24), 240402 (Dec 2003).

[Joc03b] S. Jochim, M. Bartenstein, A. Altmeyer, G. Hendl, S. Riedl, C. Chin, J. Hecker Denschlag, R. Grimm, *Bose-Einstein condensation of molecules*, Science **302**(5653), 2101–2103 (2003).

[Joc04] S. Jochim, *Bose-Einstein Condensation of Molecules*, Dissertation, Universität Innsbruck (2004).

[Joc09] S. Jochim, *Ultracold Fermi gases: Properties and techniques* (2009), in: M. Weidemueller, C. Zimmermann (Eds.), Cold Atoms and Molecules, 2nd edition.

[Joe08] R. Joerdens, N. Strohmaier, K. Guenter, H. Moritz, T. Esslinger, *A Mott insulator of fermionic atoms in an optical lattice*, Nature **455**(12), 204–207 (Sep 2008).

[Jul92] P. Julienne, A. Smith, K. Burnett, *Theory of Collisions between Laser Cooled Atoms*, Vol. 30 of *Advances In Atomic, Molecular, and Optical Physics*, 141 – 198 (Academic Press, 1992).

[Koh08] M. Kohnen, *Ultracold Fermi Mixtures in an Optical Dipole Trap*, Diploma thesis (2008).

[Lom08] T. Lompe, *An appartus for the production of molecular Bose-Einstein condensates*, Diploma thesis (2008).

[Luo06] L. Luo, B. Clancy, J. Joseph, J. Kinast, A. Turlapov, J. Thomas, *Evaporative cooling of unitary Fermi gas mixtures in optical traps*, New Journal of Physics **8**(9), 213 (2006).

[Luo08] L. Luo, J. E. Thomas, *Thermodynamic Measurements in a Strongly Interacting Fermi Gas* (2008).

[May49] M. G. Mayer, *On Closed Shells in Nuclei. II*, Phys. Rev. **75**(12), 1969–1970 (Jun 1949).

[Met99] H. J. Metcalf, P. van der Straten, *Laser Cooling and Trapping* (Springer-Verlag, New York, 1999).

[NEG] NEG (non evaporable getter coating), *Information available at:*, http://est-div-sm.web.cern.ch/est-div-sm/Project-Getter-home.htm .

[NIS] NIST, *http://physics.nist.gov/cuu/Constants/*.

[O'S09] B. O'Sullivan, T. Busch, *Spontaneous Emission in ultra-cold spin-polarised anisotropic Fermi Seas*, Phys. Rev. A **79**, 033602 (Mar 2009).

[Ott08] T. B. Ottenstein, T. Lompe, M. Kohnen, A. N. Wenz, S. Jochim, *Collisional Stability of a Three-Component Degenerate Fermi Gas*, Phys. Rev. Lett. **101**(20), 203202 (2008).

[Pau25] W. Pauli, *Über den Zusammenhang des Abschlusses der Elektronengruppen im Atom mit der Komplexstruktur der Spektren*, Zeitschrift für Physik **31**(1), 765–783 (Jan 1925).

[Pin97] P. W. H. Pinkse, A. Mosk, M. Weidemüller, M. W. Reynolds, T. W. Hijmans, J. T. M. Walraven, *Adiabatically Changing the Phase-Space Density of a Trapped Bose Gas*, Phys. Rev. Lett. **78**(6), 990–993 (Feb 1997).

[Reg03] C. A. Regal, C. Ticknor, J. L. Bohn, D. S. Jin, *Creation of ultracold molecules from a Fermi gas of atoms*, Nature **424**(6944), 47–50 (2003).

[Sak94] J. J. Sakurai, *Modern Quantum Mechanics* (Addison-Wesley Publishing Company, Inc., 1994), revised edition Edn.

[Sal91] B. E. A. Saleh, M. C. Teich, *Fundamentals of Photonics* (John Wiley and Sons, Inc., 1991).

[Sch99] U. Schunemann, H. Engler, R. Grimm, M. Weidemuller, M. Zielonkowski, *Simple scheme for tunable frequency offset locking of two lasers*, Review of Scientific Instruments **70**(1), 242–243 (1999).

[Sch07] F. Schwabl, *Quantenmechanik* (Springer-Verlag Berlin, 2007), 7th Edn.

[Ser07] F. Serwane, *The setup of a Magneto Optical Trap for the preparation of a mesoscopic degenerate Fermi gas*, Diploma thesis (2007).

[SK98] D. M. Stamper-Kurn, H.-J. Miesner, A. P. Chikkatur, S. Inouye, J. Stenger, W. Ketterle, *Reversible Formation of a Bose-Einstein Condensate*, Phys. Rev. Lett. **81**(11), 2194–2197 (sept 1998).

[Sue49] H. E. Suess, O. Haxel, J. H. D. Jensen, *Modellmässige Deutung der ausgezeichneten Nucleonenzahlen Im Kernbau*, Naturwissenschaften **36**(5), 155 (Mar 1949).

[Wen09] A. N. Wenz, *Few-Body Physics in a Three-Component Fermi Gas*, Diploma thesis (2009).

[Zan99] A. Zannoni, *On the Quantization of the Monoatomic Ideal Gas* (1999).

[Zwi03] M. W. Zwierlein, C. A. Stan, C. H. Schunck, S. M. F. Raupach, S. Gupta, Z. Hadzibabic, W. Ketterle, *Observation of Bose-Einstein Condensation of Molecules*, Phys. Rev. Lett. **91**(25), 250401 (Dec 2003).

[Zwi05] M. W. Zwierlein, J. R. Abo-Shaeer, A. Schirotze, C. H. Schunck, W. Ketterle, *Vortices and superfluidity in a strongly interacting Fermi gas*, Nature **435**, 1047–1051 (2005).

Danksagung

Ich möchte einigen Personen danken, durch derren Hilfe und Unterstützung diese Arbeit überhaupt erst ermöglicht wurde.
Zu aller erst möchte ich Selim danken, der stets Zeit für unsere Anliegen und Fragen hat. Dabei schätze ich seine Motivation, sein fachliches Wissen und seine Gedult, mit der er uns komplizierte sowie einfache Sachverhalte erläutert. Die große Unterstützung, die Selim für seine Studenten aufbringt und auch für mich aufgebracht hat, ist nicht selbsverständlich, weshalb ich sie ausdrücklich erwähnen möchte.
Wir scherzten ab und zu, dass ein Motivationstrainer bei uns nach zwei Wochen frustriert aufgeben würde. In Wirklichkeit ist es gelungen in der Gruppe eine besondere Atmoshpäre zu schaffen, in der die Leute sich gegenseitig unterstützen, wenn es irgendwo nicht weitergeht. Für diese Hilfe danke ich allen aus unserer Gruppe: Friedhelm, Timo, Thomas, Andre, Philipp und Selim. Ihr alle habt dazu beigetragen, sei es durch Nachtschichten im Labor, durch wichtige Diskussionen oder durch Korrekturen, dass die Arbeit erfolgreich wird und dass ich mich in der Gruppe wohl fühle. Neben und bei der Arbeit hatten wir oft viel Spass zusammen. Hier möchte ich nur kurz an verschiedene hochkomplexe Tests zur Bestimmung der Wärmekapazität von Trockeneis oder zur inelastischen Drehstuhl-Drehstuhl Streuung erinnern. Auch für die vielen geselligen Momente möchte ich danken. Nicht zu vergessen natürlich das tägliche Kicker-Spiel, dass jede Woche für neue spielerische und technische Glanzleistungen sorgt.
Neben der Gruppe von Herrn Prof. Ulrich, die für uns eine freundliche und unterstützende Umgebung geschaffen hat, möchte ich mich bei den Mitarbeitern aus der Feinmechanik-Werkstadt bedanken, besonders bei Herrn Seubert und Herrn Flicker. Ohne ihren unermüdlichen Einsatz für die Bearbeitung unserer mechanischen Komponenten, würde unser Experiment nicht so stabil funktionieren, wie es im Moment der Fall ist.
Bedanken möchte ich mich auch bei allen Freunden, die mich durchs Studium begleitet haben, und es eine sehr spannende Zeit werden ließen. Ganz lieben Dank auch an meine Freundin Lisa für alles.
Zuletzt möchte ich meiner Familie, meinen Geschwistern und allen voran meinen Eltern herzlich danken. Ohne euch wäre all dies nicht möglich gewesen.

Erklärung:

Ich versichere, dass ich diese Arbeit selbstständig verfasst und keine anderen als die angegebenen Quellen und Hilfsmittel benutzt habe.

Heidelberg, den _____ _____

Unterschrift